Scale-adaptive Parameterization of Shallow Cumulus Convection

I n a u g u r a l - D i s s e r t a t i o n

zur

Erlangung des Doktorgrades

der Mathematisch-Naturwissenschaftlichen Fakultät

der Universität zu Köln

vorgelegt von

Maren Brast

aus Ulm

Köln, 2017

Berichterstatter:
Prof. Dr. Roel Neggers
Prof. Dr. Susanne Crewell

Tag der mündlichen Prüfung: 30.06.2017

Contents

Abstract

The representation of cumulus clouds in general circulation models is achieved through parameterization schemes. The kind of processes that should be parameterized depends on the discretization of the model. For climate models, the discretization is such that all cumulus clouds are currently fully parameterized. For numerical weather prediction models, the resolutions are getting smaller and reaching the point at which boundary layer clouds can become partially resolved. This creates a problem, since the parameterization should only represent those clouds that cannot be resolved by the model, i. e., the parameterization must become scale-aware and scale-adaptive and thus adjust its activity to the grid spacing. This thesis is dedicated to explore new approaches to achieve this scale-adaptivity.

In the first part of this study, the behavior of the standard rising plume model is investigated, which is capable of interacting with fine-scale structures inside a shallow cumulus cloud layer. To this purpose, a rising plume model is fed with data from a large-eddy simulation (LES) of a shallow convective cloud field, which is one way of providing a plume model with a range of different environments in which it can rise. This framework allows investigating the question of what exactly determines the fate of a rising parcel in a heterogeneous environment; is it the mixing process or the local environment? An ensemble of rising parcels is calculated and each is given its own environment. Bulk statistics are examined of the total ensemble, but also of subsets of parcels with similar termination height. In addition, individual parcels can be traced, yielding insight at process level. The rising plume model includes a formulation for entrainment, which must be specified by the model. Various methods of this entrainment formulation exist in the literature, based on a variety of variables. Some of those formulations are chosen and calibrated to enable a comparison. The various entrainment formulations and their impact on the fate of the plume are then investigated. It is found that the entrainment formulation is of secondary importance. The local environment is more important in determining the behavior of the parcel. Already a constant entrainment formulation can explain much of the variation in termination heights of the parcels, while the entrainment formulation acts on top of this mechanism.

Building on these results, the next step is to explore the scale-adaptivity of a multi-plume parameterization scheme for vertical transport in the shallow convective boundary layer. The scheme used is an Eddy Diffusivity Mass Flux scheme, combining the mass flux approach of rising plumes with the eddy diffusivity of turbulence. The scheme uses multiple plumes and is therefore called ED(MF)^n. A key novelty is that ED(MF)^n is formulated in terms of discretized size distributions, with each plume representing one size-bin. Scale-adaptivity is introduced for the eddy diffusivity part of the scheme with a pragmatic blending approach, while in the mass flux part the size-distribution is filtered, such that only those plumes smaller than the grid size are maintained. This scheme is implemented into an LES model, replacing the original subgrid scheme. This method of using LES as a simple

circulation model, acting as a testing ground for a new parameterization scheme, brings some clear benefits. For example, the scale-adaptivity of ED(MF)^n can be tested by means of sensitivity tests for the horizontal resolution. This should reveal where exactly, i. e., at what range of resolutions, the gray zone for vertical transport in the boundary layer is situated. For this test, an idealized case study of shallow cumulus clouds over the Atlantic is used. It is found that for high resolutions, where most of the shallow cumulus clouds are resolved, the parameterization scheme does not add much transport. For coarser resolutions, it slowly takes over the transport by the clouds, until for the coarsest resolution all clouds are subgrid and represented by ED(MF)^n. The changing partitioning between resolved and subgrid scale transport is in line with the results of previous diagnostic studies based on fully resolved LES fields.

In the last study the parameterization scheme is tested for a more complex situation, which includes a diurnal cycle of cumulus clouds over land. This situation is much more difficult for the parameterization scheme than the marine quasi-equilibrium situation, because of the strong forcing at the surface and the time evolution of the boundary layer during the course of the day. For this test, the previously described setup was run for the measurement campaign HOPE (High Definition Clouds and Precipitation for advancing Climate Prediction Observational Prototype Experiment). The LES was nudged with data from the weather prediction model COSMO-DE, resulting in a semi-realistic representation of the measured conditions. This means that the LES is run such that the forcings and boundary conditions reflect the local weather to a reasonable degree. The LES is then run with and without ED(MF)^n for various resolutions and evaluated with measurements, for three days with differing weather situations. Though this setup proved more challenging due to the diurnal cycle, the behavior of ED(MF)^n in the gray zone as documented for the idealized case over the ocean is reproduced, in particular within the turbulent-convective layer between sunrise and sunset. Measurements of clouds and the vertical thermodynamic structure are reproduced to a reasonable degree across the range of resolutions covering the gray zone. This result gives some confidence in the general applicability of the ED(MF)^n approach and its scale-adaptivity.

Zusammenfassung

Kumuluswolken werden in globalen Modellen der Atmosphäre durch Parametrisierungen dargestellt. Die Art der Prozesse, die parametrisiert werden sollten, hängt von der Diskretisierung des Modells ab. Bei globalen Klimamodellen müssen derzeit alle Kumuluswolken vollständig parametrisiert werden. Für numerische Wettervorhersagemodelle werden die Auflösungen so fein, dass sie einen Punkt erreichen, an welchem die Wolken der Grenzschicht teilweise aufgelöst werden können. Dies kann problematisch werden, da nur die Wolken parametrisiert werden sollten, die vom Modell nicht aufgelöst werden. Die Parametrisierung sollte also merken, welche Skalen aufgelöst werden, und seine Aktivität an die Auflösung anpassen. Diese Arbeit beschäftigt sich damit, eine Möglichkeit zu untersuchen, um diese Skalen-Adaptivität zu erreichen.

Im ersten Teil dieser Arbeit wird das Verhalten von aufsteigenden Luftpaketen in einer konvektiven Grenzschicht untersucht. Dafür bekommen die Luftpakete Daten einer Large Eddy Simulation (LES) von einer konvektiven Grenzschicht mit Kumulusbewölkung, was eine Möglichkeit darstellt, die Luftpakete in verschiedenen Umgebungen aufsteigen zu lassen. Diese Methode erlaubt es, zu untersuchen, was genau das Schicksal eines aufsteigenden Luftpakets in einer heterogenen Umgebung bestimmt; ist es der Mischungsprozess oder die direkte Umgebung? Eine Reihe von aufsteigenden Luftpaketen wird untersucht, wobei jedes Paket eine eigene Umgebung bekommt. Die Luftpakete werden in ihrer Gesamtheit statistisch untersucht, aber es werden auch Teile der Gesamtheit ausgewählt, welche jeweils die gleiche Höhe erreichen. Hinzu kommt die Untersuchung einzelner Luftpakete, um die einzelnen Prozesse detaillierter zu betrachten. Die Berechnung der aufsteigenden Luftpakete beinhaltet eine Formulierung für Entrainment, welche spezifiziert werden muss. In der Literatur werden verschiedene Methoden benutzt, um das Entrainment anzugeben, basierend auf verschiedenen Variablen. Aus diesen Formulierungen werden für diese Arbeit einige ausgewählt und kalibriert, um einen Vergleich zu ermöglichen. Die verschiedenen Entrainment Formulierungen und deren Einfluss auf das Schicksal der Luftpakete werden untersucht. Es wird gezeigt, dass die Formulierung des Entrainments von zweitrangiger Bedeutung ist. Die direkte Umgebung hat einen größeren Einfluss auf das Verhaltens der Luftpakete. Bereits ein konstantes Entrainment kann einen Großteil der Variabilität der Höhen, die von den Luftpaketen erreicht werden, erklären.

Darauf aufbauend wird im nächsten Schritt die Skalen-Adaptivität einer Parametrisierung untersucht, welche mehrere Luftpakete in einer konvektiven Grenzschicht berechnet, um den vertikalen Transport zu beschreiben. Die Parametrisierung benutzt ein sogenanntes Eddy Diffusivity Mass Flux scheme, welches die Berechnung des Massenflusses von aufsteigenden Luftpaketen mit der Diffusivität von Turbulenz kombiniert. Die Parametrisierung benutzt mehrere Luftpakete und heißt deshalb ED(MF)^n. Eine entscheidende Neuerung dieser Parametrisierung ist, dass die Formulierung von ED(MF)^n diskretisierte Größenverteilungen enthält, wobei jedes simulierte Luftpaket eine Größenkategorie repräsentiert. Skalen-Adaptivität ist für den eddy diffusivity Teil der Parametrisierung durch

einen pragmatischen Mischungsansatz eingeführt, während im mass flux Teil die Größenverteilung gefiltert wird, sodass nur die Luftpakete beibehalten werden, die kleiner sind als die Gitterweite. Diese Parametrisierung wird in ein LES Modell implementiert und ersetzt die ursprüngliche Parametrisierung der Turbulenz. Dadurch, dass LES als idealisiertes atmosphärisches Modell genutzt wird, kann die Skalen-Adaptivität von ED(MF)^n getestet werden, indem Sensitivitätsstudien für die horizontale Gitterauflösung durchgeführt werden. Dies hat zum Ziel, herauszufinden, wo genau, also bei welcher Auflösung, der Übergang zwischen aufgelöstem und parametrisiertem vertikalen Transport in der Grenzschicht liegt ("Grauzone"). Für diesen Test wird ein idealisierter Fall von flacher Kumulusbewölkung über dem Atlantik genutzt. Es wird gezeigt, dass für hohe Auflösungen, bei denen ein Großteil der Kumuluswolken aufgelöst wird, die Parametrisierung nicht viel zum Transport beiträgt. Für gröbere Auflösungen übernimmt die Parametrisierung allmählich die Repräsentation des von den Wolken verursachten Transports, bis bei den gröbsten Auflösungen alle Wolken kleiner sind als die Gitterweite und vollständig von ED(MF)^n repräsentiert werden. Dieser Übergang zwischen aufgelöstem und subgridskaligem Transport liegt im Bereich der Ergebnisse früherer Untersuchungen.

Im letzten Teil dieser Arbeit wird ED(MF)^n für eine komplexere Situation getestet, welche einen Tagesgang von Kumulusbewölkung über Land beschreibt. Diese Situation ist schwieriger für die Parametrisierung als die bisher betrachtete Situation, da die Simulation stärker von der Oberfläche beeinflusst wird und sich dadurch die Grenzschicht im Verlaufe des Tages entwickelt. Für diesen Test wird die Messkampagne HOPE (High Definition Clouds and Precipitation for advancing Climate Prediction Observational Prototype Experiment) genutzt. Das LES wird mit Daten des Wettervorhersagemodells COSMO-DE angetrieben, wodurch die gemessenen Bedingungen recht gut wiedergegeben werden können. LES Simulationen mit und ohne ED(MF)^n für verschiedene Auflösungen werden dann mit Messungen verglichen, für drei Tage mit verschiedenen Wettersituationen. Obwohl diese Konfiguration durch die zeitliche Entwicklung der Grenzschicht anspruchsvoller ist, ist das Verhalten von ED(MF)^n in der Grauzone sehr ähnlich zum maritimen Fall, besonders in der turbulent-konvektiven Schicht zwischen Sonnenauf- und -untergang. Die Eigenschaften der beobachteten Wolken und der vertikalen thermodynamischen Struktur werden recht gut für alle Auflösungen über die Grauzone hinweg reproduziert. Dieses Ergebnis erhöht das Vertrauen in die generelle Anwendbarkeit von ED(MF)^n und seiner Skalen-Adaptivität.

1 Introduction

Clouds cover about 2/3 of the Earth's surface (see Fig. 1.1) and have a large impact on the Earth's climate. They affect radiation, and those associated with vertical or horizontal movement also transport energy and moisture, thereby interacting with many other processes in the atmosphere. An increase of clouds can increase the reflection of solar radiation and cool the atmosphere, while the thermal radiation can be hindered to leave the atmosphere, which has a warming effect. Due to these large effects that clouds can have on the climate, they are important to study and understand.

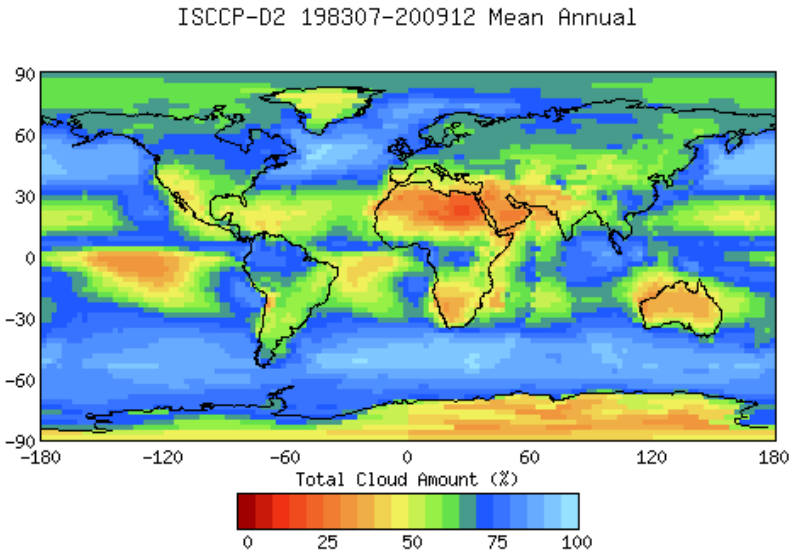

Figure 1.1: Annual mean of total cloud amount in %, adapted from International Satellite Cloud Climatology Project D2 Dataset https://isccp.giss.nasa.gov/products/browsed2.html, accessed on May 3, 2017.

Clouds cover a large range of scales (see Fig. 1.2). Large clouds systems like hurricanes or frontal systems are easily visible from space, covering hundreds of kilometers and lasting several days or longer. Smaller scales include thunderstorms and mesoscale convective systems, where clouds cluster together, forming structures of a size of tens of kilometers. Even smaller scales are single convective clouds in the planetary boundary layer, covering hundreds of meters to a few kilometers. All these clouds consist of many cloud droplets, which have a size in the range of micrometers. These droplets can grow and interact with each other, which is described by cloud microphysics.

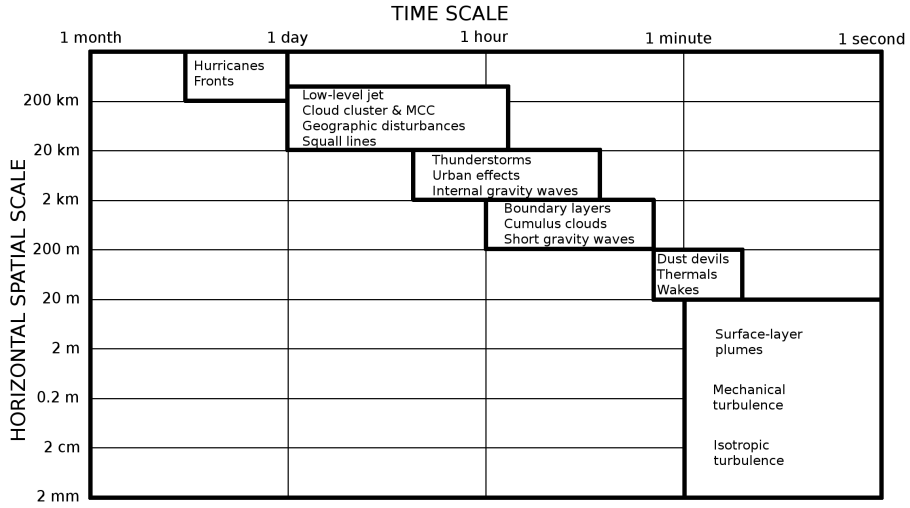

Figure 1.2: Typical temporal and spatial scales of atmospheric processes, adapted from STULL [2009].

1.1 Shallow Cumulus Clouds

One type of clouds are shallow cumulus clouds, which are particularly important to represent in models, because these clouds cover large areas of the globe (see Fig. 1.3). They usually occur persistently in the tropics and subtropics, where at the north-eastern parts of the trade wind regions the stratocumulus clouds transition into cumulus clouds. A satellite image of the northeastern tropical Pacific, west of the American coast, is shown in Figure 1.4. In the visible image, a large area covered with cumulus clouds is seen. A comparison with the infrared image reveals that the large clouds near the bottom of the image are white and therefore deep convective clouds with cold cloud tops. The large area north of those deep clouds is mostly gray in the infrared, which means that these clouds have low cloud tops. Most of these clouds are therefore shallow cumulus clouds. An example of a single shallow cumulus cloud is given in Figure 1.5.

Shallow cumulus clouds are an important part of the Hadley cell [e. g., DORRESTIJN ET AL., 2013; TIEDTKE AND SLINGO, 1988], which describes the circulation in the subtropics and is depicted in Figure 1.6. The principle idea of the Hadley cell is that due to solar insulation, the air rises at the equator, moves to the subtropics, and sinks there, causing the regions in these parts of the globe to be arid. Near the surface, the air moves toward the equator. The winds near the surface in the subtropics, which move to the equator with a relatively constant direction and speed, are called the trade winds. In this circulation, the air moving toward the equator gains humidity by the evaporation of water from the oceans. In the subtropics, a strong temperature inversion is maintained due to the large-scale subsidence, which favors the formation of low level stratiform clouds. Further downstream, the cloud deck transitions from stratocumulus to shallow cumulus clouds, accompanied

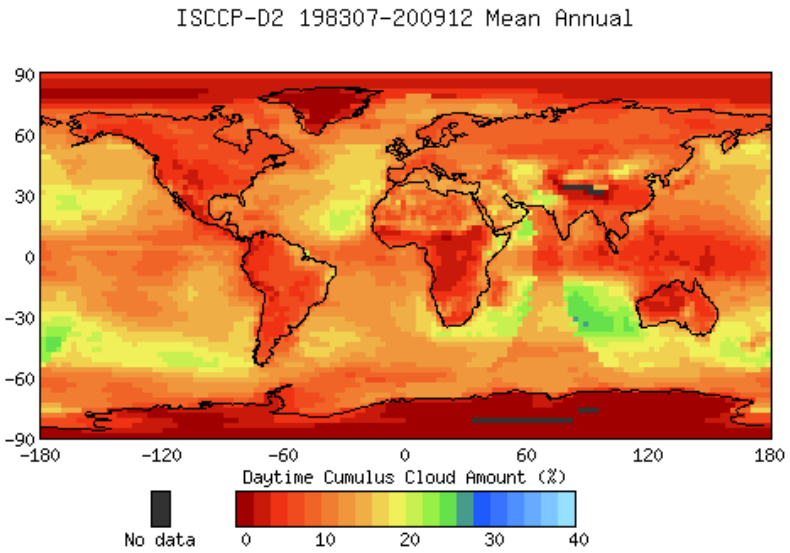

Figure 1.3: Annual mean of daytime cumulus cloud amount in %, adapted from International Satellite Cloud Climatology Project D2 Dataset https://isccp.giss.nasa.gov/products/browsed2.html, accessed on May 2, 2017.

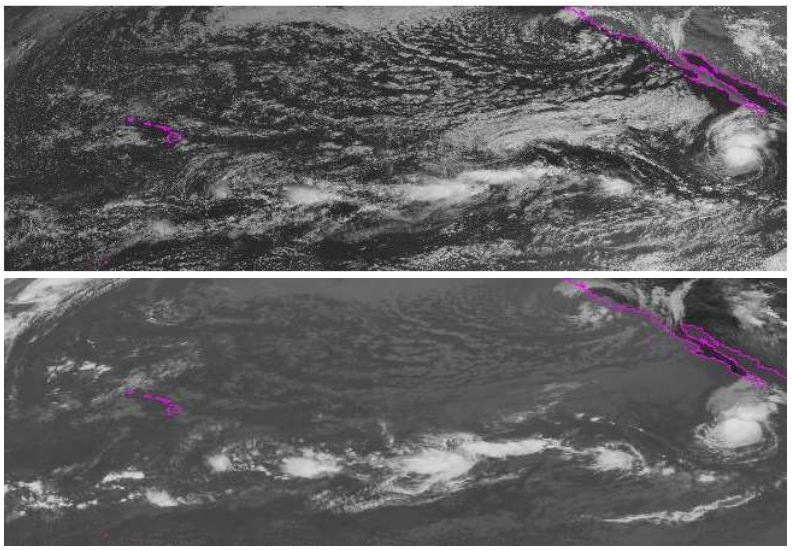

Figure 1.4: Visible (top) and infrared (bottom) satellite image of the tropical northeast Pacific from the Geostationary Operational Environmental Satellite at 18:30 UTC on 20 September 2007, taken from http://inventory.ssec.wisc.edu/inventory/, accessed on March 20, 2017.

Figure 1.5: Example of a single shallow cumulus cloud.

by a dramatic reduction in cloud cover and cloud condensate. These shallow cumulus then pave the way for the deep convection that occurs downstream at the equator at the innertropical convergence zone.

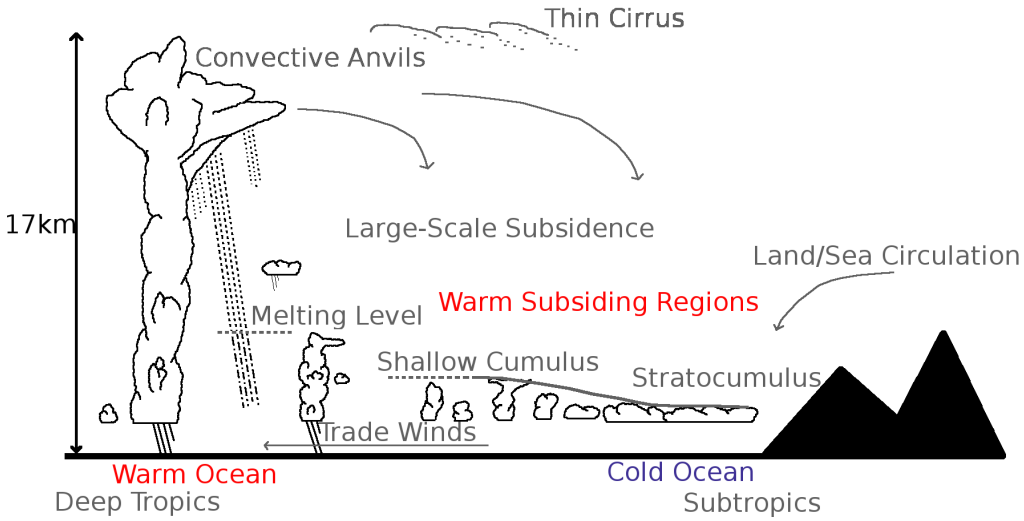

Figure 1.6: Schematic of the Hadley cell, adapted from the Intergovernmental Panel on Climate Change fifth assessment report, chapter 7, Figure 7.4 [BOUCHER ET AL., 2013].

Before the vertical structure of the convective boundary layer is described, the concept of atmospheric instability is presented. To characterize the state of the atmosphere, the temperature change with height is examined, which is called lapse rate. The dry adiabatic lapse rate is the rate of temperature change of a dry parcel, where no phase change of the water occurs and where no energy between parcel and environment is exchanged ("adiabatic"). When the parcel becomes saturated, heat is released when condensation

occurs. Condensation is the phase change from water vapor to condensate, either in liquid or solid form. This process can take place when the humidity content of the air exceeds a certain threshold value, usually referred to as the saturation point. This point depends on the thermodynamic state of the air, as described by for example temperature and pressure, as well as the presence of condensation nuclei. Condensation changes the lapse rate to a moist adiabatic lapse rate. When the lapse rate in a layer of unsaturated air is larger than the adiabatic lapse rate, this layer is called stable. When it is smaller than both dry and moist adiabatic lapse rate, the layer is absolutely unstable. Conditional instability occurs when the lapse rate of a layer is larger than the dry adiabatic lapse rate but smaller than the moist adiabatic lapse rate. Then, when the parcel is forcibly displaced vertically to such a height where condensation occurs, the parcel will continue to rise because of the latent heat release of condensation. This level is called the level of free convection. The height where the parcel has the same density as the surrounding air is the equilibrium level or level of neutral buoyancy. After reaching this level, the parcel might not stop immediately because of its momentum. The level where the parcel stops is called termination height.

Clouds form due to the atmospheric flow, and require the presence of moisture for their formation. Condensation occurs due to cooling, mixing, or adding moisture to the air. Once formed, clouds also interact with the dynamic flow by thermodynamic processes and radiation. Shallow cumulus clouds form as a result of vertical movement of air. The near-adiabatic nature of vertical displacements of air causes the air to cool, by which the saturation vapor pressure decreases. Continued lifting of an air parcel may then drive the saturation point below its total humidity content, so that not all water can be maintained in vapor form, and the first cloud droplets start to form. This point represents the onset of cumulus clouds, and takes place near cloud base. Convection sets in when the surface is heated or the air above the surface is cooled, resulting in instability. This instability is mostly formed at the surface because the solar radiation gets absorbed by the surface, heats it, and leads to conduction of heat from the surface into the atmosphere. Parcels of air near the surface get positively buoyant, which means they feature a smaller density than the surrounding air, and thus the parcels start to rise. As long as they remain buoyant, they continue to rise. Once they reach the lifting condensation level, condensation occurs and a cloud forms. When the air parcel gets less buoyant than the surrounding air, usually when it reaches the inversion height, its momentum causes it to penetrate a small way further (called overshooting), but then it stops and the cloud top is reached.

Since shallow cumulus clouds form in the convective boundary layer, typical profiles for day and night are shown in Figure 1.7. Shown are the temperature, the potential temperature, the water vapor mixing ratio, and wind speed. Several different layers can be identified. The most prominent is the mixed layer, where the potential temperature is constant. In this layer, turbulent mixing results in a fairly homogeneous distribution of

temperature and humidity. At the surface the air is unstable, resulting in a positive heat flux from the surface into the atmosphere. The humidity increases close to the surface due to evaporation, leading to a moistening of the mixed layer. On top of the mixed layer lies a capping temperature inversion, which is a stable layer and therefore slows the turbulent exchange of air between mixed layer and free atmosphere above. During the day, entrainment occurs at the inversion, which is the turbulent mixing of air between free atmosphere and mixed layer. This layer enables the convective boundary layer to grow during the day by mixing in air from above. The humidity decreases sharply in this layer because of the limited mixing between mixed layer and free atmosphere. The horizontal wind is geostrophic in the free atmosphere and decreases in the layers below due to the friction of the surface. Within the mixed layer the wind speed is constant, and decreases sharply in the surface layer. At night, the surface cools due to thermal radiation from the surface into the atmosphere. The mixed layer decays and becomes a residual layer, which is still well mixed but no new turbulence is generated. Near the surface, a stable boundary layer developes. Here, also the humidity decreases because condensation in the form of dew or frost occurs due to the cooling of the air. If no condensation occurs, the humidity does not decrease near the surface. In the mixed layer, the turbulence is gone, causing the friction to disappear too. Therefore, the horizontal winds increase in the mixed layer toward the geostrophic value, and even surpasses the geostrophic value due to the Coriolis force. This maximum is called a nocturnal lowlevel jet.

The presence of clouds changes the layering of the atmosphere, since a cloud layer is added. Near the surface, there is still a small layer of instability, enabling air to rise, with the mixed layer above. In the cloud layer on top of the mixed layer, the air is conditionally stable, followed by the inversion at the top of the cloud layer, causing the shallow cumulus clouds to stay in the convective boundary layer. Due to the inversion, the moisture in the boundary layer that was evaporated at the surface does not easily rise into the free atmosphere. During the day, the overshooting of the rising clouds into the inversion layer leads to mixing of the air above into the convective boundary layer, which is why the boundary layer deepens with time.

Compared to other cloud types, the shape of shallow cumulus clouds is fairly compact, since the depth and the horizontal size are of the same order of magnitude. However, there are large variations in the form of their shape. When an inversion is present, they tend to be wider than they are high, but if there is no inversion they can become much higher than they are wide. In a shallow cumulus cloud field, the relative horizontally mean humidity is less than 100 % with a vertically projected cloud fraction of the order of 5 - 30 % [ZHANG AND KLEIN, 2013]. Shallow cumulus clouds reach a height of about 1 - 2 km. In a shallow cumulus cloud field, there exist many small clouds and only few large clouds. This size distribution has been described with lognormal distributions [LÓPEZ, 1977] and

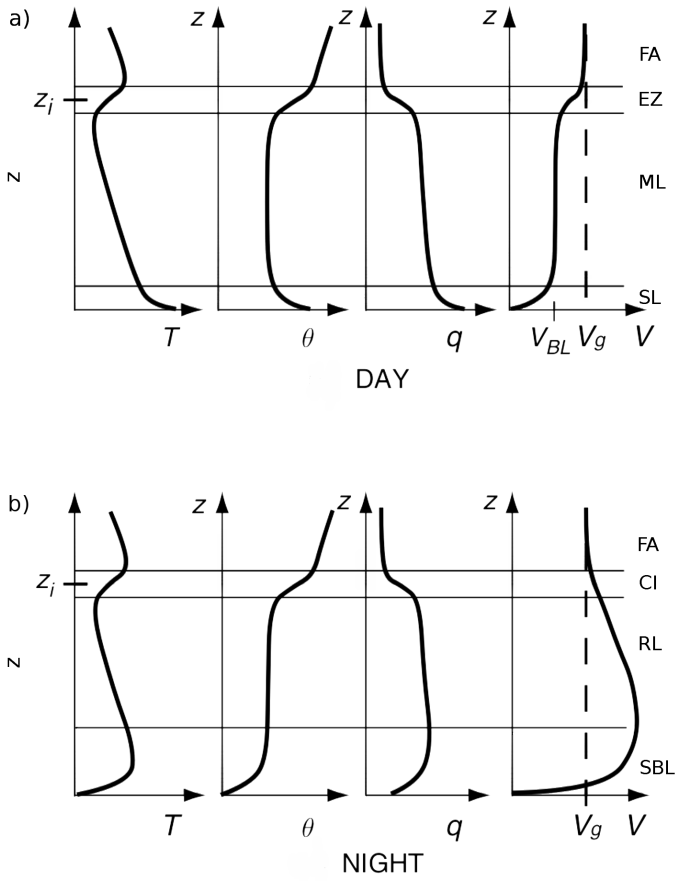

Figure 1.7: Typical vertical profiles of a convective boundary layer for day and night time, with temperature T, potential temperature Θ, water vapor mixing ratio q, and horizontal wind speed V, with V_g the geostrophic wind and V_{BL} the wind in the boundary layer. The different layers of the boundary layer are abbreviated as follows: FA: free atmosphere, EZ: entrainment zone, ML: mixed layer, SL: surface layer, CI: capping inversion, RL: residual layer, and SBL: stable boundary layer. z_i is the height of the boundary layer. Adapted from STULL [2000].

exponential distributions [PLANK, 1969; WIELICKI AND WELCH, 1986], but more recently has been found to be better described by a power law [BENNER AND CURRY, 1998; NEGGERS ET AL., 2003]. On average, the vertical velocity inside the cloud is positive, while it is slightly negative at the edges of the cloud. In the environment of the clouds, a general sinking motion prevails, to compensate for the positive vertical velocities in the clouds (see Fig. 1.8). The inside of shallow cumulus clouds is not homogeneous but rather turbulent, resulting in a high variability of vertical velocity, temperature, and moisture inside the cloud. This is indicated in the bars in Figure 1.8, which represent turbulence.

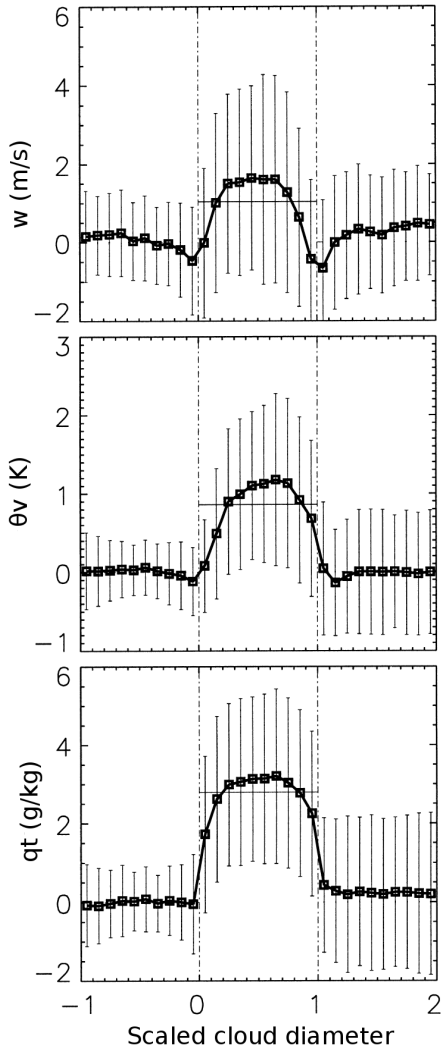

Figure 1.8: Horizontal cross section of deviation from the mean of vertical velocity, virtual potential temperature, and total water content of an average shallow cumulus cloud. The bars denote the root mean square of the deviation from the mean. Adapted from RODTS ET AL. [2003].

Cumulus clouds interact with their environment by mixing. Small turbulent eddies at the edges of the clouds mix cloudy air out of the cloud and environmental air into the cloud.

This process is called entrainment. For many years there has been a controversy on where the entrainment mainly takes place. One theory was that the mixing takes place at the lateral cloud edges [STOMMEL, 1947], while the other theory assumes that environmental air is mixed into the cloud mainly at or near cloud top and is then transported downward into the cloud [SQUIRES, 1958]. Recent large-eddy simulation (LES) studies seem to provide an answer to this controversy, by tracing particles inside the clouds back in time [HEUS ET AL., 2008]. They found that air is mainly entrained at the lateral edges of the cloud. The representation of entrainment in models is a focus of chapter 3.

Other types of cumulus clouds are stratocumulus, congestus, and deep cumulus. Stratocumulus clouds are boundary layer clouds, featuring a high cloud cover where the single cumulus clouds are not separated but strung together, forming a cloud layer of fairly small vertical extent. Deep cumulus convection is formed of cumulus clouds which reach several thousands of meters into the free atmosphere and usually produces precipitation.

1.2 Modeling Clouds

Because of their large impact on weather and climate, clouds have to be represented in weather and climate models. Unfortunately, in simulations predicting the future climate, they are a major uncertainty [e. g., ARAKAWA, 1975; BONY ET AL., 2006; VIAL ET AL., 2013], because the resolutions of present day general circulation models is still too low to resolve the full size spectrum of cloudy processes, leaving some of these unresolved. As a result, their impact on the larger-scale flow has to be represented through parameterization (see section 2.2). For this, we need to understand the complex behavior of clouds, which is difficult to achieve. Figure 1.9 shows the uncertainty connected with the feedbacks of clouds, surface albedo, water vapor and lapse rate, and Planck response, in global climate models. For the three latter feedbacks, the temperature change is similar across models, while for the clouds, there is a large variation between the models. Overestimating or underestimating cloud cover can lead to errors in radiation feedbacks and precipitation, so a good representation of clouds in models is pursued. Clouds cover a large range of scales, from global scales to mesoscales and high and low pressure systems, to fronts and individual clouds and down to microphysics. Individual clouds can also vary greatly in size. How well clouds can be resolved depends on the model and its grid spacing. In the following, a selection of models is described.

In global climate simulations, most clouds are parameterized because the grid spacing of the models of the order of 100 km is very coarse. The aim of these types of models is to estimate a trend of future climate and to get insight into the climate system. Because of the large time scales considered, these models cannot give a forecast but rather

an estimation of the future climate, for which many different assumptions are made. In contrast, global weather prediction models cover a smaller time scale and are able to calculate fairly accurate predictions of the weather for several days. With their resolutions of tens of kilometers, pressure systems and fronts can be resolved, while individual cumulus clouds cannot. For a more detailed forecast, regional models can be nested into the larger scale models. These models only cover a restricted horizontal area, for example the area of a continent or a country. The inflow into these domains is given by the larger scale model. With these models, much finer resolutions of a few kilometers can be achieved and therefore the forecast can be more detailed. In these models, fewer parameterizations are needed because more processes can be resolved.

Other models do not primarily have the aim to provide a forecast, but serve to, e. g., get insight into the climate system or to perform scientific research on clouds. The understanding gained with these models can then serve to improve weather and climate forecast models. One type of such models are single column models, representing only one column of a climate model. The physics of these models is usually the same as those of the corresponding climate model, but the dynamics need to be provided. These models have the advantage of a very small demand of computing power, thus giving fast results. With single column models, new parameterization schemes can easily be tested without the complexity of feedback processes in a more complex model. Disadvantages are that the results heavily depend on the prescribed forcings and three dimensional effects are not represented.

Another type of models used in research are cloud resolving models (CRM). These models are three dimensional models designed to study deep convective clouds. Due to their fine resolutions of the order of one kilometer, these models are much more computationally expensive than single column models. A similar type of models are large-eddy simulation (LES) models. They have finer resolutions than CRMs (of the order of 50 m) and are more idealistic, e. g., they have simpler microphysics schemes and different turbulence parameterizations. LES models resolve most of the turbulence and are mostly used to study small scale processes in the boundary layer, such as shallow cumulus clouds. Since an LES model is used in this study, this type of model is described in more detail in section 2.3.

1.3 Outline

Chapter 2 of this thesis presents the general methods used throughout the thesis. It describes the concepts of parameterization in models and large-eddy simulation models, and the cases studied in this thesis. Chapter 3 - 5 examine different aspects of the simulation

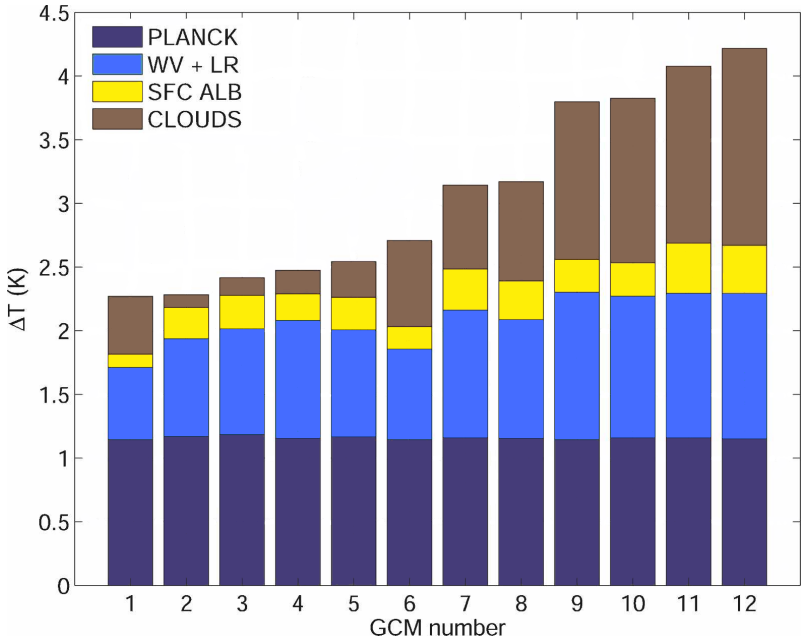

Figure 1.9: Temperature change by various feedbacks for 12 global climate models (see text), adapted from DUFRESNE AND BONY [2008].

of shallow cumulus clouds. The first of these chapters (chapter 3) is a general study of a rising parcel model, and studies the relative importance of the entrainment formulation on the parcel in a model where shallow cumulus clouds are resolved. In chapter 4, the focus turns to the representation of shallow cumulus clouds in models with different resolutions. With increasing computing powers, the resolution of large scale models improves such that large clouds can be resolved, i. e., the large scales of turbulence. Small clouds and the rest of the turbulence cannot be resolved, but must be somehow taken into account. The scale where some clouds can be resolved and others cannot is called the gray zone of convection [WYNGAARD, 2004]. A parameterization scheme is tested which takes into account those clouds that are smaller than the grid size. The test case of this study is very idealized to better understand the underlying mechanisms. Chapter 5 then takes the step toward more complex cases, to test how well such a scheme can represent transient cases over land. For this study, the model is compared to observations. At the end of this thesis, chapter 6 gives a summary of all findings, a conclusion and an outlook.

2 Technical Background

2.1 Overview over Important Variables

In this section, several variables are introduced which are used throughout this thesis to describe the shallow cumulus cloud layer. Knowledge of basic variables like velocity components (u, v, w) or temperature (T) is assumed.

Two variables used are variations of the potential temperature Θ, which is the temperature of an unsaturated parcel of air that it has when adiabatically brought to the reference pressure level of 1000 hPa:

$$\Theta = T \left(\frac{p_{1000}}{p} \right)^{\frac{R_g}{c_p}} \tag{2.1}$$

with T the temperature, p the pressure, p_{1000} the reference pressure of 1000 hPa, R_g the gas constant, and c_p specific heat capacity for an ideal gas at constant pressure. The virtual potential temperature is that potential temperature of a parcel of dry air with the same density and the same pressure as a moist parcel would have:

$$\Theta_v = \Theta(1 + 0.61q - q_l) \tag{2.2}$$

with q the water vapor mixing ratio and q_l the liquid water mixing ratio. The water vapor mixing ratio is the ratio of the mass of water vapor to the mass of dry air in a unit volume of air. Similarly, the liquid water mixing ratio and the total water mixing ratio q_t are defined. Another temperature used is the liquid water potential temperature, which can be approximated by [BETTS, 1973]:

$$\Theta_l \approx \Theta - \frac{q_l L_v \Theta}{c_{pd} T} \tag{2.3}$$

which has the advantage of being conserved in a shallow convective boundary layer without precipitation. Here, L_v is the latent heat of vaporization and c_{pd} the specific heat of dry air at constant pressure.

In parameterizations of shallow cumulus clouds, it is often assumed that there are non-local updrafts, covering a small fraction of the area and featuring a strong positive vertical velocity, while the rest of the area is mostly governed by local turbulence. Cloudy updrafts are updrafts which reach the cloud layer, so that condensation occurs and a cloud forms on top of the updraft. A cloud core is usually defined as an area with a positive vertical velocity and positive buoyancy. Sometimes, an additional requirement is the presence of liquid water.

2.2 Parameterization

Atmospheric models use prognostic equations to describe the future state of the atmosphere. Since the models cannot consider the atmospheric conditions everywhere in the atmosphere, the equations need to be discretized to the model grid. That way, the state of the atmosphere is predicted only for the grid points, which, depending on the model, can have a distance of tens, up to hundreds of kilometers between them. This discretization is accomplished by Reynold's averaging, which splits the variable a into a mean state $\overline{a}$ and the deviation of the mean a': $a = \overline{a} + a'$. By applying this averaging on the prognostic equations of atmospheric models, in addition to the averaged terms from the original equations, additional terms in the form of $\overline{a'b'}$ appear. Since these variations of variables between grid points cannot be known, some closure must be found for those terms describing these subgrid-scale processes. This problem is called parameterization.

The small subgrid-scale processes cannot be neglected in most models, because they can add considerably to the overall energy and moisture transport. Processes, for which parameterizations are needed in modern weather and climate models, are, e. g., the processes in the planetary boundary layer, the land surface, radiation, clouds, and convection. Some of these processes can interact with each other; in that case the appropriate parameterization for the situation at hand is used. The work in this thesis focuses on the parameterization of shallow convection. There exist parameterization schemes only for shallow convection, such only for deep convection, and some schemes that represent all convection (a review of cumulus parameterization is given in ARAKAWA [2004]).

2.2.1 Early Shallow Cumulus Parameterizations

In the early days of shallow cumulus parameterization, the energy spectrum was assumed to have a spectral gap between the synoptic scales and the small scales [e. g., VAN DER HOVEN, 1957]. This energy spectrum is shown in Figure 2.1, where the right side, from the energy production near the peak to the dissipation of energy, represents the turbulence,

while the left side represents the mean flow. With this spectral gap, the scales can be separated into the small scales that must be parameterized, and the resolved large scale flow. The parameterized small scales have such small time scales that their effect can be represented in one time step. In the beginning, two different approaches were taken. One approach assumed that the vertical thermodynamic profiles are adjusted through cumulus parameterization [MANABE ET AL., 1965]. The other approach assumed that cumulus parameterization can be described by large scale motion because it is controlled by it. The latter approach describes updrafts and downdrafts with entrainment and detrainment and models the mass flux. A lot of research has been done in this category [e. g., OOYAMA, 1971; YANAI ET AL., 1973; BETTS, 1973; ARAKAWA AND SCHUBERT, 1974; FRITSCH AND CHAPPELL, 1980; TIEDTKE, 1989; CHEINET, 2003].

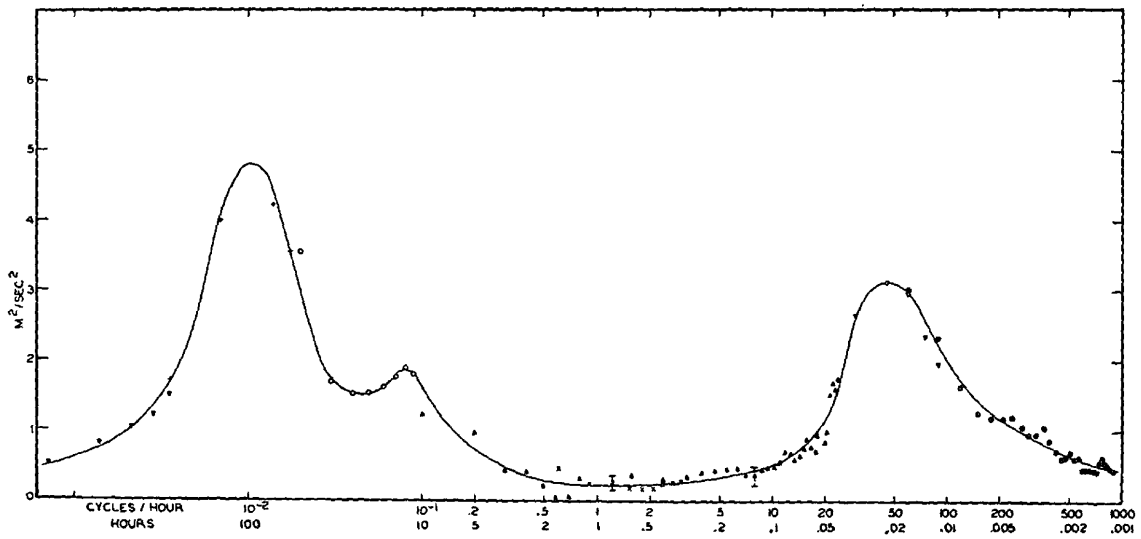

Figure 2.1: Energy spectrum at 100 m height, adapted from VAN DER HOVEN [1957].

The mass flux approach uses the top-hat assumption, where it is assumed that a shallow cumulus field can be divided into an active updraft and the environment. The flux of a variable Φ can then be described by [SIEBESMA AND CUIJPERS, 1995]:

$$\overline{w'\Phi'} = a_u \overline{w'\Phi'}^u + (1-a_u)\overline{w'\Phi'}^e + a_u(1-a_u)(w_u - w_e)(\Phi_u - \Phi_e) \tag{2.4}$$

with a the fraction of the active updraft, u denoting the average over the active updrafts and e the average over the surrounding environment. It is then assumed that the third term on the right side dominates over the other two terms, i. e., that the organized turbulence due to the averaging between updraft area and environment dominates the turbulence within the updrafts and the turbulence within the environment. By also assuming that the area covered by the updraft is much smaller than one, and defining a mass flux

$M = \rho w_u a_u$ we get

$$\overline{w'\Phi'} = \frac{M}{\rho}(\Phi_u - \Phi_e) \tag{2.5}$$

with ρ the density.

Since the early days of convective parameterization, the existence of the spectral gap as depicted in Figure 2.1 has been doubted. For coarse resolutions when all convection is parameterized, the top-hat approach still gives good results, but when resolutions get so fine that parts of the convection becomes resolved, the assumption of a very small updraft fraction in each grid box becomes problematic. Therefore, the parameterization schemes have been further developed.

2.2.2 Recent Developments of Parameterization Schemes

Recently, efforts were made to include stochastics to describe cumulus convection, representing the statistic nature of convection. To name only some, PLANT AND CRAIG [2008] introduced stochastics to a mass flux scheme by drawing the characteristics of the rising plumes from a probability density function. The scale-adaptivity of this scheme was tested by KEANE ET AL. [2014]. A different approach was taken by DORRESTIJN ET AL. [2013], who used conditional Markov chains. SAKRADZIJA ET AL. [2015] and SAKRADZIJA ET AL. [2016] used stochastics with the aim of developing a scale-adaptive scheme.

Many schemes are only appropriate for a specific case, e. g., either deep or shallow convection, either stratocumulus or cumulus. To be consistent and to avoid artificial separation between different processes, efforts are made to develop unified schemes, which encompass a broader scope of processes. LAPPEN AND RANDALL [2001] aim to unify the parameterization of convection and the boundary layer, while HOHENEGGER AND BRETHERTON [2011] and PARK [2014a,b] combine deep and shallow convection, and others look at the scale-adaptivity of deep convection schemes [ARAKAWA AND WU, 2013; GERARD, 2015].

Developments of the mass flux approach include combining it with the eddy diffusivity of the turbulence around the updrafts, called Eddy Diffusivity Mass Flux scheme, "EDMF" [SOARES ET AL., 2004; SIEBESMA ET AL., 2007]. The eddy diffusivity can be modeled by relating the flux of a variable to its vertical gradient:

$$\overline{w'\Phi'} = -K\frac{\partial\overline{\Phi}}{\partial z} \tag{2.6}$$

with a coefficient K. Other schemes use multiple updrafts in a column instead of one updraft [e. g., WAGNER AND GRAF, 2010], or combine EDMF with multiple updrafts [NEG-

GERS ET AL., 2009; NEGGERS, 2009; SUŠELJ ET AL., 2012; NEGGERS, 2015]. The latter is described in more detail in chapter 4.

2.3 Large-Eddy Simulation

Developing cumulus parameterization schemes often makes use of large-eddy simulations (LES), which are idealized high resolution models. An example for a shallow cumulus cloud field simulated by LES is given in Figure 2.2. LES models are used to improve our understanding of the atmosphere [e. g. STULL, 2009]. Through measurements, the atmosphere can be observed, but many different processes occur at the same time, and since a weather situation only occurs once and is not reproducible, sensitivity studies are difficult. LES helps to isolate certain processes by simulating an idealized turbulent field. Here, processes can be reproduced and studied in detail. Also, certain parameters can be changed slightly, so that the sensitivity of the simulation to these parameters can be studied. The aim of an LES is not to exactly reproduce observed turbulence. When studying individual simulated eddies, they quickly develop away from the observed eddies. Instead, the aim is to reproduce the statistical characteristics of the turbulent field. LES is initialized with characteristic conditions of the desired simulated regime. Then, at the beginning, small random disturbances are imposed to develop turbulence. After the turbulence is developed, the turbulent processes can be studied. Since LES resolves the large eddies that carry most of the energy but parameterizes small eddies, LES is mainly used to study turbulent processes in the boundary layer.

To develop shallow cumulus parameterization schemes, LES can be used to give insight into processes, which can help to formulate a parameterization and to determine parameters (e. g., entrainment and detrainment rates) [e. g., SIEBESMA AND CUIJPERS, 1995; GREGORY, 2001; SIEBESMA ET AL., 2007; DE ROOY AND SIEBESMA, 2008; NEGGERS ET AL., 2009; HOHENEGGER AND BRETHERTON, 2011]. To inform the development of cumulus parameterization schemes, the LES is run with a variety of cases. These cases are often idealized cases based on measurement campaigns, for example BOMEX, RICO, ATEX, and ARM. BOMEX (Barbados Oceanographic and Meteorological Experiment, HOLLAND AND RASMUSSON [1973]; SIEBESMA ET AL. [2003]) and RICO (Rain in shallow Cumulus over the Ocean, RAUBER ET AL. [2007]; VANZANTEN ET AL. [2011]) describe trade wind cumuli in the Caribbean, while ATEX (Atlantic Trade Wind Experiment, AUGSTEIN ET AL. [1973]; STEVENS ET AL. [2001]) describes cumulus clouds over the Atlantic. An example for shallow cumulus clouds over land with a diurnal cycle is the ARM case (Atmospheric Radiation Measurement Program, ACKERMAN AND STOKES [2003]; BROWN ET AL. [2002]). Sometimes a convective boundary layer is simulated by LES without the basis of a measurement campaign. These cases can be set up individually, but then it is not possible to compare

the simulation to measurements. The parameterization schemes, which are implemented into, e. g., a single column model, are then compared to observations or the output of such LES simulations to evaluate the performance of the parameterization scheme.

A novelty of one of the studies presented here is the different use of LES. Instead of comparing the parameterization to LES, it is implemented into it, replacing the original subgrid scheme, thus giving the opportunity to test the parameterization in an idealized environment, facilitating transparency and thus a deeper understanding of the behavior of the scheme, and enabling tests with very fine resolutions to test scale-adaptivity (see chapter 4).

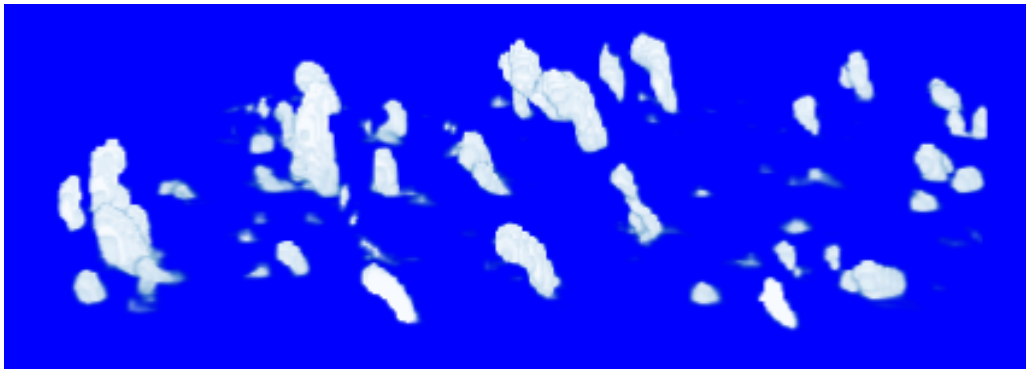

Figure 2.2: Example of a shallow cumulus cloud field simulated by LES.

Since idealized small-scale simulations must describe turbulence, a short overview over turbulence in the atmosphere is given. Turbulence in the atmosphere occurs mainly in the boundary layer. It is generated by vertical wind shear caused by the friction at the surface, by obstacles such as trees, and by the heating of the surface and the ensuing rising of air. Also, turbulence occurs outside of the boundary layer in cumulus clouds or near strong wind shear. Turbulence serves as an effective way of transporting heat away from the surface and into the atmosphere, contributing to a well-mixed layer above the surface. Turbulence can be thought of as eddies of different sizes, superimposed on the mean wind. Those eddies can be observed for example in meandering plumes above chimneys or on the water of lakes. The largest eddies are about as large as the boundary layer height. Those eddies decay into smaller eddies, which then decay into even smaller eddies, until the smallest eddies dissipate. With this process, energy is transported to smaller scales, which is called the energy cascade.

The mean flow in the atmosphere is usually modeled by numerical weather and climate models, while the turbulence usually must be parameterized. There are different ways to explicitly simulate turbulence. One approach is direct numerical simulation (DNS), which has very fine resolutions of the order of millimeters and in which all turbulence is resolved. These simulations are very accurate but limited in their domain size because

of high computing costs. On the other hand, Reynolds-averaged Navier-Stokes Simulation (RANS) only simulates the mean flow, parameterizing all turbulence, which has the advantage of very low computing costs. Because it is completely parameterized, turbulence cannot be studied. A compromise is large-eddy simulation (LES), which resolves most of the energy contained in turbulence, while parameterizing only the small eddies. This enables much larger domain sizes than possible for DNS, while turbulence can still be studied since all large eddies are resolved. All eddies that are around twice the grid size are resolved, while the smaller ones are filtered and parameterized by a subgrid-scale scheme. The equations used in LES are Boussinesq-approximated and filtered spatially, which can be done explicitly or implicitly by the grid spacing (see section 2.3.1).

Large-eddy simulations have been shown to be very useful in simulating the atmospheric boundary layer. Various regimes can be simulated, ranging from stable boundary layers [e. g., BEARE ET AL., 2006; SAIKI ET AL., 2000], stratocumulus topped boundary layers [e. g., CHLOND AND WOLKAU, 2000; VAN DER DUSSEN ET AL., 2015] to convective boundary layers [e. g., MASON, 1989; NIEUWSTADT ET AL., 1993; SIEBESMA ET AL., 2003]. Various different situations can be imposed, ranging from dry desert regions to humid climate to arctic climate. LES can thus also be used to study in an idealized way the impact of warming in a given region. The underlying mechanisms of processes can be studied with LES in an idealized environment, where transparency is high because of its simplicity. Processes studied by LES include cold-air outbreaks [e. g., CHLOND, 1992; GRYSCHKA AND RAASCH, 2005], flow around buildings [e. g., LETZEL ET AL., 2012; CALHOUN ET AL., 2005], flow above a canopy layer [e. g., SHAW AND SCHUMANN, 1992; KANANI-SÜHRING AND RAASCH, 2015; NEBENFÜHR AND DAVIDSON, 2015]), dust devils [e. g., KANAK ET AL., 2000; RAASCH AND FRANKE, 2011; ITO ET AL., 2013], and flow above heterogeneous surfaces [e. g., SHEN AND LECLERC, 1995; AVISSAR AND SCHMIDT, 1998; MARONGA AND RAASCH, 2013].

In the future, computing power will continue to increase. On the one hand, this causes direct numerical simulations to be able to simulate larger domains, and on the other hand, large-scale models can increase their resolution to resolve previously subgrid-scale processes. However, LES will still be useful. One application is the simulation of very small processes which need a fine resolution but also a large domain to be correctly represented in the model, e. g., dust devils, which need the convection to be resolved. Another application is the simulation of long time-scales [SCHALKWIJK ET AL., 2015], which gives the advantage of a good statistics, evaluation of the LES to a variety of weather regimes, and evaluation of measurements. Also, LES can be used as a "superparameterization" [GRABOWSKI, 2016], in which a three dimensional LES is implemented into a global weather or climate model. Then, the large-scale motions are resolved by the large-scale model, while small-scale processes such as the boundary layer and convection are resolved by the LES.

However, models should be compared to observations to ensure that the simulated flows are realistic. In chapter 5 of this thesis, the LES simulations are compared to observations.

2.3.1 Formulation of an LES Model

LES models are based on the Navier-Stokes-equation

$$\frac{\partial u_i}{\partial t} + u_k \frac{\partial u_i}{\partial x_k} = -\varepsilon_{ijk} f_j u_k - g\delta_{i3} - \frac{1}{\rho}\frac{\partial p}{\partial x_i} + \nu_m \left[\frac{\partial^2 u_i}{\partial x_k^2} + \frac{1}{3}\frac{\partial}{\partial x_i}\left(\frac{\partial u_k}{\partial x_k}\right)\right], \tag{2.7}$$

the continuity equation

$$\frac{\partial \rho}{\partial t} + \frac{\partial \rho u_k}{\partial x_k} = 0, \tag{2.8}$$

and the first law of thermodynamics for potential temperature

$$\frac{\partial \Theta}{\partial t} + u_k \frac{\partial \Theta}{\partial x_k} = \nu_h \frac{\partial^2 \Theta}{\partial x_k^2} + S_h, \tag{2.9}$$

with u_i (i = 1,2,3) the three velocity components, x_i (i = 1,2,3) the Cartesian coordinates x, y, and z, ε_{ijk} the Levi-Civita symbol, δ_{ij} the Kronecker delta, f the Coriolis parameter, g the gravity acceleration, ν_m and ν_h the molecular diffusion coefficients for momentum and heat, Θ the potential temperature, and S_h a source term for heat. All three-dimensional variables are dependent on the time t and the three coordinates x, y, and z. Einstein summation notation is used.

It is not possible to analytically solve these equations. Therefore, an approximation is used. Often the equations are Boussinesq-approximated, which means that the flow is assumed to be incompressible [e. g. ETLING, 2008]. This approximation is only applicable for shallow convection. An alternative approximation is the anelastic approximation, further described in section 2.4 using the example of the model used in this study, where the density is allowed to change in the vertical. Using the Boussinesq-approximation means for the continuity equation

$$\frac{\partial u_k}{\partial x_k} = 0. \tag{2.10}$$

The thermodynamic variables of pressure, density, and temperature can be split up into a ground state and the deviation of that ground state:

$$p(x,y,z,t) = p_0(z) + p*(x,y,z,t), \tag{2.11}$$

$$\rho(x,y,z,t) = \rho_0(z) + \rho*(x,y,z,t), \tag{2.12}$$

$$T(x,y,z,t) = T_0(z) + T*(x,y,z,t). \tag{2.13}$$

Now it is assumed that the deviations are much smaller than the ground state: e. g. $p* << p_0$.

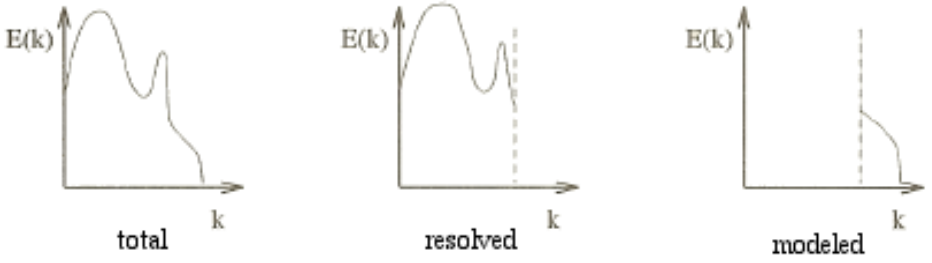

Figure 2.3: Schematic of the decomposition of the energy spectrum into resolved and subgrid scales, adapted from SAGAUT [2006].

This gives the Boussinesq-approximated set of equations. Now, the small scales need to be filtered out. This is accomplished by applying a filter, which separates the resolved scales from the unresolved scales (Figure 2.3). This filter gives the resolved field Φ:

$$\overline{\Phi}(x_i,t) = \int_{-\infty}^{+\infty} dt' \int_{-\infty}^{+\infty} d^3x_i' \Phi(x_i',t') G(x_i - x_i', t - t') \tag{2.14}$$

with the convolution kernel G [SAGAUT, 2006].

The resulting Boussinesq-approximated and filtered equations are:

Navier-Stokes equation

$$\frac{\partial \overline{u_i}}{\partial t} + \frac{\partial \overline{u_k}\overline{u_i}}{\partial x_k} = -\varepsilon_{ijk} f_j \overline{u_k} + \varepsilon_{i3k} f_3 \overline{u}_{k_g} + \frac{\overline{\Theta^*}}{\Theta_0} g \delta_{i3} - \frac{1}{\rho_0} \frac{\partial \overline{p^*}}{\partial x_i} + \nu_m \frac{\partial^2 \overline{u_i}}{\partial x_k^2} - \frac{\partial \tau_{ki}}{\partial x_k}, \tag{2.15}$$

Continuity equation

$$\frac{\partial \overline{u_k}}{\partial x_k} = 0, \tag{2.16}$$

and First Law of Thermodynamics

$$\frac{\partial \overline{\Theta}}{\partial t} + \frac{\partial \overline{u_k}\overline{\Theta}}{\partial x_k} = -\frac{\partial \gamma_k}{\partial x_k} + S. \tag{2.17}$$

with the subgrid fluxes of momentum and heat

$$\tau_{ij} = \overline{u_k' u_i'}, \tag{2.18}$$
$$\gamma_k = \overline{u_k' \Theta'}. \tag{2.19}$$

For this set of equations the subgrid fluxes need to be parameterized. There are several approaches to do this. One is the approach by DEARDORFF [1980], which uses

$$\tau_{ki} = -K_m \left(\frac{\partial \overline{u_i}}{\partial x_k} + \frac{\partial \overline{u_k}}{\partial x_i} \right) + \frac{2}{3}\delta_{ki}\overline{e}, \tag{2.20}$$
$$\gamma = -K_h \frac{\partial \overline{\Theta}}{\partial x_k} \tag{2.21}$$

with K_m and K_h the subgrid-scale eddy diffusivity coefficients for momentum and heat:

$$K_m = 0.1 l \overline{e}^{1/2}, \tag{2.22}$$
$$K_h = \left(1 + \frac{2l}{\Delta s}\right) K_m \tag{2.23}$$

with

$$\Delta s = (\Delta x \Delta y \Delta z)^{1/3}, \tag{2.24}$$

and the subgrid-scale mixing length l_{SGS}

$$l_{SGS} = l_s = 0.76 \overline{e}^{1/2} \left(\frac{g}{\Theta_0} \frac{\partial \overline{\Theta}}{\partial z} \right)^{-1/2} \tag{2.25}$$

for $\partial\Theta/\partial z > 0$ and $l_s < \Delta s$ and otherwise

$$l_{SGS} = \Delta s. \tag{2.26}$$

To determine the coefficients K_m and K_h, the turbulent kinetic energy e is needed:

$$\frac{\partial \bar{e}}{\partial t} = -\frac{\partial \bar{u}_k \bar{e}}{\partial x_k} - \tau \frac{\partial \bar{u}_i}{\partial x_k} + \frac{g}{\Theta_0} \overline{u_3' \Theta'} - \frac{\partial}{\partial x_k} \left[\overline{u_k' \left(e' + \frac{p'}{\rho_0} \right)} \right] - \zeta \tag{2.27}$$

with the dissipation rate

$$\zeta = \left(0.19 + 0.51 \frac{l}{\Delta s} \right) \frac{\bar{e}^{3/2}}{l}. \tag{2.28}$$

Another approach is the Smagorinsky-Lilly model (see also section 2.4 for the documentation of the LES model used here). In this model, the subgrid fluxes are

$$\tau_{ij} = -\rho_0 K_m D_{ij}, \tag{2.29}$$

$$\gamma = -\frac{K_m}{Pr} \frac{\partial \overline{\Phi}}{\partial x_j}, \tag{2.30}$$

with D_{ij} the resolved deformation and Pr the Prandtl number. The resolved deformation is formulated as

$$D_{ij} = \frac{\partial \overline{u}_i}{\partial x_j} + \frac{\partial \overline{u}_j}{\partial x_i}, \tag{2.31}$$

$$K_m = (C_s l)^2 S \sqrt{1 - \frac{Ri}{Pr}}, \tag{2.32}$$

with

$$Ri = \frac{Q^2}{N^2} \tag{2.33}$$

and

$$Q^2 = \frac{\partial \overline{u}_i}{\partial x_j} D_{ij} \tag{2.34}$$

$$N^2 = \frac{g}{\Theta_0} \frac{\partial \overline{\Theta}_v}{\partial z}. \tag{2.35}$$

Here, C_S is the Smagorinsky constant and l is the length scale

$$l^{-2} = (\Delta x \Delta y \Delta z)^{-2/3} + \left(\frac{z\kappa}{C_S}\right)^{-2} \tag{2.36}$$

with κ the von Kármán constant.

2.4 The LES model UCLALES

The LES used here is the UCLALES, which was started by Bjorn Stevens at the University of California, Los Angeles (thus its name), and based on work done previously at Colorado State University [STEVENS ET AL., 2005]. It is freely available in a git repository and published under the GNU license. The prognostic variables in UCLALES are wind, liquid water potential temperature, total water mixing ratio, and scalars. The main formulas solved by UCLALES are

$$\frac{\partial \overline{u}_i}{\partial t} = -\overline{u}_j \frac{\partial \overline{u}_i}{\partial x_j} - c_p \Theta_0 \frac{\partial \pi}{\partial x_i} + \frac{g\overline{\Theta_v^*}}{\Theta_0}\delta_{i3} + f_k(\overline{u}_j - V_{g,j})\varepsilon_{ijk} + \frac{1}{\rho_0}\frac{\partial(\rho_0 \tau_{ij})}{\partial x_j}, \tag{2.37}$$

$$\frac{\partial \overline{\Phi}}{\partial t} = -\overline{u}_j \frac{\partial \overline{\Phi}}{\partial x_j} + \frac{1}{\rho_0}\frac{\partial(\rho_0 \gamma)}{\partial x_j} + \frac{\partial F_\Phi}{\partial x_j}\delta_{j3}, \tag{2.38}$$

with the continuity equation and the ideal gas law, F_Φ a flux, and V_g the geostrophic wind. UCLALES uses the anelastic approximation instead of the Boussinesq-approximation, which allows for a density change with height, but assumes that the density is horizontally and spatially constant. This allows to filter out sound waves without assuming hydrostatic balance, which makes it possible to also simulate deep convection.

The subgrid fluxes are parameterized with the Smagorinsky closure (see section 2.3.1). UCLALES uses periodic horizontal boundary conditions. It is written in Fortran90/95 and parallelized with Message Passing Interface, where the domain is split into sub-domains in the x and y direction. The time stepping is done with the third order Runge-Kutta scheme. The time steps are variable and fulfill the Courant-Friedrichs-Lewy criterion, with an optional maximum value set by the user. The model grid is the Arakawa-C grid. Here, the scalars are defined in the middle of the grid box, while the velocities are shifted by half a grid point. The grid can be stretched in the vertical. For the radiation UCLALES offers various options, ranging from no radiation to full radiation with delta-4 stream radiative transfer. For the surface, free-slip or no-slip conditions can be used, and surface temperature and humidity, fluxes, or gradients can be prescribed. Optionally a surface-model

containing soil layers can be used, which is taken from the Dutch Atmospheric Large-Eddy Simulation model and described in HEUS ET AL. [2010]. The standard microphysics used is a two-moment rain scheme as developed by SEIFERT AND BEHENG [2001] and implemented following STEVENS AND SEIFERT [2008]. More details on UCLALES can be found in the documentation in the git-repository (https://github.com/uclales/uclales).

2.5 Cases Studied

To evaluate models with observations, data from measurement campaigns are taken, where many different variables are measured with a high spatial and temporal resolution. Based on these campaigns, ideal cases can be set up. These idealized, well-defined cases enable models to simulate a simple case without, e. g., a diurnal cycle, increasing the transparency of the cases and allowing intercomparison between models. With the models, processes can then be studied that are difficult to observe in such detail with measurements. The two campaigns used in this thesis are described in the following.

2.5.1 The RICO Case

The first case used in this study is a quasi-equilibrium marine situation. The Rain in shallow Cumulus over the Ocean (RICO) Field Campaign was conducted between November 2004 and January 2005 in the Caribbean near Antigua and Barbuda in the trade wind region [RAUBER ET AL., 2007]. The time and place were chosen to avoid tropical cyclones and to capture shallow cumulus days to understand physical processes in and around those clouds. Measurements were centered near the S-band/Ka-band, dual Polarimetric (S-PolKa) Doppler radar of the National Center for Atmospheric Research and taken in-situ and with remote sensing with three aircrafts, which flew a total of 57 missions. Also, a research ship was used, where the fluxes near the surface were measured and Radiosondes were launched 4 to 6 times a day. A wind profiler gave information about the wind and precipitation, a microwave radiometer measured liquid water path and water vapor path, a ceilometer measured cloud base heights, three radars measured cloud structures, and a lidar measured wind velocities. At a land station in the southeast of Barbuda, rawinsondes and surface observations were conducted. In Antigua and Puerto Rico, three aerosol sampling systems were used, and satellite data was used.

Radar measurements were aiming at collecting a large set of data about cloud development and formation of rain. Two of the aircrafts often flew circular patterns, starting close to the ocean surface, conducting another circle slightly below cloud base and flying one circle at higher altitudes to observe clouds looking down and to deploy dropsondes. Also,

clouds were sampled in between the sets of circles. The third aircraft used its cloud radar to conduct process studies of individual clouds and sampling single clouds repeatedly.

The weather conditions during RICO featured an east-northeasterly wind near the surface of about 7 m / s, sea surface temperatures of about 27 °C, and light precipitation. The atmosphere was on average slightly unstable.

The case constructed on the basis of the measurement campaign used a relatively undisturbed period between the middle of December and the beginning of January, during which the weather conditions did not change much. The mean vertical profiles of potential temperature, water vapor mixing ratio, and horizontal wind components from all Radiosondes are shown in Figure 2.4, together with the initial profiles of the composite case used for LES studies, and cloud condensate and cloud fraction are shown in Figure 2.5. This case now serves as a benchmark case for the community. An intercomparison of LES based on this case was conducted by VANZANTEN ET AL. [2011]. In this thesis, the case serves as a simple idealized case of shallow cumulus clouds.

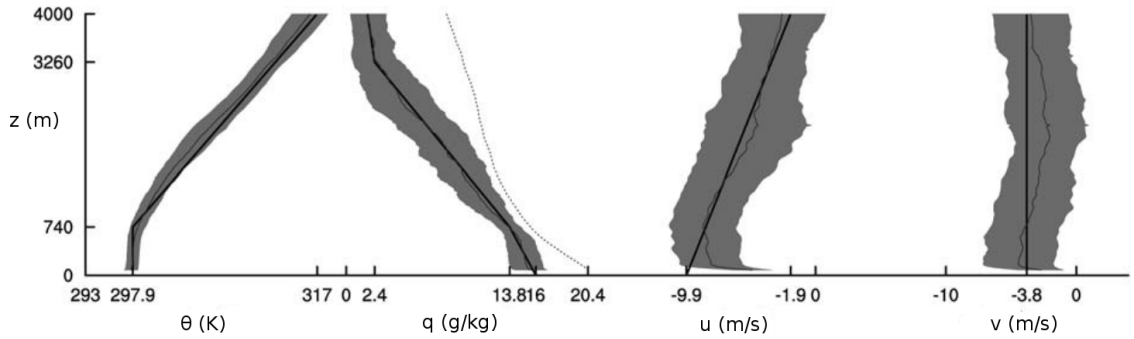

Figure 2.4: Profiles of potential temperature, water vapor mixing ratio, and horizontal wind components, averaged over all radiosondes released at Spanish Point between December 16, 2004, and January 8, 2005 (thin black line), with first to third interquartile range (gray area), mean profile of saturation water vapor mixing ratio (dotted line in second panel), and initial profiles for the composite case (thick black line), adapted from VANZANTEN ET AL. [2011].

2.5.2 The HOPE Campaign

In contrast to the RICO case, as a second campaign we use a case with transient continental conditions, to cover a broad parameter space to aid the process of developing and evaluating a new parameterization scheme. This second campaign is the HD(CP)2 Observational Prototype Experiment (HOPE) within the project High Definition Clouds and Precipitation for advancing Climate Prediction (HD(CP)2), which took place between April 3, 2013, and May 31, 2013, in and around Jülich [MACKE ET AL., 2017]. This campaign was conducted to aid the improvement of the representation of clouds and precipitation in models. The model which the project HD(CP)2 focuses on improving is the

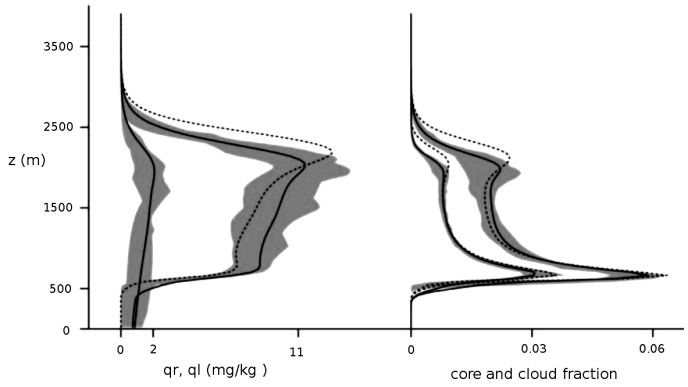

Figure 2.5: Profiles of condensed water q_l, rain water q_r, and cloud and cloud core fraction, from four hours of precipitating (solid line) and non-precipitating (dashed line) simulations, adapted from VANZANTEN ET AL. [2011].

ICON (Icosahedral non-hydrostatic) general circulation model. The HOPE campaign is designed to evaluate the model and to increase understanding about processes subject to parameterization.

Measurements were taken mainly at three supersites: the permanent site JOYCE (Jülich ObservatorY for Cloud Evolution) in Jülich, and two temporary supersites at Krauthausen and at Hambach. These sites form a triangle with a distance between each site of about 4 km. With these sites and some additional instruments in the area, three-dimensional measurements were aimed to cover a cube of about $10 \times 10 \times 10\,\mathrm{km}^3$ with a resolution of about 100 m. The location of the campaign is shown in Figure 2.6. Also shown on the map is the city of Jülich and the hill Sophienhöhe caused by the pit mine nearby. Besides the hill of the pit mine and the low mountain range Eifel south of Jülich, the area is rather flat and dominated by agriculture.

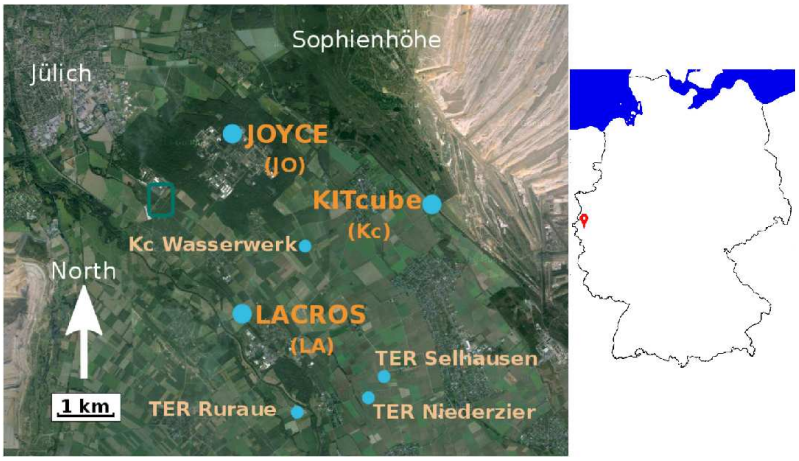

Figure 2.6: Location of the measurement campaign HOPE with the three supersites and smaller sites, adapted from HEINZE ET AL. [2016].

At the supersite in Jülich, the instrumentation from JOYCE is used [LÖHNERT ET AL., 2015]. In Hambach, the Karlsruhe Institute for Technology mobile facility KITcube was used together with a lidar system from the University of Hohenheim, and in Krauthausen, the Leipzig Aerosol and Cloud Remote Observations System (LACROS) was used. In total, the instruments used during HOPE were radiosondes, three cloud radars, three precipitation radars, four Doppler lidars, four Raman lidars, one differential absorption lidar, five microwave radiometers, six sky imagers, 99 pyranometers, and five Sun photometers [MACKE ET AL., 2017]. These instruments provided information about, e. g., the humidity and liquid water distribution, vertical profiles of temperature and humidity, temperature and moisture fluctuations, soil temperature and moisture, wind speed and direction, sensible heat fluxes, cloud base height, aerosols, and microphysics. For a more detailed overview over the instruments see MACKE ET AL. [2017] and LÖHNERT ET AL. [2015].

The time of the campaign was chosen to observe days with low level clouds. During the campaign, warm and cold fronts passed the area, with high pressure conditions in between. On several days, observations were intensified with an increased number of radiosondes and additional measurements, to study the onset of cloud and precipitation formation. Since the weather during the campaign was not homogeneous as in the RICO case, no idealized case based on a typical average day has been set up. Instead, various regimes were measured and single days can be modeled and compared to observations, providing a range of different situations for model evaluation. Consequently, in this thesis the HOPE campaign is used in chapter 5 to study several days to evaluate the cumulus parameterization scheme to realistic cases of shallow cumulus clouds over land.

3 What determines the fate of rising parcels in a heterogeneous environment?

The content of this chapter is published as Brast, M., R. A. J. Neggers and T. Heus (2016), What determines the fate of rising parcels in a heterogeneous environment?, J. Adv. Model. Earth Syst., 8, 1674 - 1690, doi:10.1002/2016MS000750

Abstract

We investigate the potential impact of the local environment on rising parcels in a convective boundary layer. To this end, we use data from an LES simulation of a shallow convective cloud field to feed a parcel model with a range of different local environments, representative of the heterogeneous environment inside a shallow cumulus cloud layer. With this method we can study the statistics of an ensemble of rising parcels, but also the behavior of individual parcels. Through the use of a heterogeneous environment, the interactions between different parcels are indirectly represented. The method, despite its simplicity, allows closer investigation of mechanisms like parcel screening and buoyancy sorting that have frequently been proposed in cumulus parameterization. The relative importance of the entrainment formulation can be assessed, considering various classic entrainment formulations. We found that while the entrainment formulation does affect parcel behavior, the impact of the local environment is significantly more important in determining the eventual fate of the parcel. Using a constant entrainment rate can already explain much of the variation in termination heights seen in nature and LES. The more complex entrainment models then seem to act on top of this mechanism, creating second-order adaptations in the main distribution as established by the heterogeneity of the environment. A parcel budget analysis was performed for two limit cases, providing more insight into the impact of the local environment on parcel behavior. This revealed that parcel screening inside cumulus clouds can be effective in enabling parcels to reach greater heights.

3.1 Introduction

The representation of moist convective processes in global weather and climate models relies on parameterization. The improvement of convective parameterizations is necessary, but difficult to achieve because many processes are not yet fully understood. One such process is the mixing between parcels and their environment [e. g., ROMPS AND KUANG, 2010; DAWE AND AUSTIN, 2013]. This mixing affects the effective vertical transport of heat, humidity and momentum. It affects the radiation budget directly through the vertical distribution of strong greenhouse gases (e. g., water vapor), and indirectly through cloud generation and maintenance. The closure for the mixing process is important, since the representation of convection heavily affects both future climate uncertainty and the skill of numerical weather predictions [e. g., TIEDTKE, 1989; VIAL ET AL., 2013]. This has motivated intense scientific research into mixing and entrainment, which has been ongoing for decades [e. g., SIMPSON AND WIGGERT, 1969; LIN, 1999; GREGORY, 2001; DE ROOY AND SIEBESMA, 2010; ROMPS AND KUANG, 2010; DAWE AND AUSTIN, 2013; DE ROOY ET AL., 2013; TIAN AND KUANG, 2016]. Different methods to study entrainment have been used, e. g., analyzing observational data [JONAS, 1990] or, more recently, using large-eddy simulations (LES) [DAWE AND AUSTIN, 2013; TIAN AND KUANG, 2016]. Various different approaches have been proposed to parameterize entrainment [for a recent review see DE ROOY ET AL., 2013]. For parameterization schemes of convection in large-scale models the debate of the proper closure for the mixing process is still ongoing [e. g., LIN, 1999; NEGGERS ET AL., 2002; SIEBESMA ET AL., 2003; ROMPS AND KUANG, 2010]. The character of the entrainment parameterization depends greatly on the exact definition of the rising parcel. If the approach assumes a bulk parcel, the entrainment formulation should represent the mean entrainment of the population of cloud sizes. On the other hand, when a single parcel is assumed, this parcel represents a single cloud or even a subcloud parcel, rising inside a cumulus cloud. The mixing then represents something very different.

This study focuses on the entrainment of single rising parcels, and not on the bulk entrainment of a whole ensemble of parcel. An idealized picture of a rising parcel assumes that the parcel ascends through a clean, cloud-free environment. The reality is very different, since a parcel can meet a variety of conditions and states, e. g., it can encounter older, decaying clouds [e. g., pulsating growth, HEUS ET AL., 2009]. In case of lateral entrainment, the local environment which the parcel encounters on its way will co-determine how far the parcel will eventually rise. The other factor determining the parcel termination height is the behavior of the entrainment process, affecting the amount of entrained air. A priori, it is not clear which factor will dominate. On the one hand, the local environment can reflect many states. An "unfortunate" parcel, encountering a lot of dry cloud-free air on its

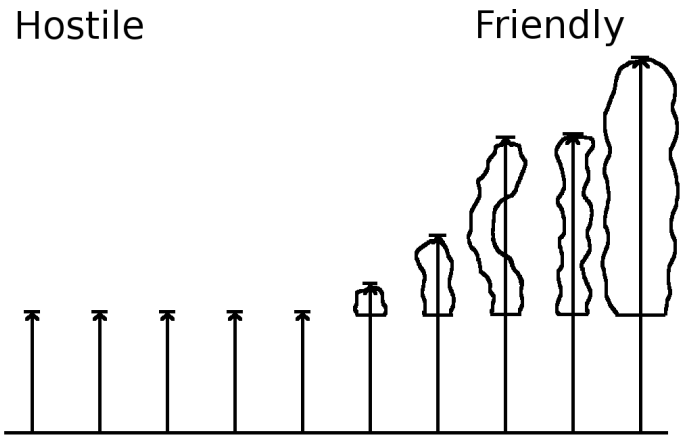

Figure 3.1: Schematic of rising parcels interacting with the local environment. Parcels within a hostile environment stop near cloud base (left side), while parcels within a friendly environment rise higher (right side).

way up, will not rise far, while a "fortunate" parcel, rising inside a cumulus cloud, can be expected to be screened off from hostile environment, thus perhaps having a better chance to rise far. The schematic in Figure 3.1 shows this concept. On the other hand, an entrainment model can interfere with this process, by imposing other dependencies on different variables. Some studies have proposed to represent this "chance effect" of entrainment events by means of a random entrainment [an example for a stochastic model is given in ROMPS AND KUANG, 2010]. However, one wonders if this stochastic effect should then not rather be represented in the air that is entrained (the source), not in the entrainment model itself. Thus, the resulting question is: To what extent is the fate of the parcel determined by the local environment that it happens to meet on its way, and to what extent is it determined by the entrainment?

The aim of this study is to shed light on this problem, and to determine which factor effectively determines the fate of a rising parcel. To do so, we try to separate between the impact of the local environment and that of the entrainment model itself. While some recent studies have intercompared different entrainment models [e. g., CHIKIRA AND SUGIYAMA, 2010] , this separation has received less attention. Many entrainment studies are diagnostic in nature, extracting a relation from data, but refraining from investigating its impact on actual parcel behavior. In this study, different entrainment models are tested in one single rising parcel model. The classic and often-applied rising parcel model by SIMPSON AND WIGGERT [1969, hereafter referred to as SW69] is used for this purpose. The parcel model is fed with a variety of local environments as sampled from an LES of a subtropical marine trade-wind cumulus cloud field. These local environments may represent i) dry cloud-free conditions, ii) cumulus clouds, iii) or any state in between, including partially cloudy conditions. This way, the variability in thermodynamic states typical of a shallow cumulus cloud layer is fed to the rising parcel model. The next step is then to test various

Table 3.1: Entrainment formulations from the literature

Reference	Entrainment formulation
Simpson and Wiggert (1969)	$0.2/R$
Siebesma et al. (2003)	$1/z$
Soares et al. (2004)	$c\left(\frac{1}{z+\Delta z}+\frac{1}{(z_i-z)+\Delta z}\right)$
Neggers et al (2002)	$\eta/(\tau w)$
Lin (1999)	λB^{α}

entrainment models as proposed in the literature, including dependencies on height, vertical velocity, buoyancy, and stochastics. The constant entrainment rate model is used as a limit case, allowing assessment of the impact of purely the different environments on the rising parcel.

In section 3.2, a brief review of different entrainment models is provided. In section 3.3 the parcel model is then formulated, and the experiment setup is described. Section 3.4 presents the results, followed by a discussion and summary of the findings in Section 3.5.

3.2 A Short Review of Entrainment Models

In any investigation of the behavior of rising parcels, the entrainment process should play a central role. Since entrainment is difficult to measure, LES simulations of case studies are often used to design parameterizations of entrainment. In the literature, many different entrainment closures have been proposed, featuring dependencies on a variety of variables [for a review see DE ROOY ET AL., 2013], for both plumes and parcels (from now on we will use the term "parcel", see also sec. 3.3.1). An overview of some of the better known formulations is given in Table 3.1.

Based on laboratory and analytical considerations, SW69 hypothesized that the entrainment should be inversely related to the radius of the cloud R, with ε the fractional entrainment rate. For simplicity, they assume the radius of the cloud to be constant with height. TIEDTKE [1989] use the same parameterization and assume an average cloud radius to get a constant entrainment rate, differentiating only between two different cumulus cloud regimes.

Another approach is to relate entrainment rate to height. SIEBESMA ET AL. [2003] found in LES studies that entrainment is decreasing with height. They use this dependency to formulate the entrainment as inversely proportional to the height above the surface z. SOARES ET AL. [2004] use a slightly more complex parameterization based on LES results, where entrainment is dependent not only on height but also on boundary layer height z_i, with $c = 0.5$ and Δz the vertical grid spacing, whereas SIEBESMA ET AL. [2007] use a

similar parameterization with a value of $c = 0.4$.

NEGGERS ET AL. [2002] proposed an inverse dependency on the vertical velocity of the rising parcel w, featuring a turnover scale τ. τ is argued to represent the typical lifetime of a rising parcel, found to be 400 s based on LES results. With this formulation, parcels with a high vertical velocity have a low entrainment rate, enabling them to rise high.

The buoyancy sorting concept used as a parameterization scheme for shallow cumulus in KAIN AND FRITSCH [1990] sees the cloud edge not strictly as cloudy or non-cloudy air. Eddies disturb the cloud edge, creating different mixtures of cloudy and non-cloudy air. Depending on the fraction of cloudy air in the mixture, the buoyancy of these mixtures differs. Mixtures with a high percentage of environmental air have a negative buoyancy, while mixtures with mostly cloudy air have a positive buoyancy compared to the environment undisturbed by clouds. Positively buoyant mixtures are assumed to entrain into the cloud, while negatively buoyant mixtures detrain from the cloud. To determine the threshold between positively and negatively buoyant mixtures, a critical mixing fraction is calculated taking into account environmental factors such as temperature and humidity. This model was further developed and applied by BRETHERON ET AL. [2004] and PARK [2014a]. The critical mixing fraction of the buoyancy sorting framework is also used by DE ROOY AND SIEBESMA [2008] to calculate the detrainment. GREGORY [2001] use buoyancy in their entrainment formulation in combination with vertical velocity. A simpler approach is taken by LIN [1999] [also used in JENSEN AND GENIO, 2006], where $\varepsilon = \lambda B^{\alpha}$, with the constants λ and $\alpha = -1.27$, and B the buoyancy.

ROMPS AND KUANG [2010] found that a stochastic parameterization of entrainment, in contrast to a constant entrainment rate, is able to represent the observed variability between updrafts. This variability depends mostly on the variable entrainment rate during the ascent and much less on the conditions at cloud base. For their eddy-diffusivity/mass flux model, SUŠELJ ET AL. [2013] also use the stochastic approach, but with a constant entrainment rate below the level of condensation.

This study uses a variety of entrainment models, comparing them all in the same setup. Entrainment formulations with dependencies on height, buoyancy, vertical velocity and stochastics are compared to a constant entrainment rate. This choice gives a broad spectrum of different concepts. Details about the entrainment formulations are described in section 3.3.

3.3 Method

We study parcel behavior by looking at a rising, entraining parcel model, with the set of equations coded as a standalone program. The parcel model is fed with vertical profiles diagnosed from the 3D field of the LES. Different entrainment closures are applied and the results are intercompared.

3.3.1 Parcel Model Formulation

A parcel is defined here to represent an infinitesimally small particle, much smaller than the coherent structures of the turbulent field in which it rises. We assume that the parcel's life time is much shorter than the advective tendency of the bulk boundary layer, which motivates assuming steady state. The associated parcel model equations therefore describe the net change of the properties of such a small particle as it rises through the turbulent field. As the particle is infinitesimally small, carrying no mass, its area fraction is not considered. This approach is not unprecedented [e. g., NEGGERS ET AL., 2002; ROMPS AND KUANG, 2010]. In addition, we assume that the parcel model also holds for small scales.

Accounting for these assumptions, the parcel model based on SW69 can be written as [SIEBESMA ET AL., 2007; NEGGERS ET AL., 2009]

$$\frac{\partial \Phi_u}{\partial z} = -\varepsilon_u(\Phi_u - \Phi_e) \tag{3.1}$$

$$\overbrace{\frac{1}{2}(1-2\mu)\frac{\partial w_u^2}{\partial z}}^{acc} = \overbrace{-b\varepsilon_u(w_u^2 - w_e^2)}^{mix} + B_u \tag{3.2}$$

$$B_u = \frac{g}{\overline{\Theta_v}}(\Theta_{v,u} - \Theta_{v,e}) \tag{3.3}$$

with Φ a conserved thermodynamic variable for moist adiabatic ascent (total specific humidity q_t or liquid water potential temperature Θ_l), ε_u the effective mixing rate, $\mu = 0.15$ and $b = 0.5$ proportionality constants for drag [e. g., ROMPS AND CHARN, 2015] and mixing, B the buoyancy, g the gravitational acceleration, Θ_v the virtual potential temperature, and $\overline{\Phi}$ the mean over the whole domain. "Acc" stands for the effective acceleration term, which includes the pressure homogenization, and "mix" denotes the mixing term. While we are aware that there are different values of μ and b used in the literature, DE ROODE

ET AL. [2012] found that though our values might not be optimal for the RICO case, a range of values for μ and b will only result in small errors.

At this point we make some additional assumptions. The first concerns the source of entrained air, which is assumed to originate locally, adjacent to the parcel. This can be interpreted as an indirect way of introducing interactions with other parcels into the model. The properties of such parcels can differ greatly from the passive, cloud-free environment, for example when the adjacent air (or parcel) also sits inside a cumulus cloud. This sets this model apart from most previous multiparcel models, in which the parcels only interact with the passive environment. In practice, to achieve this interaction, the profiles of all grid columns as sampled from a fine-scale cumulus resolving model (LES) are given to the off-line rising parcel model. This should reveal how a rising parcel can react to different local environments. During its ascent the parcel is continuously diluted with air from the instantaneous LES column inside which it is rising; in (3.1) - (3.3) subscript "e" is replaced by "Lc" (LES-column) to reflect this lateral mixing model involving locally entrained air.

By using "Lc" in eq. (3.3), B_u becomes a local buoyancy, describing the excess over the local environment. This is very different from a mean buoyancy which describes the buoyancy over the horizontal mean. The key difference is that parcels experience the local environment also in the buoyancy. It is to be expected that parcels sitting inside a buoyant LES cloud (i. e. mean buoyant) will not have a large local buoyancy.

The second assumption is that the parcels rise only vertically, not laterally. Alternatively, one could choose to use LES trajectories of rising parcels instead, which perhaps would better follow rising cumulus clouds during their life cycle. However, this approach is also not without problems. For example, model parcels which mix differently compared to the actual rising parcel will start to deviate from this trajectory. We therefore consciously adopt a simpler approach, by only considering purely vertical columns. While this simplifies the analysis, it still confronts the parcel model with many different environments; this should be sufficient for studying the potential impact of heterogeneous air on the fate of the parcel, and give insight into mechanisms like parcel screening and buoyancy sorting. The use of many different, but representative profiles allows a statistical assessment of parcel behavior.

The rising parcel model is thus vertically integrated with the environmental properties obtained from sampled columns from instantaneous 3D LES fields. With this setup, we follow three aims:

- to confront the classic rising parcel model with a heterogeneous environment, representative of a shallow cumulus cloud field,
- to investigate the occurrence of parcel screening and buoyancy sorting mechanisms,

- and to explore the additional impact of the entrainment formulation.

This study exclusively focuses on gaining more insight into parcel model behavior in situations in which it might encounter different local environments. The use of a heterogeneous environment, which can be interpreted as introducing interactions between parcels, has not been a feature in most previous parcel models. In the mixing term, two factors can a priori be distinguished that can play different roles concerning the ascent of the parcels. The first factor, the local environment, has varying effects. Inside an LES cloud, where the difference between the parcel and the LES column can be small, the dilution is small, minimizing deceleration due to mixing. On the other hand, when a parcel leaves the LES clouds, the mixing can decelerate the parcel. The second factor, the entrainment, is given by the closure of the model. Beforehand it is not clear which factor will dominate. Therefore, to understand the behavior of the parcels we will investigate which factor dominates and has the larger effect on the ascent of the parcels.

3.3.2 Experiment Setup

For this study the SW69 rising parcel model is provided with vertical profiles as sampled from the LES model UCLALES [STEVENS ET AL., 2005]. The LES-columns are sampled from the instantaneous 3D fields of temperature, humidity, and vertical velocity, which are then used as the environmental variables appearing in eqs. (3.1) - (3.3). We stress that the parcel calculation does not affect the LES in any way.

For testing the SW69 rising parcel model the Rain In shallow Cumulus over the Ocean (RICO) case was chosen [RAUBER ET AL., 2007], as it represents a clean undisturbed case of marine shallow cumulus. The campaign took place from November 2004 to January 2005 near Antigua and Barbuda in the Atlantic Ocean in the trade wind region. Measurements were conducted by three aircrafts, one research ship and land stations. LES simulations based on this case have been intercompared and confronted with measurements [VANZANTEN ET AL., 2011], showing that LES models do well in reproducing its key features.

After 9 h the spin-up time of the simulation has passed. The time period selected for analysis in this study therefore starts at 9 h and ends at 12 h, which gives enough data for analysis without being computationally very costly. During these three hours, every 200 s the LES profiles of all columns are given to the parcel model. The simulated model domain is $14\,\text{km} \times 14\,\text{km} \times 4\,\text{km}$ with a resolution of 100 m in the horizontal and 40 m in the vertical, which is the same resolution as used by VANZANTEN ET AL. [2011]. The UCLALES model we use has a Smagorinsky type subgrid scheme and was part of the intercomparison in VANZANTEN ET AL. [2011].

Table 3.2: Root-Mean Square Error of the best fit for various entrainment models

Entrainment model	Parameter	Best Fit	RMSE
Constant	c	1/70	0.0112
1/w	τ	100	0.0099
1/z	c	50	0.0112
1/B	λ	1.2×10^{-6}	0.0095
Stochastic	c	1/25	0.0096

The rising parcels are initialized at the lowest model layer with

$$\Phi_u(x,y) = \overbrace{\overline{\Phi_{Lc}(x,y)}}^{environment} + \overbrace{\Delta\Phi}^{surface\ perturbation}, \tag{3.4}$$

$\Delta\Phi$ the surface perturbation, and $\overline{\Phi}$ the mean over the grid cell. This formulation gives all parcels an initial excess of Φ and thereby ensures that all parcels reach the cloud layer. The parcel initialization height is assumed to be situated inside the surface layer, so that a constant flux with height can be used, which means that the perturbation can be written as

$$\Delta\Phi = c\,\overline{w'\phi'_{sfc}}/\sigma_w, \tag{3.5}$$

as proposed by TROEN AND MAHRT [1986], where σ_w is calculated using the relation proposed by HOLTSLAG AND MOENG [1991] and c is a scaling factor. We choose to keep c constant for simplicity to be able to assess only the variability of the environment. This procedure is fully described in the ECMWF IFS documentation, Part 4, Chapter 3. This initialization procedure is also used in NEGGERS ET AL. [2009]. Condensation within the parcel follows the common method used in SOMMERIA AND DEARDORFF [1977].

3.3.3 Implementation Details

Next, the details of the implementation of the entrainment models as listed in Table 3.2 are briefly discussed:

- The first, simplest possible entrainment model assumes the entrainment to be a constant c for all parcels.
- For the dependency on height, the model by SIEBESMA ET AL. [2003] is used, where $\varepsilon = c\,(1/z)$ and c is a constant to be calibrated.
- The model by LIN [1999] is used for the buoyancy dependency, where $\varepsilon_i = \lambda B_{i-1}^{\alpha}$. Here, i denotes the level where the entrainment is calculated. Since we need the

entrainment to calculate the buoyancy of the current level, the buoyancy of the previous level is used. We choose $\alpha = -1.27$, which LIN [1999] found to be a good constant value for α and which we found to be suitable for this study as well. The constant to be calibrated here is λ. We use the buoyancy from the LES model, i. e., the local environment, to calculate the entrainment only if the buoyancy is positive. In previous studies [e. g. JENSEN AND GENIO, 2006], the parcel stops at the level of neutral buoyancy. To ensure that the parcels in our study do not continue to rise with a negative buoyancy, we set the entrainment rate for negative buoyancies to a high value of 0.1. This value is arbitrary, but the results are not sensitive to this value so we assume it to be reasonable.

- For the vertical velocity dependency the model by NEGGERS ET AL. [2002] is used: $\varepsilon = \eta/(\tau w)$, with w the vertical velocity of the parcel, η a calibration factor, which in this study is set to one, and τ the turnover time scale, which is to be determined.

- To include a stochastic model, we developed a very simple model inspired by ROMPS AND KUANG [2010]. We implemented the model in a way that gives the highest variability, since the increased variability is the main characteristic of this model compared to the other models. Therefore, we calculated the entrainment rate for each parcel only once at the beginning: $\varepsilon = c\,r$. c is the constant to be calibrated and r is a random number picked from a gamma distribution $f = \frac{y^{\alpha-1}e^{-y/\theta}}{\theta^{\alpha}\Gamma(\alpha)}$ after MARSAGLIA AND TSANG [2000], where the normal distribution needed for the calculation of the gamma distribution is calculated with the Marsaglia polar method [MARSAGLIA AND BRAY, 1964]. For the gamma distribution, two parameters need to be specified, the shape parameter α and the scale parameter θ. For the highest variability in entrainment we chose $\alpha = 2$ and $\theta = 0.5$, which puts the average of the function at 1 and thus makes the calibrated parameter c comparable to the constant entrainment rate.

Since the main goal is to evaluate the dependency of parcel state on a range of different variables, simple formulations are used to facilitate the interpretation. The main constant in each formulation is calibrated so that the vertical profile of the number of parcels still rising best matches the cloud fraction profile in the LES (described in detail in the next section). This means that here it is implicitly assumed that all cloudiness in the RICO case is associated with rising parcels. Although this assumption is certainly simplistic, the main aim here is to capture the typical vertical structure of the number of rising parcels in the cloud layer. We chose the minimum RMSE to calibrate the entrainment models instead of using the constants from the literature because i) the constants in the literature are often determined for whole cloud populations, not single parcels, resulting in a conceptual mismatch, ii) in the literature different cases are used to calibrate the models, whereas we study the RICO case for all models, independent of the cases for which the models were designed, and iii) each entrainment model should be given a chance to perform at its best.

The details of this calibration are described in the next section. It should be noted that our main goal is to document parcel behavior, and its dependence on the environment as well as on the entrainment model. The detailed discussion of each entrainment model itself, as well as its possible applicability, is not in the scope of this study; for this we refer to the individual publications that describe each model (see section 3.2).

3.4 Results

3.4.1 Cloud Fraction

The "cloud area fraction" for i) the LES, $a_c^{LES}(z)$, and ii) for the parcels, $a_c^{parcels}(z)$, is defined as

$$\begin{aligned} a_c^{LES}(z) &= \frac{1}{N_x N_y} \sum_{i=1}^{N_x} \sum_{j=1}^{N_y} I^{LES}(i,j), \\ a_c^{parcels}(z) &= \frac{1}{N_x N_y} \sum_{i=1}^{N_x} \sum_{j=1}^{N_y} I^{parcels}(i,j), \end{aligned}$$

respectively, with I an indicator function defined as

$$\begin{aligned} I^{LES}(i,j) &= \begin{cases} 0 & \text{for} \quad q_l = 0 \\ 1 & \text{for} \quad q_l > 0 \end{cases}, \\ I^{parcels}(i,j) &= \begin{cases} 0 & \text{for} \quad z > z_t(i,j) \\ 1 & \text{for} \quad z \leq z_t(i,j) \end{cases}, \end{aligned}$$

with z_t the termination height of the parcel. The cloud area fraction defined here describes the fraction of those grid boxes containing parcels, which have a negligible size inside the grid box (see sec. 3.3.1). As argued above, the fractions $a_c^{LES}(z)$ and $a_c^{parcels}(z)$ are for simplicity considered to be comparable, because the parcels condense above cloud base and resemble the cumulus clouds in RICO, where most clouds are convective and surface-driven.

Figure 3.2 shows the ability of the entrainment models to reproduce the cloud fraction profile of the LES. In the LES the lifting condensation level (LCL) is between 600 m and 700 m. Above the LCL there is a maximum in cloud fraction, with a decrease with height

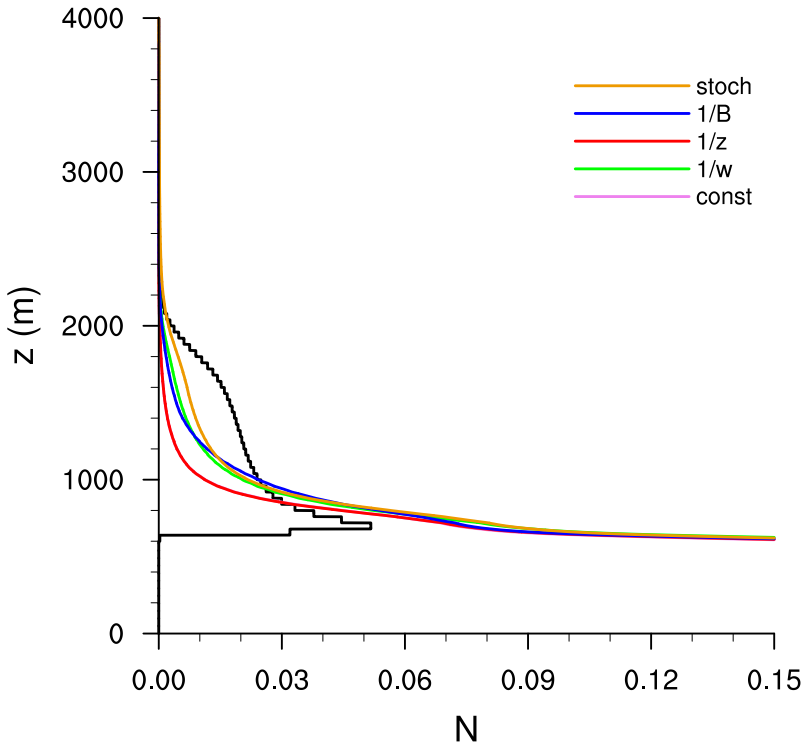

Figure 3.2: Profiles of cloud fraction for the simulations with entrainment models depending on a constant, on vertical velocity, on height, on buoyancy, and on stochastics, and profile of the LES cloud fraction. The normalized number of cloudy grid boxes of the LES for each level (solid black line) and the normalized number of rising parcels inside columns with an LES cloud for the five different models (colored lines) are shown, averaged over the analysis time.

and the highest clouds reaching about 2200 m. Similar profiles of the cloud fraction were found by VANZANTEN ET AL. [2011] and SIEBESMA AND CUIJPERS [1995].

Differences exist between $a_c^{LES}(z)$ and $a_c^{parcels}(z)$ throughout the subcloud layer, since the parcels start to rise at the surface and the fraction is constant in the subcloud layer for all entrainment models. The heights of cloud base and cloud top are mostly well captured, but all entrainment models overestimate the cloud fraction near cloud base and underestimate it higher up. However, though there are differences in the ability of the models to represent the vertical structure, all models are able to reproduce the cloud fraction to some degree.

To quantify the capability of the entrainment models to capture the vertical structure, the following root mean square error is calculated:

$$RMSE = \sqrt{\frac{1}{Z}\sum_{z=1}^{Z}(N_u(z) - N_{Lc}(z))^2} \tag{3.6}$$

with Z the number of horizontal levels that are taken into account and N_u and N_{Lc} the

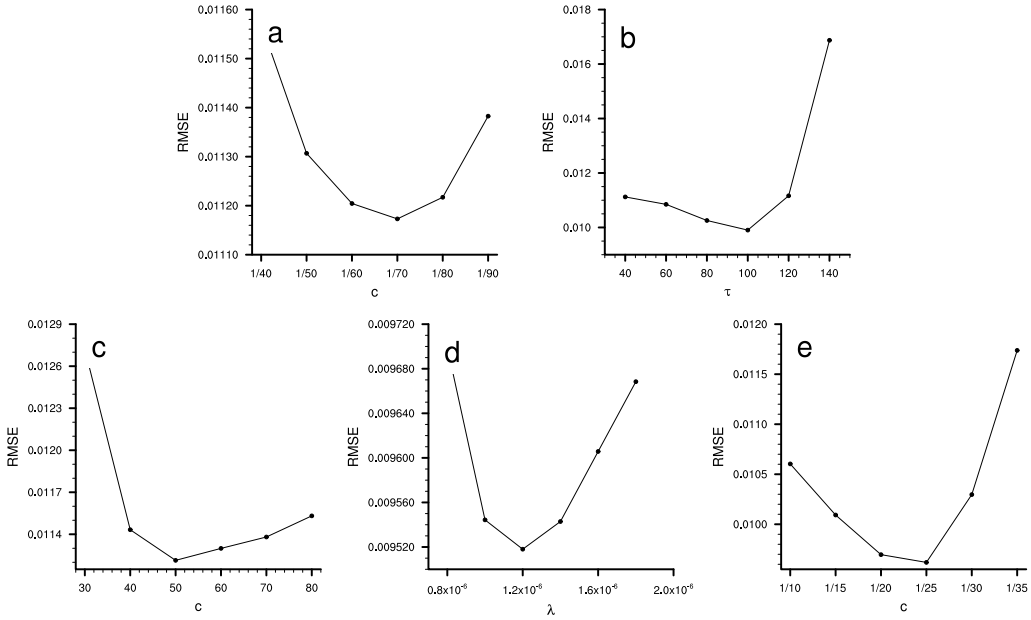

Figure 3.3: RMSE for varying parameters of entrainment models which depend on a constant (a), on vertical velocity (b), on height (c), on buoyancy (d), and on stochastics (e).

number of updrafts and cloudy grid boxes at each level, respectively. The vertical range in which this evaluation takes place is defined by the maximum cloud fraction of the LES as the lower boundary, and the top of the LES cloud fraction as the upper boundary.

Using this RMSE, a parameter optimization was performed by varying the constant parameters of the entrainment formulations and comparing the cloud fraction of the parcels to the LES cloud fraction. The RMSE for the different entrainment models are displayed in Figure 3.3. From this analysis, the parameter giving the smallest RMSE was chosen for each entrainment model. Though there is some variation among the vertical profiles produced by the various entrainment models, which is reflected by the RMSE, it is relatively small since all entrainment models yield the same basic decreasing cloud fraction with height. A summary of the optimized parameters is given in Table 3.2. These parameters differ slightly from the parameters in the literature. For the vertical velocity dependency, τ is smaller than proposed by NEGGERS ET AL. [2002] based on an analysis of whole clouds; in our application a lower τ is required to make parcels stop at cloud base. For the same reason, the value for c in the height dependent formulation as well as λ in the buoyancy dependency and c in the constant formulation are slightly larger than the values in the literature. Our stochastic formulation deviates too much from the original formulation by ROMPS AND KUANG [2010] to allow a direct comparison.

By finding the most suitable parameter, we prepared the entrainment models such that each model is calibrated to this specific application and case. Since the main goal of our study is to investigate the behavior of the parcels, we limit the number of different

parameters tested, which is nevertheless detailed enough for a comparison of the different entrainment models.

Beside cloud fraction, another way to compare the entrainment models is by looking at the variability among parcels for each model. To this purpose we calculated the variance among the rising parcels:

$$\sigma_{q_t}^2 = \frac{\sum_{q_t}(q_{t,u}(z) - \overline{q_t}(z))^2}{n(z)}, \tag{3.7}$$

with n the number of rising parcels present at height z, $q_{t,u}$ the total specific humidity of the parcel and $\overline{q_t}$ the average over all rising parcels. Thus, for each level we only take into account those parcels that are still rising. The behavior of the parcels is influenced by both q_t and Θ_l. In the following we will only show the results for q_t for brevity.

In Figure 3.4 the humidity variance is used to compare the different entrainment models. All entrainment models show the same order of magnitude for the variance. The entrainment model depending on the buoyancy exhibits one of the larger spread among the parcels. We hypothesize that the underlying mechanism of this behavior is the buoyancy sorting concept [KAIN AND FRITSCH, 1990]. When a group of parcels rises inside an LES cloud, the LES buoyancy is large, implying weak dilution of the rising parcels when using this entrainment model. However, as soon as a parcel leaves the cloud, the LES buoyancy B_{Lc} becomes small, so that the parcel starts to dilute more efficiently. Parcels thus become very sensitive to their environment, with the buoyancy-based entrainment model amplifying the impact of the environment that we already see with the constant entrainment model. The peak in the variance near cloud top for the formulations depending on a constant and height are due to a small number of still rising parcels.

It is interesting to note that the variance of the stochastic approach and the constant entrainment have similar magnitudes. More insight into the buildup of the variance among parcels is provided by Figure 3.5, showing the difference in variance between a subset of parcels, of which the termination height is equal to or higher than 1800 m, and all rising parcels. Here, 1800 m is chosen as a height defining high reaching parcels. For the subset of high-reaching parcels the variance at lower levels is smaller; this holds for all entrainment models. This suggests that the properties of high reaching parcels are more similar during their ascent compared to the full ensemble. Apparently, these parcels are screened off from the hostile cloud-free environment by the local environment which supports the ascent. This result further confirms that the local environment has a strong influence on the rising parcels. Especially the variance of the entrainment models depending on buoyancy and vertical velocity is smaller for the high-reaching subset. The vertical velocity dependency exhibits a positive feedback since increasing vertical velocity

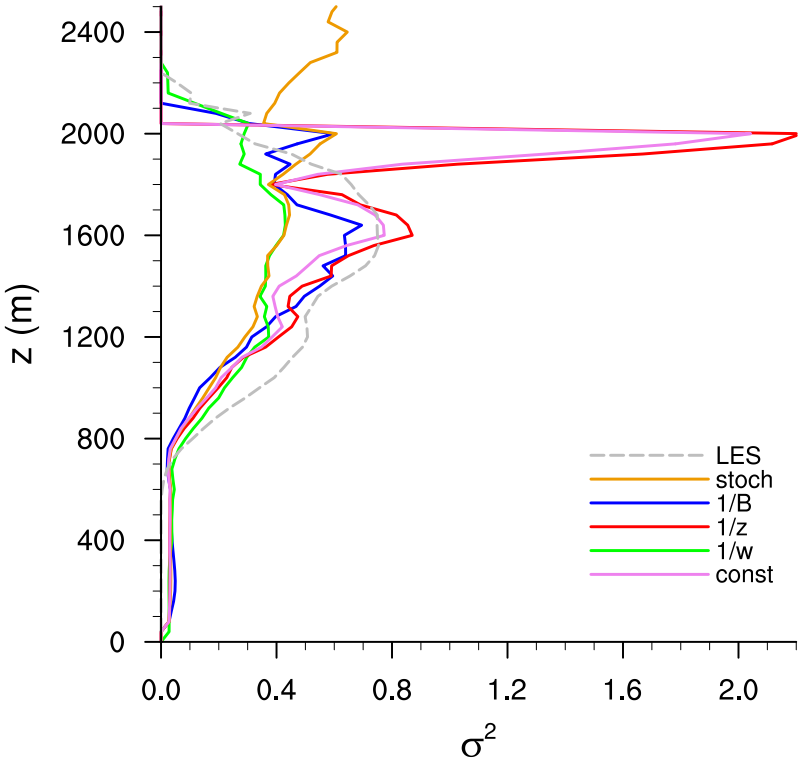

Figure 3.4: q_t-variance for the five entrainment models for all rising parcels with the LES variance as a reference.

decreases the mixing rate which in turn supports an increasing vertical velocity. A higher buoyancy stimulates an increased vertical velocity, resulting in a similar behavior of those two entrainment models.

3.4.2 Differences Among Parcels

To better understand the differences between rising parcels we now segregate the behavior of parcels as a function of their termination heights. In this and the following analyses we only consider the simplest entrainment model with a constant entrainment rate. The argumentation for this is that it highlights the role of the environment; the secondary dependence on the entrainment model as reported earlier also justifies this choice.

Figure 3.6 shows the median q_t-Profile of all parcels, as well as the spread among them. When categorized into different termination heights with bins of 200 m (Fig. 3.7), several differences become apparent. With increasing termination height, the interquartile range increases slightly, probably because more variable local environments are encountered. Also, the high reaching parcels are more successful in maintaining their humidity. Apparently, parcels with a high humidity are more successful in rising far. For the two highest bins, this difference is not present at all heights due to the relatively small number of

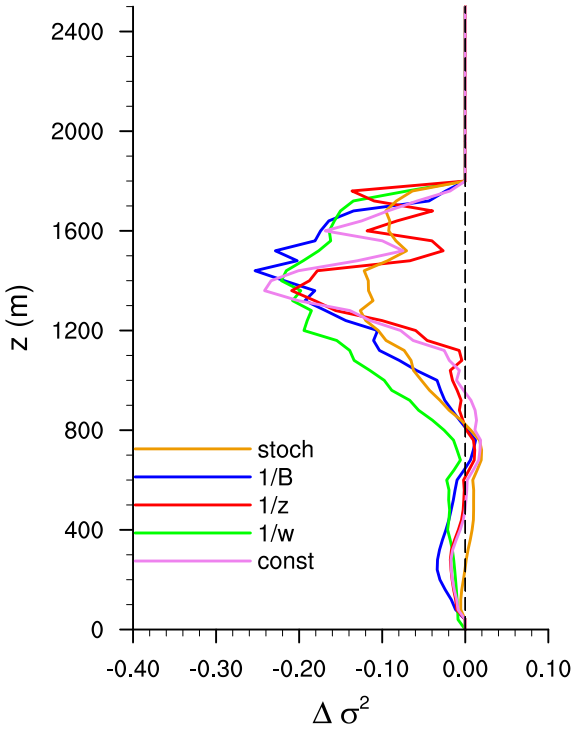

Figure 3.5: Difference between the q_t-variance of parcels reaching at least 1800 m and all rising parcels for the five entrainment models.

high-reaching parcels. The humidity is mainly influenced by the local environment, which again illustrates the importance of the local environment on the behavior of the rising parcels. At lower levels below cloud base, all bins have a similar humidity (Fig. 3.8 (a)) because all parcels were initialized the same. The difference between the parcels is caused by the different environments they encounter.

From this analysis, the effective mixing for each bin can be quantified by using equation (3.1) to yield

$$\begin{aligned} \varepsilon_{bin}^{b} &= -\frac{\frac{\partial}{\partial z}\langle q_{t,u}\rangle^{b}}{\langle q_{t,u}\rangle^{b} - \overline{q_t}} \\ &= \frac{\langle \varepsilon_u \left(q_{t,u} - q_{t,Lc}\right)\rangle^{b}}{\langle q_{t,u}\rangle^{b} - \overline{q_t}} \end{aligned} \tag{3.8}$$

and discretized

$$\varepsilon_{bin}^{b} \approx -\frac{\frac{q_{t,u}(z_2) - q_{t,u}(z_1)}{z_2 - z_1}}{q_{t,u}(z_1) - \overline{q_t}(z_1)} \tag{3.9}$$

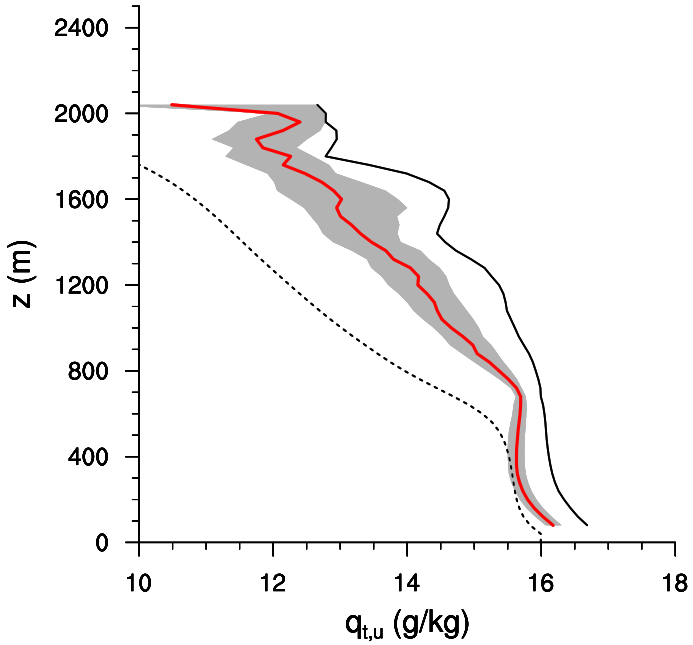

Figure 3.6: Median of q_t for all rising parcels (red), interquartile range (gray), maximum q_t for each level (solid black) and mean q_t of the local environment (dashed black).

where $\langle\rangle^b$ indicates the mean over all parcels in bin b, and $\overline{(..)}$ indicates the horizontal mean over the whole domain. Note that ε^b_{bin} is conceptually different from the entrainment rate for individual parcels ε_u: the former represents the entrainment rate needed to reproduce the mean of the bin with a bulk parcel model that acts on the horizontal mean $\overline{q_t}$. We adopt this definition to allow comparison of our results with previous studies of bulk entrainment.

To calculate the entrainment with eq. (3.9) we used $z_1 = 800\,\mathrm{m}$ and $z_2 = 1360\,\mathrm{m}$ as upper and lower heights for all bins. The upper level was chosen because it is the top of the parcels from the lowest bin. The results were found not to be sensitive to this choice (not shown). The resulting entrainment rates for all bins are compared in Figure 3.8 (b). The bin of the fortunate, highest rising parcels has a low entrainment rate, enabling them to rise far, while the bin with the unfortunate parcels has a high entrainment rate. The range of entrainment rates lies between $0.0015\,\mathrm{m}^{-1}$ and $0.003\,\mathrm{m}^{-1}$. In the literature, similar values were found for bulk population statistics [SIEBESMA AND CUIJPERS, 1995].

3.4.3 Case Studies

To gain more insight into the relation between parcel and local environment, two individual parcels with very different properties are selected as opposing case studies. Parcel state variables and budget terms will be investigated, focusing on the differences between

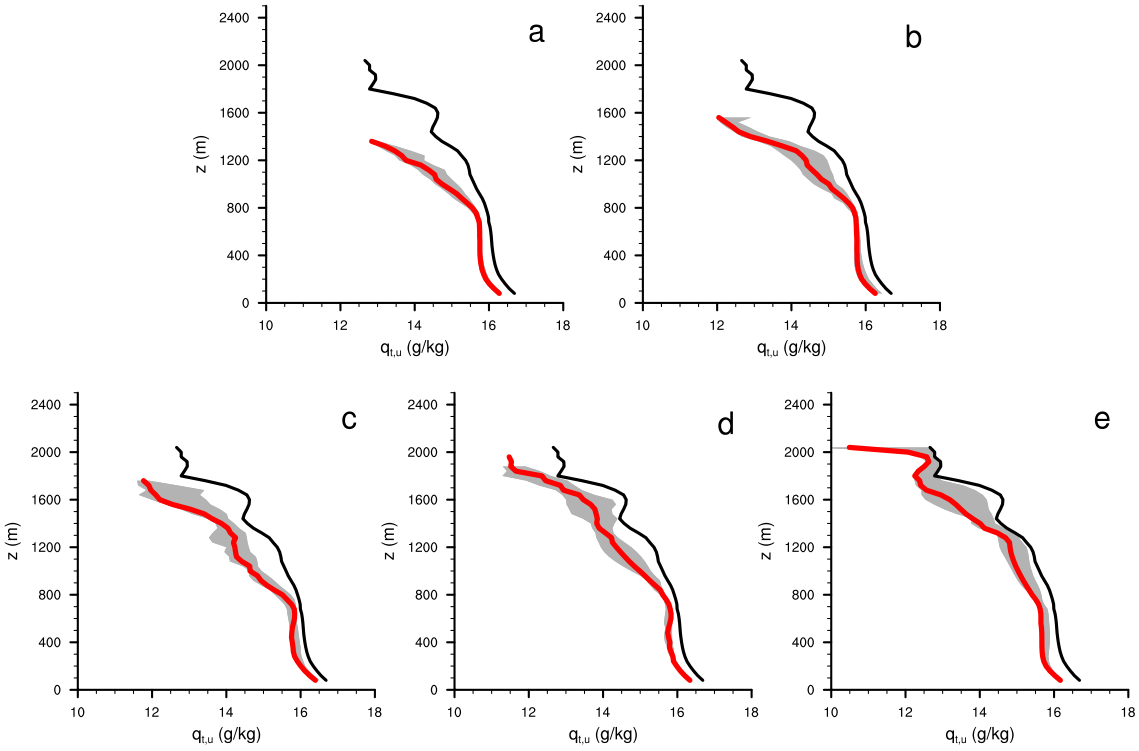

Figure 3.7: Median of q_t for all rising parcels (red), interquartile range (gray), maximum q_t for each level (solid black) for all rising parcels that reach between 1200 m and 1400 m (a), 1400 m and 1600 m (b), 1600 m and 1800 m (c), 1800 m and 2000 m (d), 2000 m, and 2200 m (e).

these two parcels. This should provide insight into what causes the net behavior of a parcel in general, and its response to its direct environment.

The Fortunate Parcel

The first case is a parcel with one of the highest maximum vertical velocities, which falls in the bin of the highest reaching parcels as discussed in the previous section. This column is interpreted as an example of a strong updraft with a high vertical velocity and a high termination height, rising in the most favorable environment and therefore called "fortunate parcel". These strong parcels are relatively rare [PLANK, 1969] but are illustrative to study. The LES cloud in which this updraft is embedded is shown in Figure 3.9 (a). The profiles of vertical velocity and q_t-excess of the parcel over the environment as well as the profiles of the buoyancy and $w'q_t'$ (solid lines) are shown in Figure 3.10. The high termination height of this parcel is associated with a high vertical velocity, increasing until about 2000 m. Up to that height, the q_t-excess is small, being first slightly positive and above 1600 m becoming slightly negative, indicating a small q_t difference between the parcel and its direct environment. This behavior is caused by the presence of an LES cloud

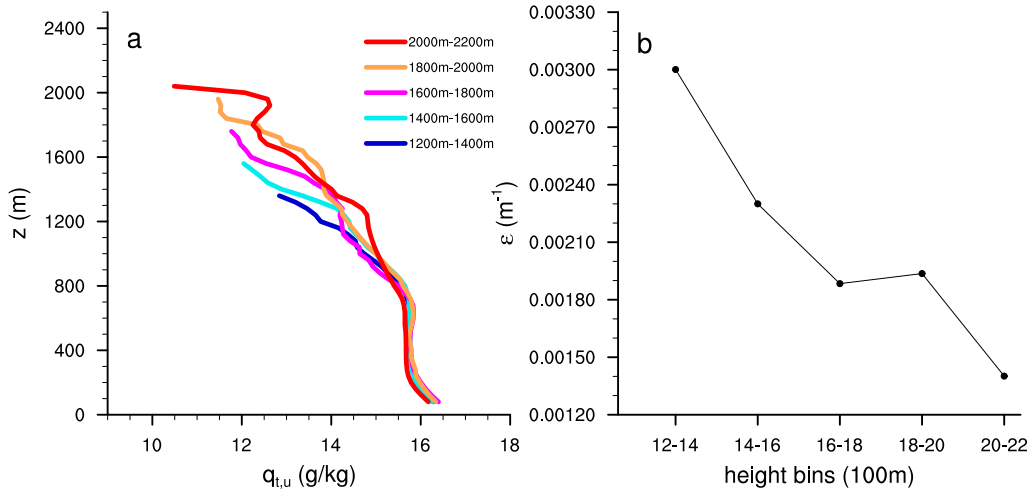

Figure 3.8: Median of q_t (a) and bulk entrainment rate (b) for different height bins for the model with constant entrainment.

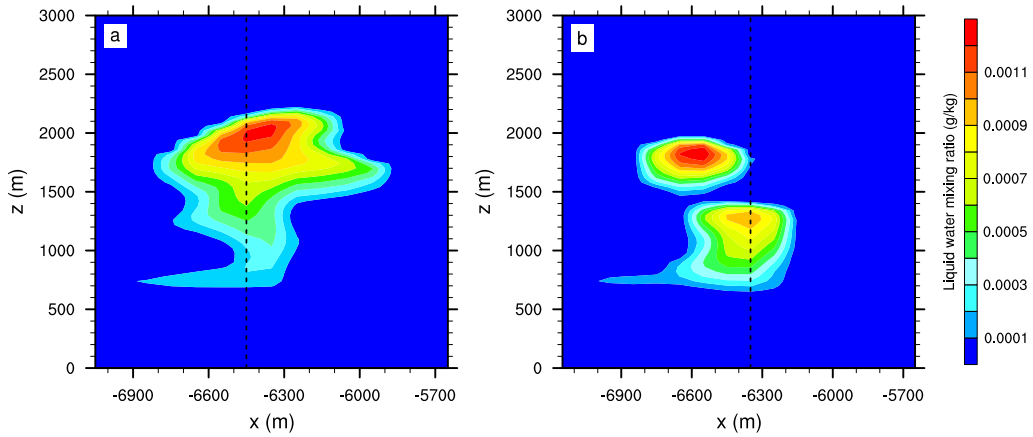

Figure 3.9: Part of a vertical cross section of the liquid water mixing ratio of the LES around (a) the fortunate parcel and (b) the less fortunate parcel (dashed line is the location of the studied columns shown in Fig. 3.10).

in the column, associated with a relatively high $q_{t,Lc}$. The buoyancy B_u is slightly positive for most of the ascent of the parcel. Near its termination height the parcel vertical velocity decreases rapidly while the q_t-excess increases rapidly. This probably reflects the parcel overshooting out of the LES cloud. At the top of the LES cloud the $q_{t,Lc}$ decreases abruptly (not shown), causing the difference between the parcel and its environment to increase. Near the termination height the negative B_u contributes to the stopping of the parcel.

The product $w'q_t'$ is shown in Figure 3.10 (d), expressing the impact on vertical transport. The profile closely resembles that of the q_t-excess, with a very small positive value until a height of about 1600 m and a slightly negative value between 1600 m and 2000 m. (Note that this product represents the hypothetical transport relative to the *direct* environment; the parcel is "sailing" on top of an LES cloud. Accordingly, a negative local value could

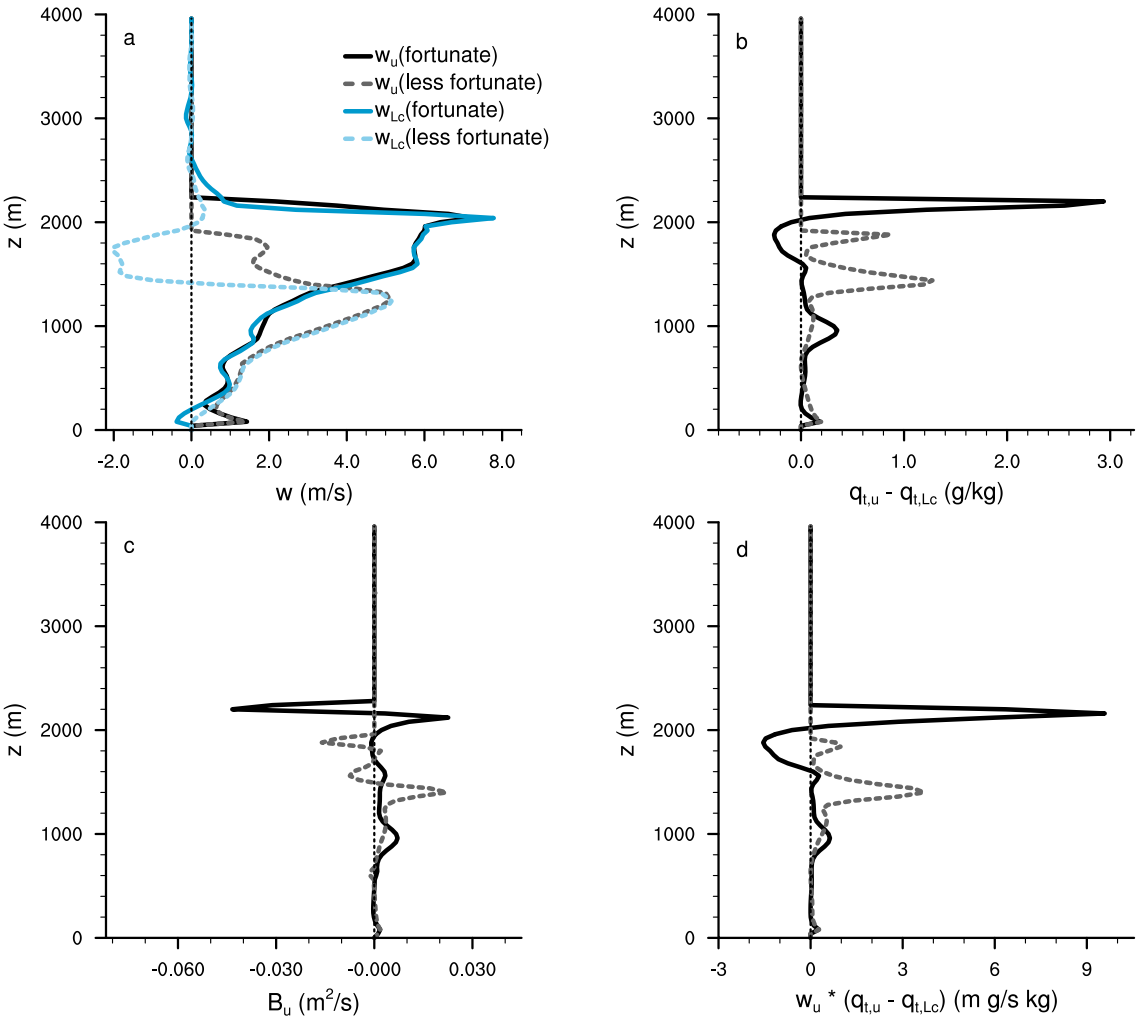

Figure 3.10: Profiles of (a) vertical velocity, (b) q_t-excess, (c) buoyancy, and (d) $w'q_t'$ for the fortunate (solid line) and the less fortunate parcel (dashed line) and the LES columns (blue).

still be associated with a positive value with respect to the horizontal mean). Near the termination height this term peaks due to the combined high values of vertical velocity and q_t-excess at that height.

The results illustrate that the parcel reacts immediately to changes in its environment. As long as the vertical velocity inside the LES cloud is positive, the parcel follows with a similar vertical velocity; the picture emerges that it is sailing along with the cloud, profiting from its protected status. Once the parcel shoots out of the cloud, it quickly reaches its termination height. The vertical extent of this overshooting layer is small, suggesting that parcels cannot live long outside an LES cloud.

A Less Fortunate Parcel

Another parcel is studied as an opposite example. This parcel, taken from the second highest category of section 3.4.2, does not reach that high, and could therefore be labeled as a "less fortunate" parcel. It is a less extreme case than the "fortunate parcel" and serves as an example of the variety of parcels' fates. Figures 3.10 shows the profiles of this less fortunate parcel. The q_t-excess differs substantially from the fortunate parcel in its second peak between 1200 m and 1600 m, which corresponds to a decrease in its vertical velocity w_u. Somewhat counterintuitively, its buoyancy B_u at this height is mostly positive and much larger than the buoyancy of the fortunate parcel. The profile of $w'q_t'$ resembles the profile of the q_t-excess. Figure 3.9 (b) shows the LES environment in which the less fortunate parcel rises. It contains two clouds, and although the parcel rises at the edge of the higher cloud, this still results in a double peak in the liquid water mixing ratio at about 1400 m and 1800 m. Because between those two peaks, $q_{t,Lc}$ is at a minimum, $q_{t,u}$ is now larger than $q_{t,Lc}$, associated with a peak in the q_t-excess. This behavior, featuring a gap in the LES cloud, can in this framework be loosely interpreted as a particle being detrained by one cloud and subsequently being entrained by another.

The parcel behavior for this less fortunate parcel further highlights how strongly the parcel reacts to its direct environment. Only when it leaves a cloud is it actively able to do transport relative to its direct environment; however, the hostile air then quickly and efficiently reduces both its kinetic energy and excess properties.

3.4.4 Budget Analyses

Fortunate Parcel

The behavior of the rising parcels can be revealed in more detail by studying the different terms of the budgets that control the behavior of the parcels. Two terms in the parcel's kinetic energy budget can have opposing effects, the mixing term and the buoyancy B_u (eq. (3.3)). Figure 3.11 (a) shows the variables making up the buoyancy B_u for the fortunate parcel, including the virtual potential temperature of this parcel $\Theta_{v,u}$, the LES column $\Theta_{v,Lc}$, and the average over the whole domain $\overline{\Theta_v}$. B_u and $B_{Lc} = g(\Theta_{v,Lc} - \overline{\Theta_v})/\overline{\Theta_v}$, are also shown for reference. The $\overline{\Theta_v}$ profile shows the well mixed subcloud layer with a more or less constant value, a conditionally unstable lapse rate in the cloud layer and an inversion at about 1900 m. In the cloud layer $\Theta_{v,Lc} > \overline{\Theta_v}$, which is in accordance with the rising of the convective cloud in the column. Near the top of the cloud $\Theta_{v,Lc}$ is smaller than $\overline{\Theta_v}$. Compared to $\Theta_{v,Lc}$, $\Theta_{v,u}$ is only marginally larger, but extends slightly higher. B_{Lc} is positive up to the height where $\Theta_{v,Lc}$ gets lower than $\overline{\Theta_v}$. Here, B_{Lc} becomes negative

up to the cloud top. In contrast, the updraft buoyancy B_u is only marginally positive. At the height where the LES cloud reaches its top, B_u has a positive peak, until $\Theta_{v,u}$ sharply decreases as the particle overshoots the cloud. These profiles show that the parcel model feels its local environment and reacts to it; it sails with the LES cloud in a weakly buoyant state.

The analysis of the kinetic energy budget (eq. (3.2)), including the buoyancy term, the acceleration term, and the mixing term, is shown in Figure 3.11 (c). Between cloud base and about 1800 m, the buoyancy and the mixing term are relatively small, and the acceleration mostly follows the mixing term. Above 1800 m, the mixing term dominates the budget up to shortly beneath cloud top. Note that the profile of the mixing term depends on $(w_u - w_{Lc})$ (see eq. (3.2)). Between 1000 m and 2000 m the term $w_u^2 - w_{Lc}^2 < 0$ (see Fig. 3.10), causing the mixing term to become positive. The opposite is true between 2000 m and the termination height, resulting in a negative mixing term. At cloud top B_u takes over with a negative peak, while the mixing is already zero. Apparently, when the parcel shoots out of the cloud, its local buoyancy B_u becomes positive but is outdone by the suddenly strongly negative mixing term, causing the parcel to dilute and quickly loose its buoyancy. In other words, mixing is more important than buoyancy in the kinetic energy budget.

Less Fortunate Parcel

The budget analysis for the less fortunate parcel is shown in Figure 3.11 (b) and (d). Compared to Figure 3.11 (a), Figure 3.11 (b) shows that $\Theta_{v,Lc}$ becomes smaller than $\overline{\Theta_v}$ at a lower height. There is an area around 1400 m where $\Theta_{v,u}$ is much larger than $\Theta_{v,Lc}$. In this area, B_{Lc} has a minimum, while B_u peaks. This area corresponds to the gap in the cloud (Fig. 3.9 (b)).

For the kinetic energy budget (eq. (3.2), Fig. 3.11 (d)), in the lower part of the cloud layer, the mixing term is positive while the buoyancy is small, resulting in a slightly positive acceleration term which enables the parcel to rise with the background LES cloud. Above about 1200 m, the mixing term becomes negative because $w_u - w_{Lc} > 0$ (see Fig. 3.10). This mixing slows the parcel, causing the vertical velocity to decrease, because the mixing term has a higher magnitude than the suddenly positive buoyancy B_u. As the parcel enters the second LES cloud, it keeps decelerating, mainly because w_{Lc} is mostly negative (a passive cloud). As it overshoots the second cloud, negative buoyancy B_u efficiently slows the parcel down to a standstill.

At this point the following picture emerges about how parcels interact with a heterogeneous environment. Inside an LES cloud the local parcel buoyancy B_u is small, while its

properties are close to that of the background; as a result, it is able to move with the cloud, being screened off from the hostile environment. As soon as it leaves the cloud, however, the mixing term starts to dominate the kinetic energy budget and ensures that the parcel quickly looses its excess properties, in the process becoming more important than the buoyancy. This mechanism effectively sorts out the parcels outside of clouds from the ones inside clouds. Given the dominance of the mixing term, this process could be referred to as a "mixing-sorting mechanism".

It is interesting to draw parallels with the buoyancy sorting mechanism as proposed by KAIN AND FRITSCH [1990]. The main difference is that the buoyancy sorting mechanism is formulated in terms of the total buoyancy of a parcel over the mean state, $B_{Lc} + B_u$, while the mixing-sorting mechanism as described above is formulated in terms of the local B_u alone. In principle, they describe the same process, of parcels decelerating when leaving a cloud. However, as we find that the mixing term is in the end responsible for slowing down (and sorting out) the parcel, and not the buoyancy term, one could argue that mixing-sorting is a more appropriate name for this process.

3.5 Summary and Conclusions

In this study the potential impact of the local environment on the fate of a rising parcel is investigated. To this purpose a simplified setup was used, with parcels interacting with profiles that reflect the heterogeneous turbulent environment that they may encounter during their ascent. This way, interaction with other parcels is indirectly represented, which is a novelty in multiparcel modeling. In addition, the method is designed to enable the investigation of well-known mechanisms like parcel screening and buoyancy sorting. Different entrainment models were used in the same setup to investigate the effect of the entrainment parameterization on parcel behavior. An LES was used to generate a shallow cumulus cloud field, providing the range of different local environments that is required for this study.

We find that the most important factor determining the eventual parcel termination height is the local environment that it encounters on its way; the formulation of the entrainment model is of secondary importance. The entrainment model depending on the background buoyancy performs best. We speculate that the information of the state of the environment captured by the background buoyancy can explain this. The results further suggest that i) parcel screening is efficient in boosting their termination height, ii) parcels quickly loose their excess properties when leaving a protective in-cloud area, iii) mixing dominates over local buoyancy in the kinetic energy budget of these parcels, and iv) initial conditions seem to be less important than the mixing.

Despite the simplicity of our method, for example in the use of vertically sampled LES profiles to act as parcel environments and the omission of life cycle effects, the method is already successful in providing insight into some important mechanisms in shallow cumulus convection. This includes the parcel screening effect, the buoyancy sorting mechanism, and the importance of the local environment over the entrainment formulation. It would be interesting to explore if profiles obtained from LES trajectory analyses would yield the same results. This is considered a future research topic.

This study makes use of entrainment models that have been proposed in the literature. It is beyond the scope of this study to validate these models, or to derive new ones. The sole aim of including many different dependencies is to find out if any of these entrainment models can diminish the apparently dominant role of the local environment in determining parcel termination height. It is clear from the results that none can do so.

What do the results and insights obtained in this study imply for the parameterization of shallow cumulus convection? Perhaps the most important consequence is that the local environment encountered by rising parcels should be taken into account in the associated budget equations. This can be achieved either indirectly, by perhaps using a stochastic entrainment closure to mimic a chance encounter with heterogeneous air, or directly, by letting rising parcels in an ensemble somehow interact with each other. The development of such models is considered a future research opportunity. Perhaps the results obtained in this study can provide some guidance in this effort.

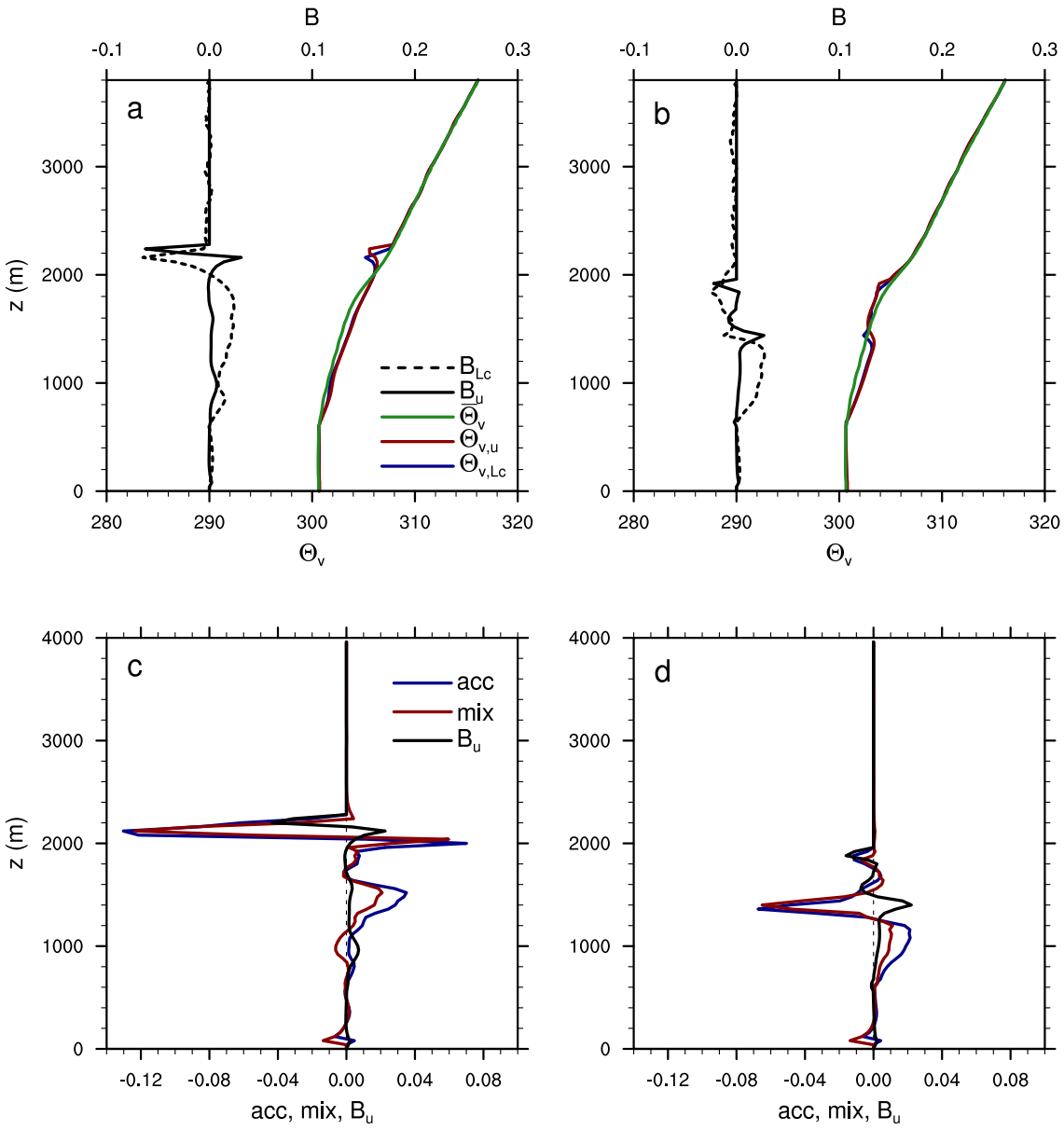

Figure 3.11: Buoyancy and contributing terms (eq. (3.3)) for (a) the fortunate parcel and (b) the less fortunate parcel, and the budget analysis for the kinetic energy (eq. (3.2)) for (c) the fortunate parcel and (d) the less fortunate parcel.

4 Testing the scale-adaptivity of a shallow cumulus parameterization scheme

Abstract

In this study we investigate the scale-adaptivity of a new parameterization scheme for shallow cumulus clouds in the gray zone. The Eddy Diffusivity Multiple Mass Flux (or ED(MF)^n) scheme is a bin-macrophysics scheme, in which subgrid transport is formulated in terms of discretized size densities. While scale-adaptivity in the ED-component is achieved using a pragmatic blending approach, the MF-component is filtered such that only the transport by plumes smaller than the grid size is maintained. For testing, ED(MF)^n is implemented into a large-eddy simulation (LES) model, replacing the original subgrid scheme for turbulent transport. LES thus plays the role of a non-hydrostatic testing ground, which can be run at different resolutions to study the behavior of the parameterization scheme in the boundary-layer gray zone. In this range convective cumulus clouds are partially resolved. We find that at high resolutions the clouds and the turbulent transport are predominantly resolved by the LES, and the transport represented by ED(MF)^n is small. This partitioning changes towards coarser resolutions, with the representation of shallow cumulus clouds becoming exclusively carried by the ED(MF)^n. The way the partitioning changes with grid-spacing matches the results of previous LES studies, suggesting some scale-adaptivity is captured. Sensitivity studies show that a scale-inadaptive ED component stays too active at high resolutions, and that the results are fairly insensitive to the number of transporting updrafts in the ED(MF)^n scheme. Other assumptions in the scheme, such as the distribution of updrafts across sizes and the value of the area fraction covered by updrafts, are found to affect the location of the gray zone.

4.1 Introduction

Clouds play an important role in the Earth's climate system. While global models resolve the large-scale clouds, the smaller scale clouds require parameterization. This includes shallow cumulus clouds, covering large areas over the oceans in the subtropical trade

wind regions. The vertical transport of heat and water vapor associated with shallow cumulus clouds is a key part of the Hadley circulation, and thus significantly affects large-scale circulation [e. g., TIEDTKE, 1989; NEGGERS ET AL., 2007]. The importance of a good representation of this type of clouds in large-scale models has long been recognized [TIEDTKE, 1989; VIAL ET AL., 2013], and a variety of parameterizations have been developed [an overview of cumulus parameterizations is given in ARAKAWA, 2004]. Limits in computational power still constrain the complexity of such parameterizations, so that in practice a compromise must be found between a realistic representation of the clouds and computational costs.

First generation cumulus schemes are often based on the bulk mass flux approach [e. g., OOYAMA, 1971; BETTS, 1973; YANAI ET AL., 1973; ARAKAWA AND SCHUBERT, 1974; FRITSCH AND CHAPPELL, 1980; TIEDTKE, 1989]. In this approach the vertical transport of heat and moisture by an ensemble of rising plumes is parameterized through one single plume representing the whole ensemble [SIMPSON AND WIGGERT, 1969]. Mass flux schemes are popular because they are not only relatively simple and computationally cheap, but they also capture key aspects of cumulus convection, such as the advective nature of related transport. A mass flux parameterization can represent most of the turbulent convective transport in the cloud layer [SIEBESMA AND CUIJPERS, 1995; SIEBESMA ET AL., 2003] as well as the coupling with the subcloud layer [GRANT, 2001].

The development and further improvement of mass flux schemes is still ongoing, with the rising plume model [SIMPSON AND WIGGERT, 1969] still at the foundation of most of these frameworks. When the grid resolutions of atmospheric models increase such that boundary layer processes become partially resolved (a situation referred to as the "terra incognita" or "gray zone" of convection [WYNGAARD, 2004]) the parameterization scheme should become scale-aware and scale-adaptive. This means that the scheme realizes which processes are resolved and which must be parameterized (scale-awareness) and that it responds by only parameterizing those processes that cannot be resolved (scale-adaptivity). Scale-awareness and adaptivity can be introduced by using not a single but multiple plumes, each representing different characteristics. The idea of parameterizing shallow cumulus convection by taking into account clouds of different sizes is not new. One of the first to use this idea are ARAKAWA AND SCHUBERT [1974], who divide an ensemble of shallow cumulus clouds into sub-ensembles and thereby account for the different cloud sizes. This scheme is the basis for the multiparcel scheme by WAGNER AND GRAF [2010], who use a different closure formulation than ARAKAWA AND SCHUBERT [1974]. NEGGERS ET AL. [2002] describe a multiparcel model with the focus on the lateral entrainment rate, which depends on the vertical velocity of the rising parcels. PARK [2014a] uses multiple updrafts and downdrafts to unify deep and shallow convection. Other schemes use ensembles of clouds within a stochastic approach [e. g., OOYAMA, 1971; PLANT AND CRAIG,

2008; SAKRADZIJA ET AL., 2015]. Some recent studies are specifically designed to introduce the ability to adapt to different resolutions [TEIXEIRA ET AL., 2008; BOGENSCHUTZ AND KRUEGER, 2013; BOUTLE ET AL., 2014], but further research about scale-adaptive parameterizations is still needed.

The use of size densities in shallow cumulus parameterization has various advantages. Bulk mass flux approaches describe the characteristics of one single cloud which represents the whole ensemble of cumulus clouds. However, shallow cumulus clouds vary greatly in size and therefore have different characteristics [e. g., DAWE AND AUSTIN, 2012; BÖING ET AL., 2012], so that combining the characteristics of all individual clouds into one bulk scheme fails to realistically describe the variation among the clouds. A scheme using size densities can take the characteristics of different cloud sizes into account, as well as representing the distribution of cloud sizes, which is important because in a shallow cumulus field, many small clouds exist with few large clouds [e. g., PLANK, 1969]. Another advantage of using size densities is that in principal, the different cloud sizes can interact with each other indirectly through the environment in which they rise, i. e., through the mean state of the columns in the large scale model (in chapter 3 it was shown that rising parcels are affected by their environment. Thus, if a parameterization scheme affects the environment as well, interaction between plumes is given). Finally, with size densities it is easy to introduce scale-awareness of the parameterization, by only taking into account the desired cloud sizes.

This study is based on a multiplume model described in NEGGERS [2015], called ED(MF)^n, which is described in detail in section 4.2.1. In NEGGERS [2015], ED(MF)^n was implemented into a single column model (SCM) and compared to a large-eddy simulation (LES), which is a common method to develop and test parameterization schemes. The properties of different cloud size bins were investigated and it was hypothesized that this parameterization scheme could be scale-adaptive. LES models are mostly used to resolve large-scale eddies, while the small-scale eddies are parameterized. Thus, most of the energy is resolved by the model, because the large eddies carry most of the energy. Therefore, shallow cumulus clouds are for the largest part resolved. The small eddies are parameterized by a subgrid scheme, which in our case is a Smagorinsky-Lilly-type scheme. LES has proven to be successful at simulating moist convective boundary layers and clouds [SIEBESMA ET AL., 2003; HEUS ET AL., 2010; VANZANTEN ET AL., 2011].

In this study, the scale-adaptivity of ED(MF)^n is tested in a novel way. To test scale-adaptivity, a scheme can be implemented into a larger-scale model which is then run with varying resolutions, covering the gray zone. To avoid the results being clouded by the complexity of operational weather forecast models, such as other parameterization schemes, in this study an LES model is used with which to test ED(MF)^n. Due to its simplicity, its design allows to study the effect of the parameterization scheme directly. The new approach

in this study is to replace the original subgrid scheme with the parameterization scheme ED(MF)^n, so that multiple plumes are launched inside each column of the LES. The LES is then run with resolutions varying from hundreds to thousand meters. Of course, if an LES is run with a resolution of 1 km, most eddies carrying energy are not resolved anymore, so we do not use LES in a conventional way. Instead, we use it as an idealized large-scale model, in which the turbulence is parameterized by the eddy diffusivity part of ED(MF)^n, and most transport is done by the rising plumes of ED(MF)^n. If the scheme is truly scale-adaptive, with a very fine resolution the LES will work as it was designed to work, with most of the energy and transport resolved by the LES, and only a very small portion of the energy will be parameterized by the subgrid scheme, which in our case is ED(MF)^n instead of the usual Smagorinsky-Lilly-type scheme. However, with coarser resolutions, the LES will not be able to resolve most of the turbulence, so that the subgrid scheme, i. e., the ED(MF)^n, will do more transport of energy. Thus, LES is used as a testing-ground for scale-aware and scale-adaptive modeling. By launching multiple plumes in each column, the LES acts as a simplified larger scale model with varying resolutions, profiting from its non-hydrostatic formulation and high model transparency. The goal of this study is thus to investigate how the plume model responds to resolved clouds present in an LES domain for different resolutions of the LES.

In section 4.2 the method of testing scale-adaptivity and a more detailed description of the setup is described. The results are presented in section 4.3, and a discussion and summary of the findings are given in section 4.4.

4.2 Method

4.2.1 Formulation of ED(MF)^n

The ED(MF)^n framework used in this study is based on the EDMF framework introduced by SIEBESMA ET AL. [2007]. EDMF parameterizes the transport in the boundary layer by combining two previously used approaches. The eddy diffusivity part, ED, describes a turbulent field. In this approach, the turbulent flux $\overline{w'\Phi'}$ is parameterized by multiplying the local gradient of Φ with a coefficient K. This approach alone is not able to describe sufficiently the upwards vertical transport in a convective boundary layer. The mass flux part, MF, describes the transport done by updrafts. Here, the flux is parameterized by the difference between the Φ of the updraft and the horizontal mean, multiplied by a mass flux M. The mass flux approach is suitable to represent convective clouds, so the combination of both parts can be used to describe clear boundary layers as well as boundary layers with

convective clouds:

$$\overline{w'\Phi'} = -K\frac{\partial\overline{\Phi}}{\partial z} + M(\Phi - \overline{\Phi}) \tag{4.1}$$

with Φ a conserved thermodynamic variable (liquid water potential temperature Θ_l or total water mixing ratio q_t).

The original framework of EDMF uses one updraft in each grid box. To use the advantages brought by multiplumes, NEGGERS [2015] developed a new scheme, ED(MF)^n, which uses bin-macrophysics and introduces size filtering. It is based on EDMF, but instead of one updraft, n different updrafts enable the model to represent discretized cloud size densities, given by

$$N(z) = \int_l \mathscr{N}(l,z)dl \tag{4.2}$$

with N the total number of plumes at each height z and $\mathscr{N}$ the number density representing the number of plumes for each size bin l. The corresponding area size the plumes cover is given by

$$a(z) = \int_l \mathscr{A}(l,z)dl \tag{4.3}$$

with $\mathscr{A}$ the area covered by the plumes in one bin and a the total area covered by plumes. The mass flux M of the plumes is also dependent on their size:

$$\mathscr{M}(l,z) = \mathscr{A}(l,z)[w_u(l,z) - w_e(z)] \tag{4.4}$$

with w_e the vertical velocity of the environment and subscript u denoting updrafts. In large-scale-models, w_e is negligible (e.g. SIEBESMA ET AL. [2007]) but for the small resolutions of LES used in this study (see sec. 4.2.3) w_e must be considered [HONNERT ET AL., 2016]. Since the vertical velocity of the environment in our case is the resolved vertical velocity of the LES, w_e becomes w_{LES}. Correspondingly, Φ_e becomes Φ_{LES}.

The resulting parameterization offers the adjustment to different resolutions by only integrating over those plumes which are too small to be resolved. Therefore, the turbulent flux in ED(MF)^n is parameterized by

$$\overline{w'\Phi'} = -K\frac{\partial\overline{\Phi}}{\partial z} + \int_l^F \mathscr{A}(l,z)[w(l,z) - w_{LES}(z)](\Phi_u - \Phi_{LES})dl \tag{4.5}$$

with F the filter size. The first term on the right hand side represents the eddy diffusivity, the second term stands for the mass flux. To close this equation, the eddy diffusivity coefficient K and the behavior of the updrafts must be described. For the thermals, a plume model is used, based on SIMPSON AND WIGGERT [1969], also used in the original EDMF by SIEBESMA ET AL. [2007] and described in detail in chapter 3 of this thesis. The parameter K in the mixed layer is

$$\begin{aligned} K_h &= \frac{\kappa u_*}{\Phi_{h0}} \left(1 - \frac{z}{z_i}\right)^2 \\ K_m &= \frac{\kappa u_*}{\Phi_{m0}} \left(1 - \frac{z}{z_i}\right)^2 \end{aligned} \tag{4.6}$$

with subscripts h and m standing for heat and momentum, κ the Von Kármán's constant, u_* the friction velocity, z the height, z_i the boundary layer height, and Φ_{h0} and Φ_{m0} stability functions

$$\begin{aligned} \Phi_{h0} &= \left(1 - 39\frac{z}{L}\right)^{-1/3} \\ \Phi_{m0} &= \left(1 - 15\frac{z}{L}\right)^{-1/3} \end{aligned} \tag{4.7}$$

with L the Obukhov length. In the cloud layer

$$\begin{aligned} K_h &= \frac{l^2}{\Phi_m \Phi_h} \left|\frac{\partial u}{\partial z}\right| \\ K_m &= \frac{l^2}{\Phi_m^2} \cdot \left|\frac{\partial u}{\partial z}\right| \end{aligned} \tag{4.8}$$

with the length $l = 150m$, and Φ_m and Φ_h gradient functions. For more details see EUROPEAN CENTRE FOR MEDIUM-RANGE WEATHER FORECASTS [2014]. Assumptions for the cloud size density $\mathscr{N}$, the area size a and the entrainment of the plumes, needed for the plume model, are given in section 4.2.3. For more details on the formulation of ED(MF)^n see NEGGERS [2015].

Figure 4.1 shows the concept of this approach. The upper part shows a number of plumes of the parameterization scheme, each representing updrafts of a certain size. Some of the plumes in the parameterization scheme reach the lifting condensation level and thus represent clouds. In the lower part, the corresponding number of clouds are shown, which

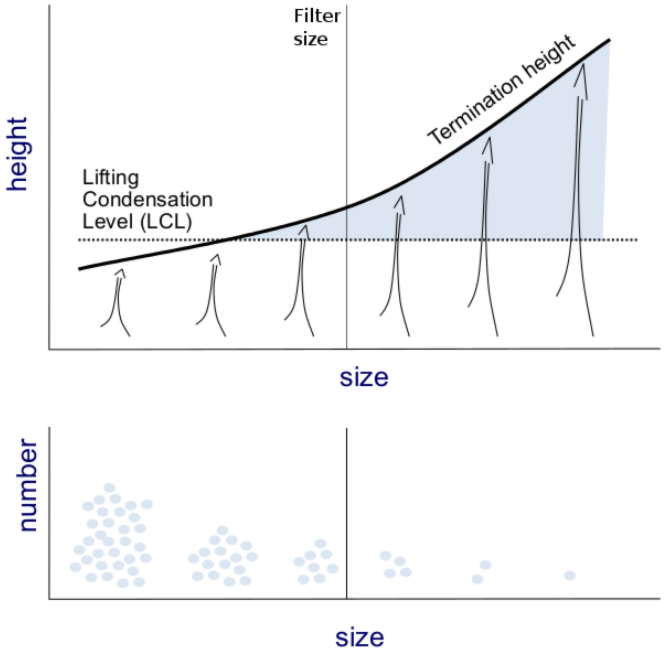

Figure 4.1: Illustration of the concept of ED(MF)^n. Upper part: an ensemble of plumes with the lifting condensation level, termination height, and in blue the area where the plumes condense. Lower part: the number of updrafts each plume in the upper part represents. Figure adapted from NEGGERS [2015].

each plume in the parameterization represents. Here, many small clouds are represented by the small updrafts of the parameterization, while only few clouds are represented by the large updrafts. This corresponds to the observed size distribution of shallow cumulus clouds fields [e. g., PLANK, 1969]. The upper part also shows the lifting condensation level (LCL) of the updrafts, so only the larger updrafts condensate, while the termination height of the smaller updrafts can be lower than the LCL. Also shown is the filter size. When implemented into a large-scale model, this model is run with a certain resolution, which determines the size of updrafts that can be resolved. The filter size of ED(MF)^n can now be chosen to include only those updrafts that are not resolved by the large-scale model, thus making the scheme scale-aware.

4.2.2 Eddy Diffusivity

NEGGERS [2015] describe that the MF part of EDMF can be made scale-aware by including not one but n updrafts. However, the eddy diffusivity part of the parameterization scheme is not taken into account. This results in a contribution of ED(MF)^n to the vertical transport for simulations with a fine grid resolution that is slightly too high (see section 4.3.3). The main goal of this study is to investigate the scale-adaptivity achieved by introducing scale-awareness to the mass flux. However, the impact of a scale-aware eddy diffusivity is

also investigated. This scale-awareness is introduced by adjusting the coefficient K_h in formulation (4.5). In this study, K_h is now made scale-aware for the subcloud and cloud layer separately. In our method, K_h from the LES, calculated with a Smagorinsky-Lilly-type scheme, is used. Though we replace the original subgrid scale (SGS) scheme of the LES, it is still calculated during the simulations in parallel to ED(MF)^n, so that parts of it, namely K_h, can be used to make the ED-part of ED(MF)^n scale-aware.

For the cloud layer, the coefficient K_h from the LES, calculated with a Smagorinsky-Lilly-type scheme, is compared to the K_h calculated in ED(MF)^n. The smaller value is then taken as the K_h for the scale-aware ED in the cloud layer. This has the desired effect that K_h stays small in the cloud layer, since the eddy diffusivity is playing a small role because the transport by clouds is associated with rising updrafts. For the subcloud layer, another approach is taken, since here, close to the surface, the eddy diffusivity plays a slightly different role. Therefore, the pragmatic blending approach by BOUTLE ET AL. [2014] is used, where K_h is modified by a weighing function. Thereby, for small resolutions, K_h resembles the K_h calculated by the Smagorinsky-type scheme of the LES, while for coarse resolutions, K_h resembles the K_h calculated by ED(MF)^n:

$$K_h = W K_{h,EDMF} + (1-W) K_{h,LES} \tag{4.9}$$

with W the weighing function based on turbulent kinetic energy partitioning by HONNERT ET AL. [2011] and simplified by BOUTLE ET AL. [2014]:

$$W = 1 - \tanh\left(\frac{\beta z_i}{\Delta x}\right) \max\left(0, 1 - \frac{\Delta x}{4 z_i}\right) \tag{4.10}$$

with $\beta = 0.15$ a parameter controlling the speed of the transition, z_i the boundary layer height, and Δx the horizontal grid size. K_h of the LES is calculated as

$$K_h = \frac{K_m}{Pr} \tag{4.11}$$

with Pr the Prandtl-number and K_m the coefficient for momentum:

$$K_m = (c_s l)^2 S \sqrt{1 - \frac{Ri}{Pr}} \tag{4.12}$$

with c_s a constant, l a length scale, S the magnitude of deformation, and Ri the local Richardson number. For more information about the Smagorinsky-Lilly turbulence scheme see, e. g., STEVENS ET AL. [1999].

Using equation (4.9) results for the simulation with a horizontal resolution of 100 m in a

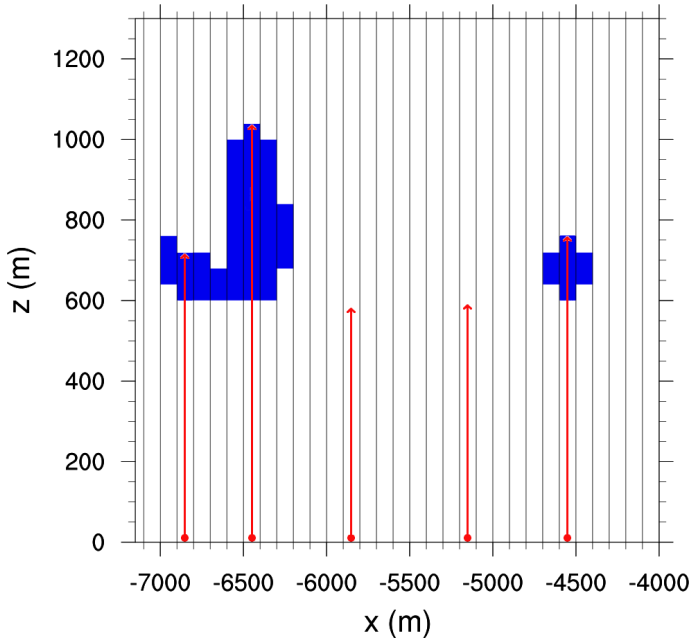

Figure 4.2: Schematic description of the implementation of the plume model into the LES. The blue area denotes the LES cloud. The arrows are illustrative for the plumes rising in every column. The arrowhead is the suggestive termination height.

K_h consisting of about 96 % of the K_h from the LES, while for a resolution of 1000 m, K_h consists of about 95 % of the K_h from ED(MF)^n. By using the K_h from LES and therefore including the grid size Δx, both parts of ED(MF)^n are scale-aware. The effect of this added change to ED(MF)^n is presented in section 4.3.3.

4.2.3 Setup

The parameterization scheme ED(MF)^n is now implemented into an LES. The LES used in this study is the UCLALES, described in STEVENS ET AL. [2005]. ED(MF)^n is included into LES by replacing the SGS scheme of the LES, so that the information about subgrid-scale transport is coming from ED(MF)^n instead of the Smagorinsky-based SGS scheme of the LES. In each column of the LES, the ED(MF)^n initializes a number n of updrafts, which continue to rise until they reach their termination height. Also, the eddy diffusivity is calculated for each column (the ED part of ED(MF)^n). This implementation is depicted in Figure 4.2. Here, for some random columns some updrafts are shown in red. They rise until reaching their termination height, which is dependent on the environment they rise in (see chapter 3). In this Figure, for simplicity the number n of updrafts is 1. For most simulations in this study, a maximum of $n = 10$ updrafts will be used, which should be a good compromise between resolving the size density while minimizing computational costs. A sensitivity study of this value is given in section 4.3.3.

To use the mass flux parameterization presented in section 4.2.1 some assumptions must be made. The entrainment rate ε of the plumes is inversely depending on plume size and the size density $N(z)$ is prescribed by a power law with no scale break. For each run, only those updrafts are taken into account which are smaller than the filter size F in equation (4.5), which is here taken to be equal to the grid size. This is a simplification, since more than one grid box is needed to fully resolve a convective process. The total area fraction covered by all plumes, a, is set to a constant of 10 %. Further development of ED(MF)^n should consider a variable total updraft fraction to fully understand the implications of this simplification, but this further complexity is outside of the scope of this study. The effect of a different constant for a is studied in section 4.3.3. Further simplifications include that the updrafts can only rise vertically and horizontal displacement due to, e. g., the mean wind, are not taken into account. Also, when the updrafts are calculated, they are given the instantaneous profiles of the LES columns in which the updrafts rise. This does not take into account the cloud life cycles. However, with this setup it is possible to study the scale-adaptivity of the parameterization scheme, which is designed to be a compromise between realistic behavior and complexity. Therefore, the current setup is suitable for this study; further improvements of these assumptions is considered a future research topic.

To study the scale-adaptivity of the parameterization scheme, ten simulations were run with resolutions ranging from 100 m to 1 km, with a vertical resolution for all runs of 40 m. LES was not originally designed for these coarse resolutions. However, though for the coarse resolutions the fraction of energy represented by the subgrid scheme is not small anymore, ED(MF)^n is designed to conduct the transport not resolved by the larger-scale model, and therefore this setup is well suited to the current study. The domains have $144 \times 144 \times 100$ grid boxes, which results in a different domain size for each simulation. This difference in domain size might slightly affect the representation of the flow, but we think that this effect is negligible. The advantage of this setup is that we always have the same number of columns, which aids to compare the statistics of the simulations. The ten updrafts have sizes equally distributed between 50 m to 950 m. As a test case, the Rain In shallow Cumulus over the Ocean (RICO) case is chosen [VANZANTEN ET AL., 2011], which is a well documented case of shallow convection. The LES model used in this study, UCLALES, has participated in an intercomparison and proven to be suitable to simulate this case [RAUBER ET AL., 2007]. The simulation time was 9 h, where the last three hours are used for analysis. Every timestep, the subgrid scheme ED(MF)^n is called.

4.3 Results

For different resolutions, the ability of the LES to resolve shallow cumulus clouds varies. This is illustrated in Figure 4.3, where a schematic shows that one exemplary cloud can

be resolved for fine resolutions, while it is a subgrid-scale process for coarser resolutions. This effect is shown for simulations with varying resolutions in Figure 4.4. Here, the resolved liquid water mixing ratio of simulations with different resolutions represents the clouds resolved in the simulations. For the simulation with a fine resolution of 100 m, many clouds can be resolved, while for the coarse resolution of 1 km much less clouds can be resolved. In our case, no clouds are resolved for grid sizes of 700 m and more. The challenge of the subgrid scheme is now to represent all those clouds that are not resolved by the LES. The ability of the subgrid scheme to fulfill this task is studied in the following sections.

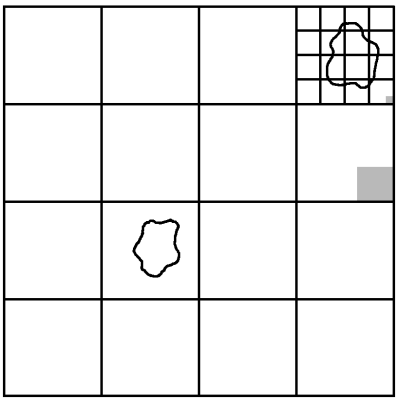

Figure 4.3: Schematic showing that small clouds are only resolved by fine grids. The two gray areas show the area fraction a of the updraft from eq. (4.3) for two different grid sizes.

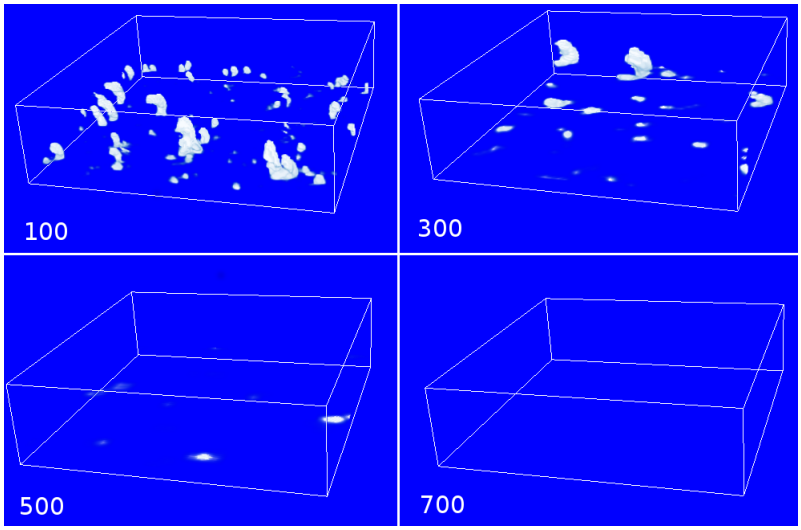

Figure 4.4: Contours of resolved liquid water mixing ratio for four different LES simulations with resolutions of 100, 300, 500, and 700 m after 12 h of simulated time.

4.3.1 Plume Behavior

Now the behavior of ED(MF)^n for the different resolutions is studied. Figure 4.5 shows profiles of different variables, divided into those parts represented by ED(MF)^n, those resolved by the LES, and those represented by both ED(MF)^n and LES, for different resolutions of the LES. The total transport is more or less the same for all resolutions, which is the behavior we expected. It has to be mentioned that the boundary layer doesn't develop in exactly the same way in all simulations, i. e., it shows some resolution dependency. For coarser resolutions, the boundary layer deepens more quickly, which could be due to the fact that the entrainment decreases with increasing plume size. Near the surface, the peaks of the fluxes differ slightly, probably because the resolutions near the ground for the coarse resolutions is not sufficient to resolve these peaks. The covariance of heat and moisture shows that for fine resolutions, the LES contributes most of the transport, while for coarse resolutions ED(MF)^n takes over.

The same behavior shown in Figure 4.5 is evident for some cloud variables (Fig.4.6). Here, another feature is obvious: for the simulation with a resolution of 1 km, discretized steps of the cloud variables appear. This feature is dependent on the number of rising plumes. Only the largest plumes represent the clouds, so when using 10 plumes only about two plumes represent most of the transport, and when one plume stops, a step in the cloud variable appears. The number of plumes are further studied in section 4.3.3.

These results indicate that ED(MF)^n is indeed scale-adaptive. The transport of heat and moisture is achieved almost exclusively by the LES for the fine resolutions, while for the coarse resolutions the subgrid scheme, which is in our case the ED(MF)^n parameterization scheme, takes over the transport.

Though for coarse resolutions there are no clouds present in the LES, a comparison was made between LES cloud top and termination height of the plumes. Figure 4.7 shows this comparison for the simulations with resolutions of 100 and 500 m. These resolutions were taken for illustration to have one resolution with most clouds resolved and one coarser resolution were the LES still resolves some clouds to allow the comparison of the terminations heights of the plumes with the LES clouds. The termination height of most plumes is close to the LES-cloud-tops for fine resolutions, because the plumes stop early and the clouds are resolved by the LES. With decreasing resolutions (Fig. 4.7b), the plume termination height increases compared to LES cloud top height. Here, less LES clouds are resolved and the plumes pick up the subgrid transport and therefore rise higher. This is a further indicator that the representation of the clouds gets shifted from the LES to the ED(MF)^n with decreasing resolution.

For all resolutions, the ratio between subgrid and resolved flux of q_t was calculated by

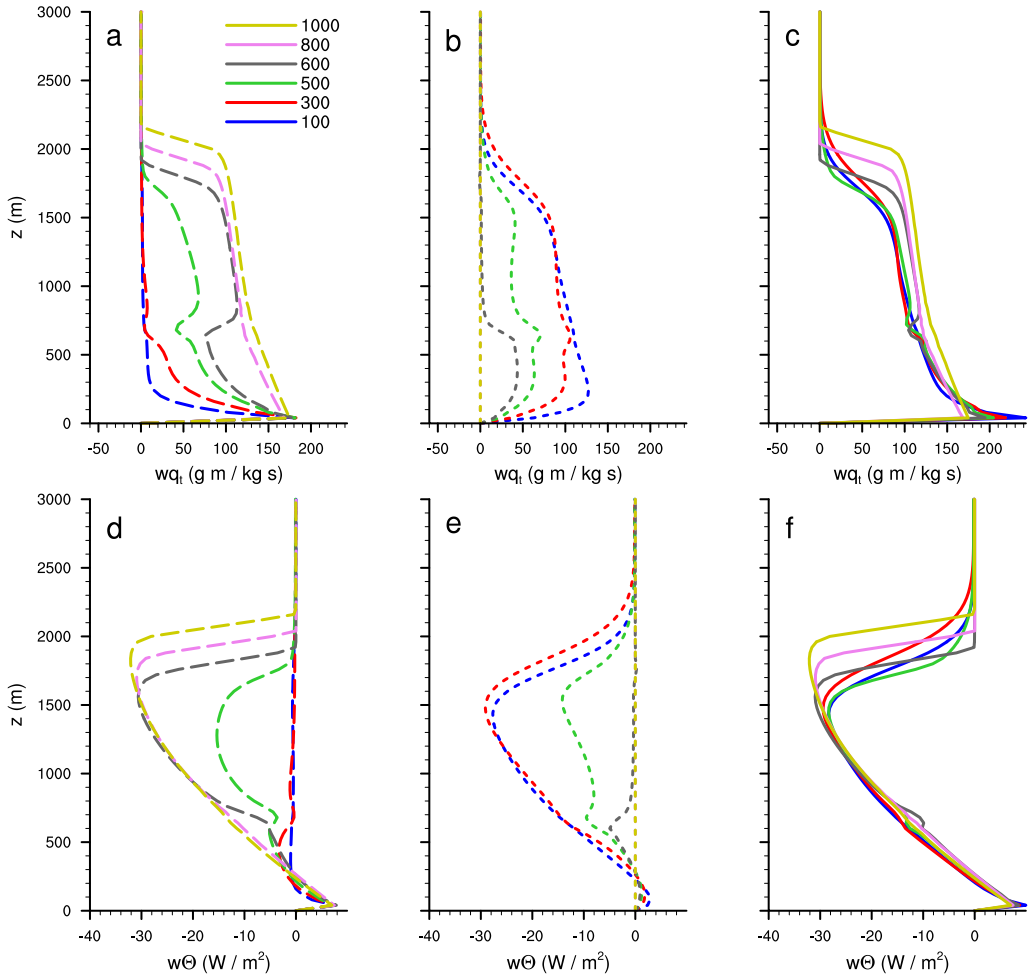

Figure 4.5: Profiles of vertical transport of q_t (a,b,c) and Θ (d,e,f), averaged horizontally and over three hours, for different resolutions (in colors). Dashed line: subgrid transport by ED(MF)^n, dotted line: resolved transport by LES, solid line: total transport.

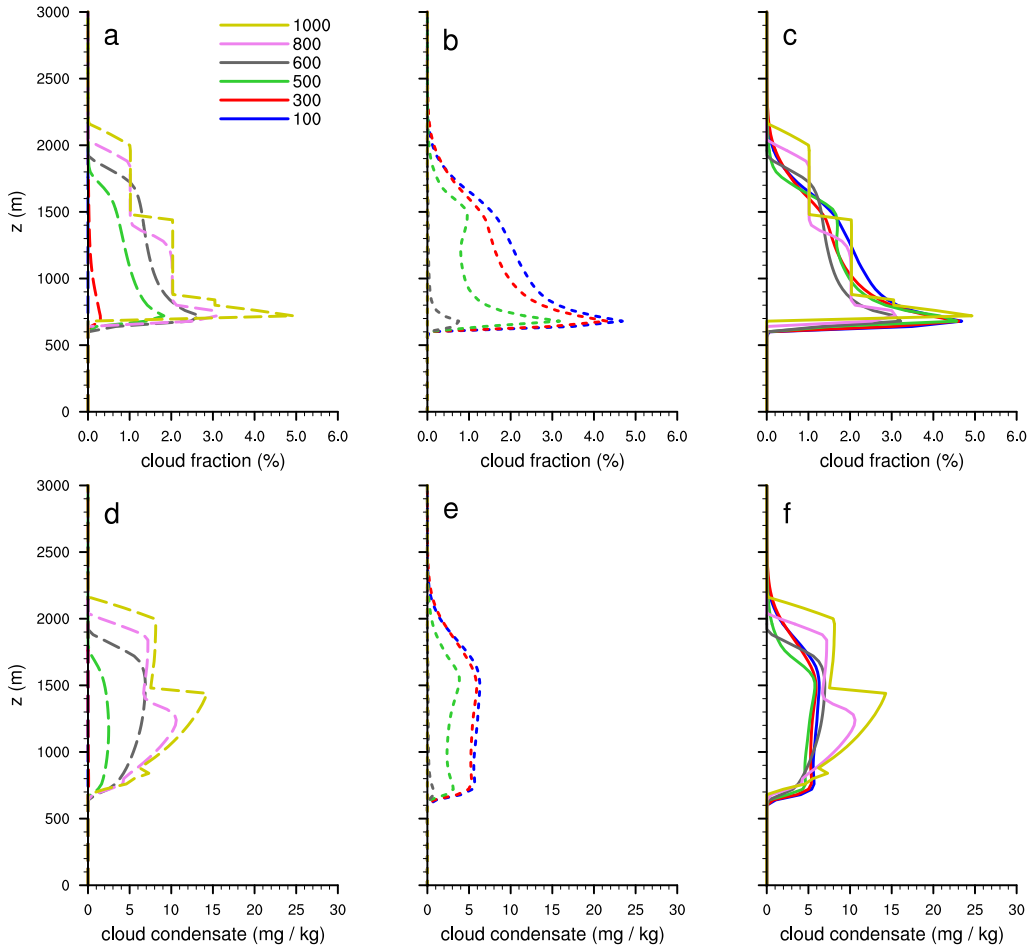

Figure 4.6: Profiles of (a,b,c) cloud fraction and (d,e,f) cloud condensate, averaged horizontally and over three hours, for different resolutions (in colors). Dashed line: subgrid portion by ED(MF)^n, dotted line: resolved portion by LES, solid line: total profile.

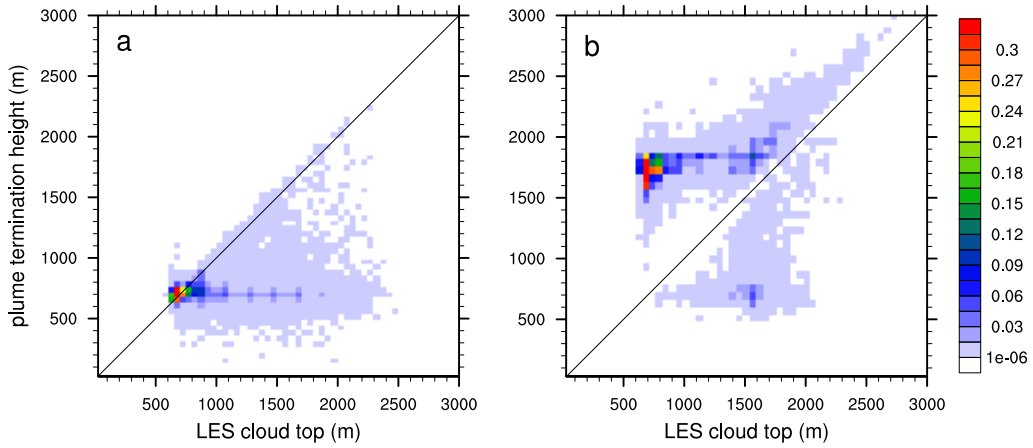

Figure 4.7: Frequency density function of LES cloud top and plume termination height averaged over three hours and a resolution of a) 100 m and b) 500 m.

averaging over the horizontal domain and over the heights between 400 and 2000 m (Fig. 4.8), resulting in an S-plot similar to Figure 2 in DORRESTIJN ET AL. [2013] and Figure 2 in HONNERT ET AL. [2016]. The Figure shows that for the coarse resolutions, all transport is done by the subgrid scheme ED(MF)^n, while for the resolutions of 400 m and finer resolutions more than 80 % of the flux is resolved. Also shown is the standard deviation of the subgrid flux. It exhibits a peak in the gray zone, representing the transition between clouds being mostly parameterized for coarse resolutions and clouds being mostly resolved for fine resolutions. The location and the magnitude of this peak are in accordance with those in DORRESTIJN ET AL. [2013]. For fine resolutions, there is an increase in the standard deviation, originating mainly from the middle of the cloud layer (not shown). Different choices of height averaging result in the same conclusion as long as the height interval roughly covers the cloud layer, which is shown in Figure 4.9. Here, the ratio is studied at certain heights corresponding to the mixed layer, the cloud layer, and above the cloud layer. It can be seen that the distribution between resolved and subgrid fluxes behaves scale-adaptively in the mixed layer (at 400 m) as well as in the cloud layer (at 1000 m), while for a height above the cloud layer (at 2400 m) the S-shape begins to falter, because the total transport becomes very small and only very few plumes reach this high.

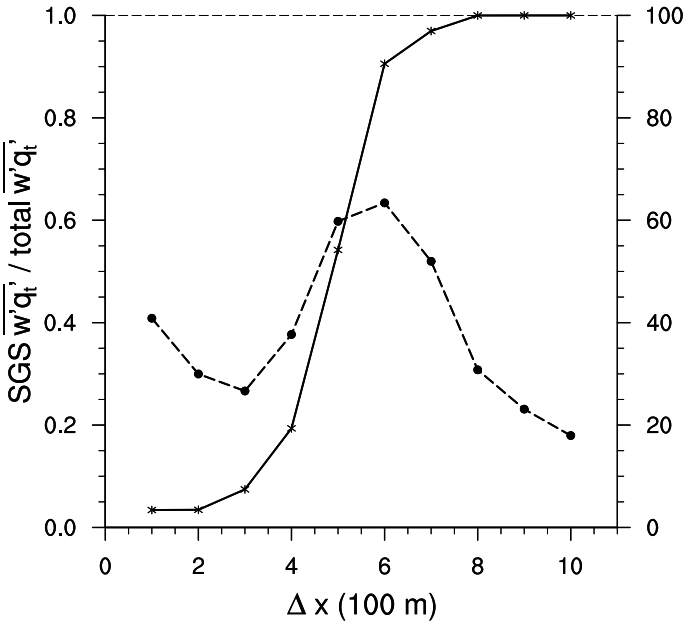

Figure 4.8: Ratio between subgrid and resolved flux of q_t (solid line), and standard deviation of subgrid flux (dashed line), averaged horizontally, over three hours, and over the heights between 400 and 2000 m.

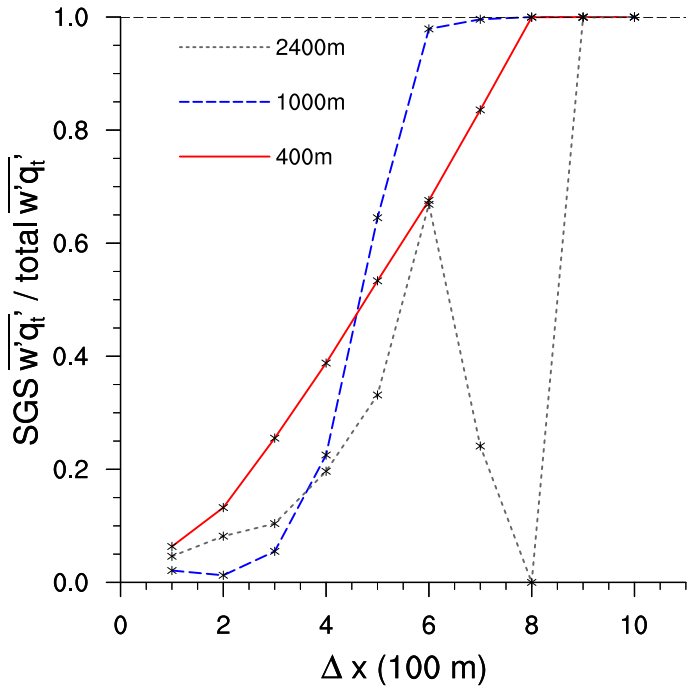

Figure 4.9: Ratio between subgrid and total flux of q_t (solid line), averaged horizontally and over three hours, for heights of 400, 1000, and 2400 m.

4.3.2 Energy Spectra

Though it is important that the ED(MF)^n is able to resolve clouds depending on resolution, also the total energy of the flow should be consistent. Therefore, we analyzed the spectrum of the LES for different resolutions (Figure 4.10). For the LES simulations, different resolutions were shown to alter the variability of the vertical velocity [SAKRADZIJA ET AL., 2016]. Therefore, to avoid this possible problem, for the calculation of the LES spectrum, a simulation with a domain of 512×512 grid points and a resolution of 100 m was conducted and then coarse grained [SHUTTS AND PALMER, 2007] to the coarser resolutions, to act as a reference. Thus, a realistic LES spectrum is given. With decreasing resolution, the energy of the scales smaller than the grid size should be represented by the ED(MF)^n. To calculate the energy of ED(MF)^n, for every group of plumes the energy was calculated as follows:

$$E^{edmfn}(l,z) = \mathscr{A}(l,z)\,\Delta x\,(w_u(l,z) - w_{LES}(z))^2 \tag{4.13}$$

with E the energy, l the index of the updraft number, z the height, Δx the grid box length, w_u the vertical velocity of the individual updraft, and w_{LES} the vertical velocity of the LES. Here, the vertical velocity variance is weighted with the area fraction of the updraft $\mathscr{A}$ and the grid box length to make all updrafts comparable.

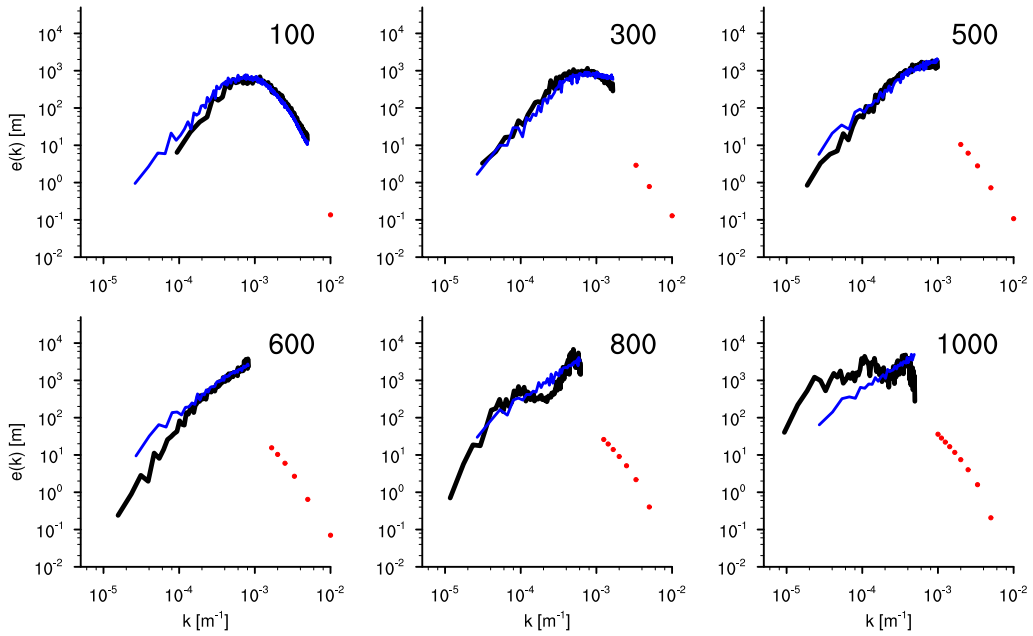

Figure 4.10: Energy spectra of LES (lines) and ED(MF)^n (dots) at a height of 400 m, averaged over three hours, for simulations with resolutions of 100 m, 300 m, 500 m, 600 m, 800 m, and 1000 m. Black line: energy spectra of the original LES with varying domain size and resolutions. Blue line: reference LES with domain size of 512 $\times$ 512 grid points and a resolution of 100 m, coarse grained to the corresponding resolution.

Figure 4.10 shows the spectra of the LES for various resolutions, taken from the "original" LES with various resolutions and from the reference LES coarse grained from 100 m. Also, the energy of the ED(MF)^n updrafts are shown, taken from the original LES with the various resolutions. Both LES spectra show the typical shape of the spectra for the resolution of 100 m [e. g., DE ROODE ET AL., 2004]. For fine resolutions, the difference between the coarse grained reference LES and the original LES is very small. For the resolution of 1000 m, the difference increases, so there seems to be some energy of the small scale processes that is cut off. The number of updrafts of ED(MF)^n increases with decreasing resolution because the number of updrafts included in ED(MF)^n increases. From the simulations with more than one updrafts it can be observed that the small updrafts carry little energy. The larger the updrafts are, the more energy they represent. They complement the spectra of the LES quite nicely, so we conclude that the energy contained in the total flow is consistent.

4.3.3 Sensitivity Studies

In this section, the sensitivity of the results on some choices regarding the setup is tested to gain understanding on the behavior of ED(MF)^n. The differences of these simulations to the original simulation described in the previous sections are listed in table 4.1. All

of these simulations have a smaller domain size, which only negligibly affects the results (not shown) but which saves computing time.

The first sensitivity study regards the scale-adaptivity of the eddy diffusivity. In NEGGERS [2015], the ED(MF)^n scheme is described which includes a scale-adaptive mass flux, while here, the eddy diffusivity was also adjusted (see section 4.2.2). Now, the influence of a scale-adaptive ED is studied by repeating the reference simulation but with the original ED-part without the changes described in section 4.2.2. Further, the effect of the number of updrafts is studied by using 50 updrafts instead of 10, also evenly distributed in size between 0 m and 1000 m, with the updrafts larger than the grid size switched off. Another test investigates the effect of the distribution of the updrafts across resolutions. In the reference simulation, the largest updrafts are not taken into account, which decreases the number of updrafts with increasing resolution. Here, the number of updrafts is maintained for all simulations instead of the size of the updrafts. With increasing resolution the size of the updrafts decreases, but the updrafts are still evenly distributed between 0 m and the resolution of the simulation. Another study concerns the sensitivity of the simulation on the area fraction a covered by the updrafts. In the reference simulation, this fraction has a constant value of 10 %. Now, we run two sets of simulations with constant values of 5 % and 20 %. A last study investigates the influence of the filtering of the updrafts. Here, for all resolutions 10 updrafts are maintained, with sizes between 0 m and 1000 m and without the updrafts larger than the grid size switched off.

A summary of the differences between the different sensitivity studies is given in Figure 4.11, which shows the ratio between the subgrid and the total humidity transport across resolutions. Simulation *noED* is similar to the reference simulation but over-represents the subgrid transport for fine resolutions, indicating that the adjustment made to the scale-adaptivity of the eddy diffusivity is necessary for ED(MF)^n to be truly scale-adaptive. Simulation *50up* shows that the results are not very sensitive to the number of updrafts. 10 updrafts seem to be enough to represent the subgrid transport and indicate a good compromise between a detailed representation of different cloud sizes and economy in computing resources. An advantage of using 50 updrafts is that the discretized steps in the reference simulation seen in Figure 4.6 are smoothed out (not shown), because most of the transport is done by the largest updrafts and in this simulations there is a larger number of large updrafts. For simulation *10up*, the gray zone, i. e., the transition between the clouds being parameterized and resolved, is shifted toward finer resolutions. Cloud condensate and cloud fraction represented by ED(MF)^n are slightly larger for the resolutions in the gray zone (not shown). This difference to the reference simulation could be explained by the larger number of relatively large updrafts for the resolutions in the gray zones, which are able to conduct more transport than in case of fewer updrafts. For the coarse resolution, no change occurs with respect to the reference simulation, because

Table 4.1: Overview over sensitivity studies

	horiz. domain size in grid points	scale-adapt. ED	No. of updrafts	varying updraft size across res.	updraft fraction a	filtered
ref	144×144	yes	10	no	10 %	yes
noED	96×96	no	10	no	10 %	yes
50up	96×96	yes	50	no	10 %	yes
10up	96×96	yes	10	yes	10 %	yes
a5	96×96	yes	10	no	5 %	yes
a20	96×96	yes	10	no	20 %	yes
unf	96×96	yes	10	no	10 %	no

the distribution of the updrafts is similar and all transport is done by the subgrid scales. For the fine resolutions, almost all transport is resolved, which also results in a small difference between simulations *ref* and *10up*. Only in the middle resolutions in between a change is apparent. A similar behavior is found for simulation *a20*, where the larger area fraction of the updrafts also results in larger subgrid transport for the middle resolutions. The same explanation also holds for simulation *a5*, where the behavior goes in the other direction, with the transport smaller in the middle resolutions. When the updrafts are not filtered (simulation *unf*), ED(MF)^n is active independently of resolution and carries out all transport. As expected, this setup is not scale-adaptive at all.

4.4 Summary and Conclusion

In this study the scale-adaptivity of the shallow cumulus parameterization scheme ED(MF)^n was tested. The resolution of weather and climate models continues to increase. With this increasing resolution, processes that have been completely subgrid scale before, now can become partly resolved. The distinction which processes are resolved, which are parameterized, and which can be resolved due to the increasing resolution depends on the type of the model. For all processes that are partly resolved, the parameterization scheme has to adapt, representing only the subgrid-scale processes, especially when a model is regularly run with different resolutions or when nesting is used (with a region of finer resolutions embedded in a coarser-resolution model). This scale-adaptivity of a shallow cumulus parameterization has been investigated for a range of resolutions covering the gray zone.

Since weather and climate prediction models have a large number of parameterization schemes covering all sorts of processes, in this study ED(MF)^n was implemented into an LES, acting as a "play-ground" for testing. The original subgrid-scale scheme was inactivated and replaced by ED(MF)^n. This setup was then run with various resolutions. The advantages of using LES in this context is that it is an idealized model, making the interpretation of the results easier because the signals are not altered by as many other

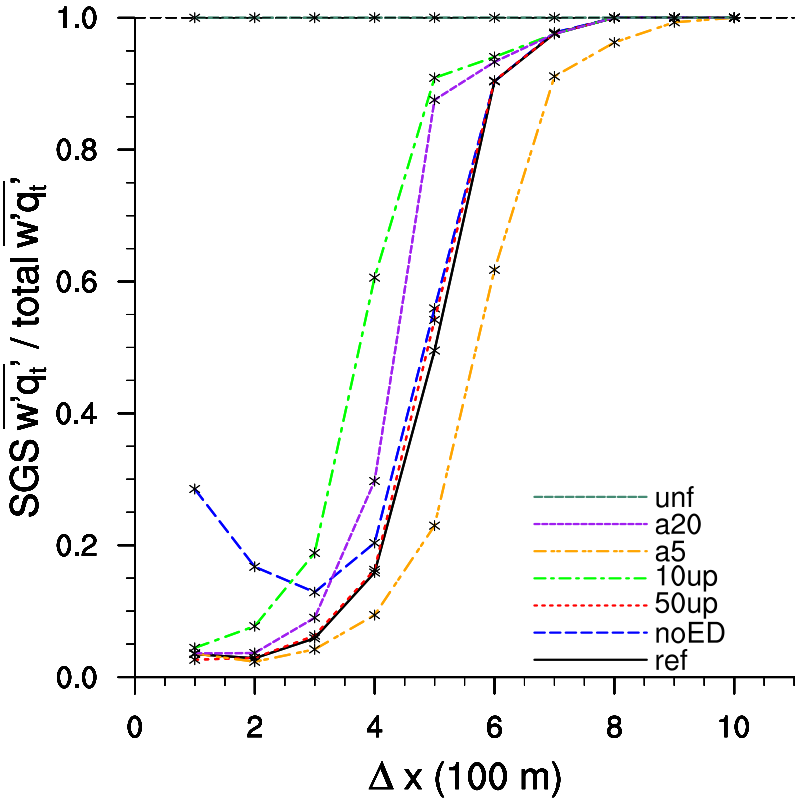

Figure 4.11: Ratio between subgrid and total flux of q_t, averaged horizontally, over three hours, and over the heights between 400 and 2000 m, for different sensitivity studies (see text).

parameterization schemes as exist in global weather prediction models. This way, a clean analysis of the behavior of ED(MF)^n could be performed in a setup that is as simplified as possible while still sophisticated enough to study the behavior of ED(MF)^n.

We could show that the scheme ED(MF)^n developed by NEGGERS [2015] is indeed scale-aware and scale-adaptive. With increasing resolution, a smaller number of plumes is considered and the transport represented by the subgrid scales decreases. At the finest resolution of 100 m, all shallow convection is represented by the resolved scales. For the coarse resolution of 1000 m, no clouds are resolved. In this case, the transport done by shallow cumulus clouds is represented by the parameterization scheme. The total transport is similar across resolutions. There is a small increase in boundary layer height for coarser resolutions, presumably because the physics of the scheme is not without deficiencies.

The scheme studied here is scale-adaptive mostly because the mass flux part of the scheme is scale-adaptive. A method was described to make the ED part of the scheme scale-adaptive as well, by adapting the K parameter. Without this method, the scheme was conducting excessive transport of the eddy diffusivity for fine resolutions. This shows that for a true scale-adaptivity, the ED-part of ED(MF)^n must also be scale-aware. Further sensitivity studies showed that a higher number of updrafts doesn't add much value. Keeping the number of updrafts the same instead of the size of the updrafts, as well as changing the constant total area fraction of the updrafts, leads to a shift of the gray zone.

Several simplifications were made regarding the design of ED(MF)^n. The fraction of the updrafts is always constant. Also, the scheme has no stochastics implemented, which might improve the performance of the scheme. However, even with these simplifications the scale-adaptivity of this scheme could be proven.

For the testing of the parameterization scheme, an idealized model has been used. However, though models can try to describe reality, they need to be continuously compared to observations to test how realistically the processes in the atmosphere are portrayed. Therefore, to further test ED(MF)^n, it should be compared to real observations of shallow cumulus clouds. The setup described in this study could be used to simulate a less idealized case of a shallow cumulus clouds field on a day where observations are available. The representation of shallow cumulus clouds across resolutions can then be evaluated by the observations. This approach is taken in a different study described in chapter 5 of this thesis.

5 Comparing ED(MF)^n in the gray zone to observations

Abstract

This study investigates the scale-adaptivity of a shallow cumulus parameterization scheme with the help of the measurements from the campaign HOPE (High Definition Clouds and Precipitation for advancing Climate Prediction Observational Prototype Experiment), which spans a range of daily cases over land, each covering a diurnal cycle. The parameterization scheme used is ED(MF)^n, consisting of an eddy diffusivity part and a mass flux part. The mass flux part is formulated in terms of discretized size distributions of convective transport and clouds, making use of a multiple plume approach. This framework allows size filtering of parameterized transport, making the scheme in principle scale-adaptive. In the previous chapter this scheme was implemented in a large-eddy simulation (LES) model, replacing the original sub-grid scheme. This way the LES was used as a simplified larger-scale model, acting as a testing ground for scale-adaptive parameterizations. While the approach was explored for idealized marine subtropical conditions, in this study we progress to more complex, and therefore more challenging shallow cumulus situations over land. With the data from the weather prediction model COSMO-DE, the LES is nudged, resulting in a close representation of the measured conditions. During the HOPE-campaign the boundary layer was measured extensively. Three individual days were chosen, each describing a different diurnal cycle of boundary layer convection. The LES is run with and without ED(MF)^n for various resolutions, and the modeled boundary layer is compared to the observations from HOPE.

5.1 Introduction

For the development of parameterization schemes, large-eddy simulation (LES) models are a valuable tool, often used as a virtual laboratory for constraining and informing the development of parameterizations for larger-scale circulation models. With LES atmospheric processes can be studied, which helps us to improve our understanding of these

processes. LES can act complementary to observations since it provides highly resolved three-dimensional data, but it needs to be evaluated with observations to ensure that the conclusions drawn from the simulations are transferable to the atmosphere. LES models are designed to study various processes in a more idealized way [e. g., GRYSCHKA AND RAASCH, 2005; VAN DER DUSSEN ET AL., 2015]. Setups of idealized cases are often based on measurement campaigns, using the measurements to build an idealized case of a certain atmospheric regime to study the processes within this regime [HOLLAND AND RASMUSSON, 1973; SIEBESMA ET AL., 2003; RAUBER ET AL., 2007; VANZANTEN ET AL., 2011].

The classic way of using LES for parameterization development is to use its output data for informing new ideas and to constrain constants of proportionality. A novel way of using LES has been explored in chapter 4, and is inspired by recent developments in parameterization. The ever increasing resolutions in general circulation models has prioritized the development of scale-adaptive parameterizations. How to best test such schemes remains an open research question. This is where LES can play a role, by acting as a simplified and highly transparent circulation model for testing such new schemes, across a range of resolutions that covers the gray zone. A fully scale-adaptive scheme should then be suitable to be applied across a broad range of resolutions, from typical climate model discretizations of tens of kilometers, down to LES grid spacings of about 100 meters. Such a scheme should adjust its contribution to transport and clouds to the discretization of the model in which it is implemented. Only those processes that cannot be resolved by the model should be represented by the parameterization scheme. Further information about the parameterization of shallow convection and an overview over various parameterization schemes developed so far is given in chapter 4. There, the parameterization scheme ED(MF)^n (the Eddy Diffusivity multiple Mass Flux scheme) is described in detail, which is used also in the following study. This scheme combines the eddy diffusivity approach, representing small-scale turbulent transport, with the mass flux approach, where multiple updrafts are launched in each column, and each updraft represents an ensemble of clouds of a certain size. The scheme is designed to be scale-adaptive, as it allows the filtering out of the contribution by those plumes that are larger than a certain cut-off length, which can be assumed proportional to the grid-spacing.

The testing of the parameterization scheme of shallow cumulus clouds ED(MF)^n within an LES model is described in chapter 4 of this thesis. Experiments with this setup for the idealized marine quasi-steady state RICO case yielded promising results, showing true scale-adaptive behavior of the ED(MF)^n across the boundary layer gray zone. However, to further test the general applicability of the framework it is important to study if this conclusion holds for a more complex case. To this purpose in this study the setup of the previous chapter will be explored for a set of cases describing diurnal cycles of convec-

tion over land. This set is designed to include a range of different convective regimes, including a dry convective boundary layer, a shallow cumulus topped boundary layer and a boundary layer including deeper shallow cumulus convection. These cases are selected from the HOPE campaign (High Definition Clouds and Precipitation for advancing Climate Prediction Observational Prototype Experiment, MACKE ET AL. [2017]). To achieve a somewhat realistic simulation, the method used by NEGGERS ET AL. [2012] is applied, where model output from an operational weather prediction model is used to initialize and nudge the simulation. HEINZE ET AL. [2016], and also SCHALKWIJK ET AL. [2015], are later examples in which this technique was successfully applied. Then, to study the performance of this setup, the simulation is evaluated with a selection of independent measurements of the kinematic, thermodynamic, and cloudy state of the boundary layer. To test the scale-adaptivity of the parameterization scheme, this setup is run at various resolutions covering the gray zone. Each of the simulations is then compared to observations, and the behavior of the SGS scheme is investigated as a function of the grid-spacing. The main research objective is to investigate how the scale-adaptivity materializes in highly transient situations, during which the boundary layer evolution is significant.

Section 5.2 describes the setup of the simulations and the measurements used. In section 5.3 the ability of LES to represent the observed weather situation is evaluated by comparing the simulation to observations, and the scale-adaptivity of ED(MF)^n is tested for this case over land and with diurnal cycle, followed by a summary and a conclusion in section 5.4.

5.2 Methods

5.2.1 Case Configuration

The aim of this study is to evaluate the scale-adaptivity of the parameterization scheme ED(MF)^n in a semi-idealized setup over land and with a diurnal cycle, with ED(MF)^n implemented into UCLALES. The configuration of the implementation of a semi-realistic case into the UCLALES is the one that was described by HEINZE ET AL. [2016]. The large-scale forcing in the LES is implemented by prescribing the large-scale pressure gradients, horizontal advection, and vertical motion. This forcing is here taken from the regional numerical weather prediction model COSMO-DE [BALDAUF ET AL., 2011] (hereafter COSMO). The surface of our model domain is homogeneous, and the horizontal boundaries are cyclic. Therefore, the large-scale forcings change only over time and are spatially homogeneous, i. e., the profile of prescribed tendencies is identical at each grid location. To avoid that the simulation slowly drifts away from the conditions observed in nature, UCLALES is nudged at every time step toward the profiles from COSMO. The strength of the nudg-

ing is determined by the relaxation time, which in our case is 6 hours. This time span is small enough to introduce large-scale synoptic disturbances into the domain, while it can be assumed large enough to allow the turbulence and the shallow convection in the LES to develop their own unique state. The COSMO data is taken from the weather analysis, which besides model output includes assimilated observations. This data is available every 3 hours with a horizontal resolution of 2.8 km. To feed our LES with large-scale forcing at every time step, the COSMO data is interpolated in time. To ensure that the COSMO-data only represents large-scale forcing without including the small-scale processes that are resolved by the LES, the COSMO data is averaged spatially within a domain of $2^\circ \times 2^\circ$ centered over the HOPE area. For more details about the large-scale forcing see HEINZE ET AL. [2016].

5.2.2 Model Setup

As in the previous chapter, the LES used is the UCLALES, described in STEVENS ET AL. [2005]. ED(MF)^n is included into LES by replacing the original Smagorinsky-based SGS scheme of the LES. In each column of the LES, a number n of updrafts is initialized, conducting the mass flux part of the transport ("MF"). Also, the transport done by eddy diffusivity is included with the "ED"-part of the scheme. In the mass flux part, entrainment is included by prescribing an entrainment rate to the rising plumes which is inversely depending on plume size. For each simulation, only those plumes smaller than the grid size are taken into account, while the larger plumes are filtered out. This filtering introduces scale-adaptivity to the "MF"-part of the scheme. The "ED"-part of the scheme is made scale-adaptive by adjusting the coefficient K_h in formulation (4.5). For the cloud layer, K_h from the LES is compared to K_h of ED(MF)^n, and the smaller value is used as K_h. In the subcloud layer, the pragmatic blending approach by BOUTLE ET AL. [2014] is used, weighing K_h so that it resembles K_h of the LES for fine resolutions and for coarse resolutions, K_h resembles the K_h from ED(MF)^n (see also section 4.2.1).

For this study, two types of simulations are conducted: (i) reference simulations without ED(MF)^n and (ii) simulations with ED(MF)^n implemented into LES. The reference simulations in this study are run with a horizontal resolution of 100 m, while the simulations with ED(MF)^n have resolutions ranging from 100 m to 1000 m. All simulations have a horizontal domain size of 96×96 grid points, which results in larger domain sizes for the simulations with coarser resolutions. The vertical resolution is 50 m with 144 grid points and stretched starting at 5000 m, resulting in a height of the domain of about 13 km. The simulation time spans 24 h and starts at midnight. At the beginning of the simulations some time is needed for spin-up, but since the first hours of the day are not relevant for studying convection, this does not present a problem. Every 200 s, the subgrid scheme

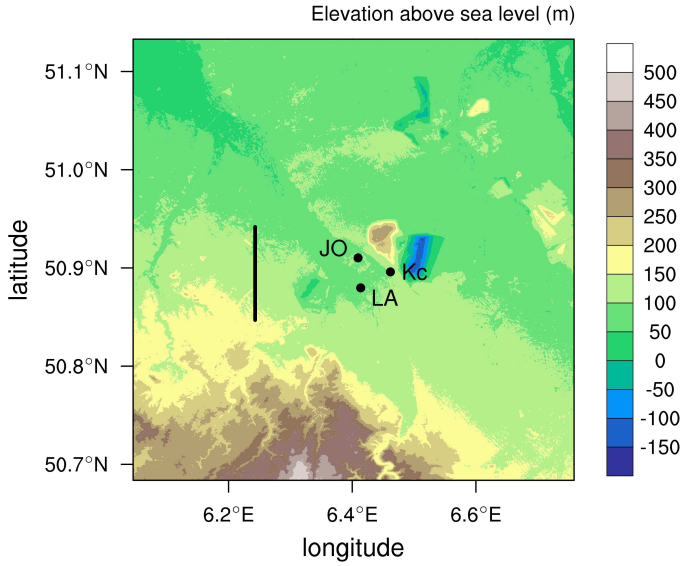

Figure 5.1: Map showing the area around the HOPE measurement site. The three supersites are denoted as JO for JOYCE in Jülich (Jülich Observatory for Cloud Evolution), Kc for KITcube in Hambach (Karlsruhe Institute of Technology cube), and LA for LACROS in Krauthausen (Leipzig Aerosol and Cloud Remote Observations System). The vertical line indicates the horizontal dimension of the reference LES simulation. The map is adapted from HEINZE ET AL. [2016] with data from ASTER GDEM VALIDATION TEAM [2011].

ED(MF)^n is called. The area around HOPE exhibits mostly agriculturally used land without major hills, therefore we feel justified in using a homogeneous surface.

5.2.3 Simulated Days During The HOPE Campaign

The HOPE campaign was designed to evaluate the icosahedral non-hydrostatic model (ICON) and to study subgrid variability and microphysical processes [MACKE ET AL., 2017]. The main campaign took place in Jülich at the permanent supersite JOYCE (Jülich Observatory for Cloud Evolution [LÖHNERT ET AL., 2015]) located at the research center. In addition, measurements were taken at the two other supersites Krauthausen and Hambach, which together with JOYCE, are each about 4 km away from the other supersites. Other instruments and measurements complement these three supersites, e. g., pyranometers and sky imagers. A map of the region is shown in Figure 5.1. The measurement area is rather flat except for the hill Sophienhöhe caused by the pit mine nearby. South of the region the low mountain range Eifel is located.

Measurements from the HOPE campaign used in this study are the radiosonde data, which were launched at least every 6 hours at the KITcube (the Karlsruhe Institute for Technology mobile facility) in Hambach. Additionally, microwave radiometer data from Jülich and Hambach, a Total Sky Imager, ceilometer, and a wind lidar, stationed at Jülich, were

Table 5.1: overview over instruments used in this study

instrument	location	variable used	reference
radiosondes	KITcube	profiles of temperature and humidity and z_i	KALTHOFF ET AL. [2014]
microwave profiler Humidity and Temperature Profiler HATPRO	JOYCE	liquid water path (LWP), integrated water vapor (IWV)	LÖHNERT ET AL. [2015]
total sky imager TSI880	JOYCE	cloud cover	LÖHNERT ET AL. [2015]
ceilometer CHM15k	JOYCE	cloud base height, cloud cover	LÖHNERT ET AL. [2015]
wind lidar HALO Photonics Doppler lidar	JOYCE	boundary layer height (z_i)	SCHWEEN ET AL. [2014]
Cloudnet	JOYCE	cloud top height	ILLINGWORTH ET AL. [2007]

used. Also, the Cloudnet target classification was used [ILLINGWORTH ET AL., 2007]. The instruments and variables used in this study are summarized in table 5.1. For an overview over all measurements taken during HOPE see MACKE ET AL. [2017].

The HOPE campaign took place in April and May 2013. During this period, a variety of weather conditions occurred, ranging from the passages of fronts to high pressure systems. From the two month of data, three days were chosen for this study to evaluate the performance of the parameterization schemes for different conditions. These three days are April 24, 2013, May 2, 2013 , and May 6, 2013. The weather situation of these three days is illustrated in Figure 5.2, showing the cloudnet target classification from Jülich [ILLINGWORTH ET AL., 2007]. April 24 shows a clear sky, May 2 has cumulus developing into stratocumulus and a relatively high cloud fraction. On this day, some rain is present during the day. On May 6, the boundary layer develops late in the day. Some shallow cumulus clouds form and the boundary layer becomes relatively deep. In greater heights, above the boundary layer, some ice clouds form. Thus, we study how well the parameterization schemes deals with dry, forced, and free convection.

5.3 Results

5.3.1 Reference simulations without ED(MF)^n

Prior to investigating the scale-adaptiveness of ED(MF)^n, it is essential to gain confidence in the realism of the reference LES simulation of the selected cases. The reference simulation is the one at the highest resolution (100 m), at which the boundary layer turbulence and clouds can be assumed to be reasonably well resolved. With this simulation, it is tested if the forcing of the LES with COSMO-data can reproduce the conditions observed by the

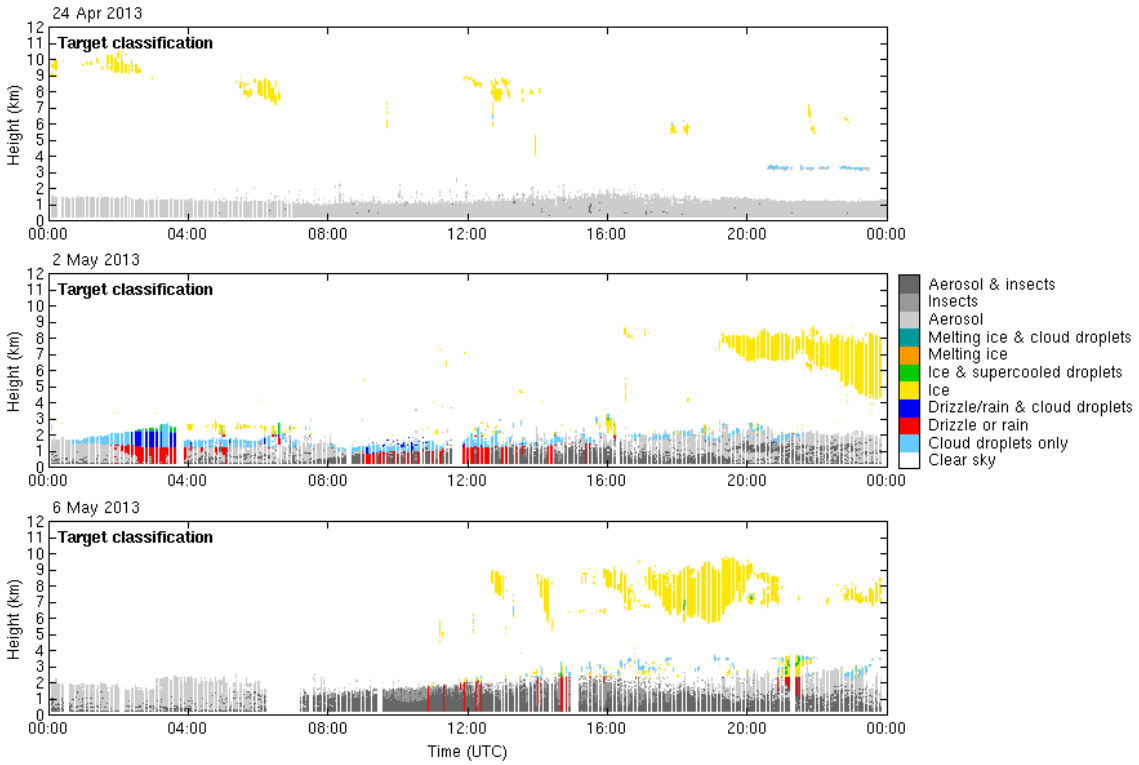

Figure 5.2: Cloudnet target classification of three chosen days.

instruments during the HOPE campaign. Therefore, UCLALES in its original version, without the parameterization scheme implemented, is compared to observations. This setup then serves as a reference simulation for the following evaluation of ED(MF)^n. While for the simulations with ED(MF)^n implemented into LES a variety of horizontal resolutions will be used, for the reference simulations a relatively fine resolution of 100 m is used.

Thermodynamic State

The integrated water vapor (IWV) is compared in Figure 5.3. Though the measurements are point measurements and the LES data can only provide a horizontal average over an area because of the prescribed forcing, we assume that the data are suited for comparison because data from the three supersites were studied, thus giving insight into the variability of the variables. While the measured IWV is integrated from the surface to the top of the atmosphere, for the LES, the IWV can only be integrated until the top of the model domain, which is at about 13 km. However, the amount of water vapor above 13 km is typically more than an order of magnitude smaller than that below this level, and can therefore be ignored in this comparison. The LES profiles are averaged over the whole domain for better representativity. For April 24 and May 2, the IWV from observations and the LES agree well, while for May 6, the IWV is slightly overestimated, though the trend is

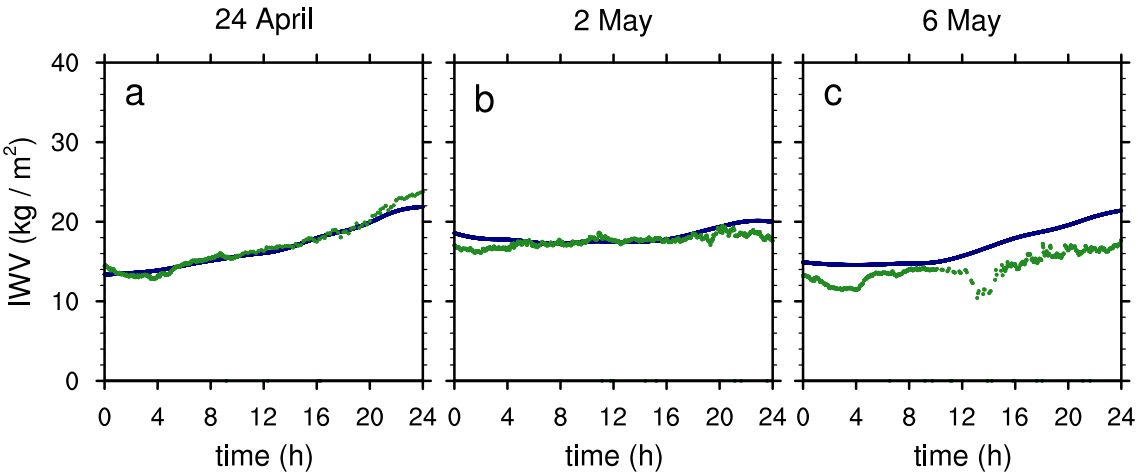

Figure 5.3: Time series of observed (green) and simulated (blue) integrated water vapor for the three days.

captured by the model.

In Figure 5.4, the profiles from radiosondes taken at 11 UTC are compared with the model profiles (averaged over the domain). For all days, the main characteristics are well captured by the model, though the mixed layer is always slightly too cold and strong gradients in the humidity are not captured by the model. For April 24 and May 2, radiosonde data at other times are available, which also show that the model is fairly well able to reproduce the various layers like cloud base and inversion as well as their internal gradients, for q_t as well as Θ. Though the representation of the profiles is slightly lacking in detail, for our study we deem the quality of the reproduction to be good enough since the qualitative characteristics are captured well.

Clouds

For April 24, both the instruments and the LES did not detect any cloudiness (Fig. 5.5). On May 6 the liquid water path (LWP) was zero in the first half of the day and increased in the evening, which is shown in the observations and captured by the model. On May 2, the observations show some liquid water in the atmosphere throughout the day. The clouds in the beginning of the day are not captured by the model. These clouds are stratiform clouds which evolved during the night and persisted until they are dissolved by the development of convection. This kind of cloud is difficult for LES to capture because the formation of those clouds is very sensitive to the atmospheric conditions, so the LES has to be provided with a very accurate atmospheric state by the forcing of COSMO. However, these clouds are not the focus of this study, since we are interested in the surface driven convection between sunrise and sunset. Later in the day when convection develops, the

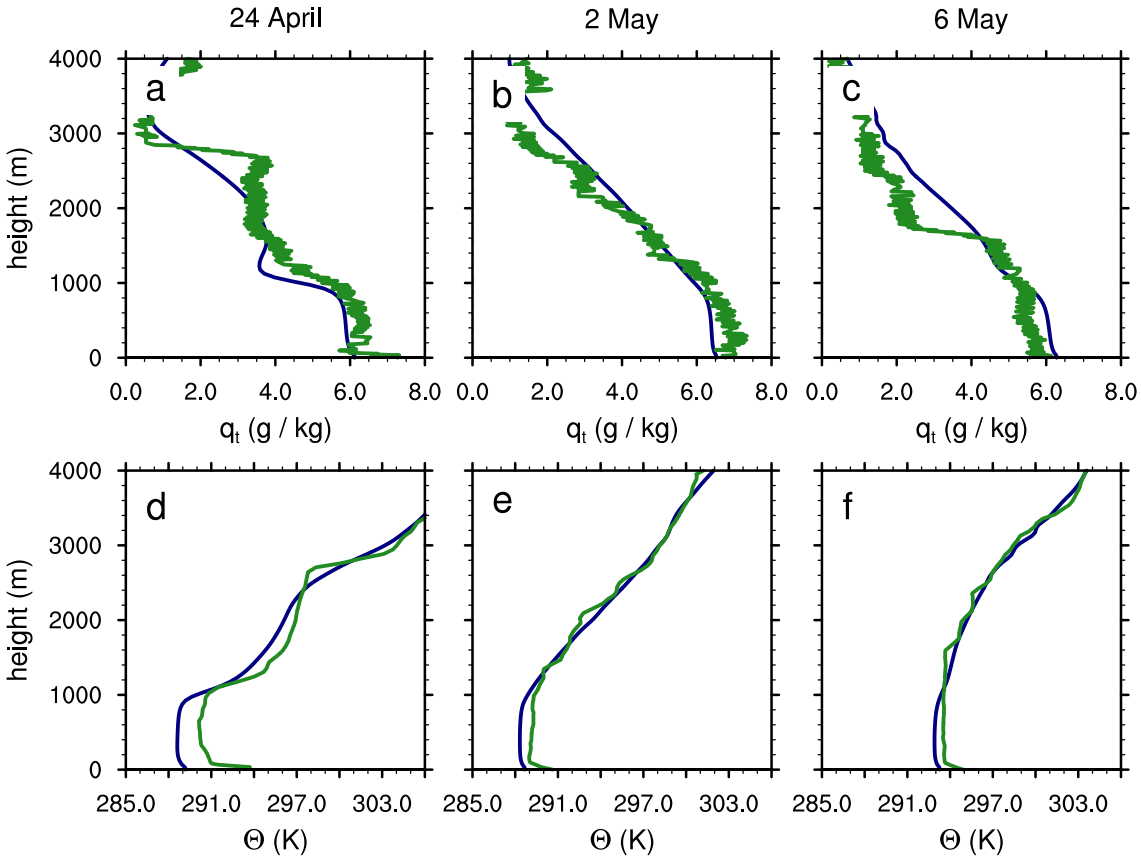

Figure 5.4: Vertical profiles of total water mixing ratio (top) and potential temperature (bottom) measured by radiosondes (green) and simulated and horizontally averaged (blue) at 11 UTC for three days.

LES captures the amount of LWP. The gap of LWP in the observations in the middle of the day is caused by chance, since the measurements are taken only at the column directly above the instrument. This gap does not occur for the HATPRO stationed a bit farther away at Hambach (not shown). During the evening, the higher LWP is captured by the model. These results are in agreement with the results from HEINZE ET AL. [2016] (their Fig. 6), though they were able to capture the clouds in the beginning of May 2, maybe because they simulated 19 days continuously, while in our setup each day is initialized at midnight and the first hours are needed for the spin-up. The time series of the cloud cover simulated by LES is shown in Figure 5.6 for the two days where clouds occur. Here, it is obvious that at the beginning of the simulation the clouds on May 2 are mostly missed, but the clouds developing during the day are captured.

The time series of the cloud fraction is shown in Figure 5.7. Two instruments were used to determine the cloud fraction. The ceilometer (CHM15k, LÖHNERT ET AL. [2015]) gives a cloud fraction divided into eight discreet intervals, and cloudmask data from the total sky imager (TSI880, LÖHNERT ET AL. [2015]) was used to calculate the cloud fraction,

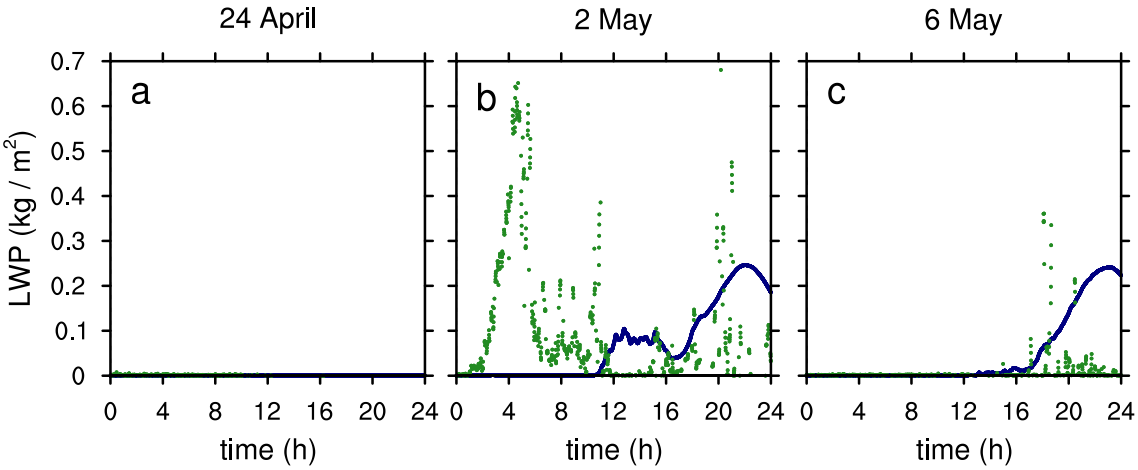

Figure 5.5: Time series of observed (green) and simulated (blue) liquid water path for the three days.

where thin and opaque clouds are counted as cloudy pixels. The data for April 24 shows a low cloud fraction and low LWP in the observations for parts of the day (especially in the first half of the day), which is not captured by the LES. The cloudnet classification shows some high ice clouds above the boundary layer during the day (Fig. 5.2), which explains this difference between observations and LES. For May 2, the cloud fraction agrees well between both observations and LES for the second half of the day. Before sunrise, the LES misses the clouds (see also Fig. 5.5). For May 6, observations and LES agree very well, except for the beginning of the day, where the observations show a small cloud fraction, whereas the LES shows no clouds. However, our focus is on daytime convective clouds, and the occurrence of nighttime clouds depends heavily on the forcing applied to the model and on chance.

Overall, the LES is well able to capture the clouds measured on the three days. Though it misses some clouds before sunrise on May 2, the daytime convective clouds are well captured, since cloud top, cloud base and the amount of LWP are well reproduced. Especially on this day the development of the cloud layer is in agreement with previous studies of continental cloud layer development with clouds developing before noon, rising cloud base during the day and deepening cloud layer [e. g., ZHANG AND KLEIN, 2013]. For all three days, the amount of simulated clouds as well as their time evolution are well captured. Though a larger number of studied days would improve the statistics, for our purpose we deem these three days to be representative since they show the same typical cloud characteristics as seen in other studies of shallow cumulus days over land [e. g., BROWN ET AL., 2002; ZHANG AND KLEIN, 2013].

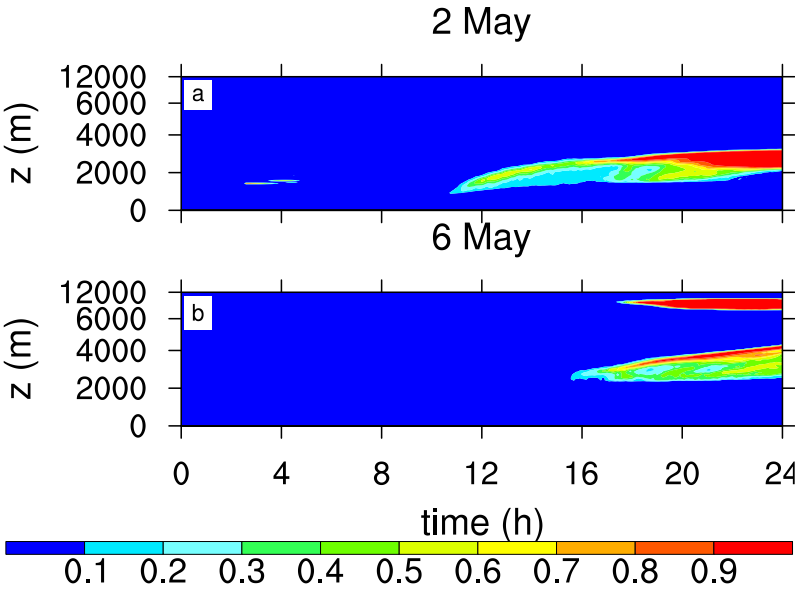

Figure 5.6: Time series of profiles of resolved cloud fraction for the two shallow cumulus days.

Boundary Layer Heights

To study the evolution of the boundary layer height (BLH), this height must first be defined, since there are many different ways to determine it. Here, the BLH from the LES is determined by the Richardson number. The gradient Richardson number is the ratio between turbulence and wind shear. The bulk Richardson number approximates the gradient Richardson number by finite differences between layers:

$$Ri_{bulk} = \left(\frac{g}{\Theta_{v,\text{surface}}}\right) \frac{\Theta_v - \Theta_{v,\text{surface}}}{u^2 + v^2} z, \tag{5.1}$$

with g the gravitational constant, Θ_v the virtual potential temperature, z the height, and u and v the horizontal wind velocities. Here, the layer across which the bulk Richardson number is calculated, is the layer between the surface and the height z. To determine the BLH, a critical value is assumed: $Ri_{bulk,c} = 0.25$. The height, where this critical value is exceeded, is then taken as the BLH. The BLH is determined for every column in the LES and then averaged horizontally. The bulk Richardson number has been used in the literature for decades to determine the BLH [e. g. TROEN AND MAHRT, 1986; HEINZE ET AL., 2016], and various critical values were assumed. Our value for $Ri_{bulk,c}$ lies in the range of values used in the literature [RICHARDSON ET AL., 2013].

To determine the BLH from measurements, several methods are used. The BLH is calculated using the radiosondes and determining Ri_{bulk}. Also, the wind lidar is used to determine the BLH with the method from SCHWEEN ET AL. [2014]. Here, the standard

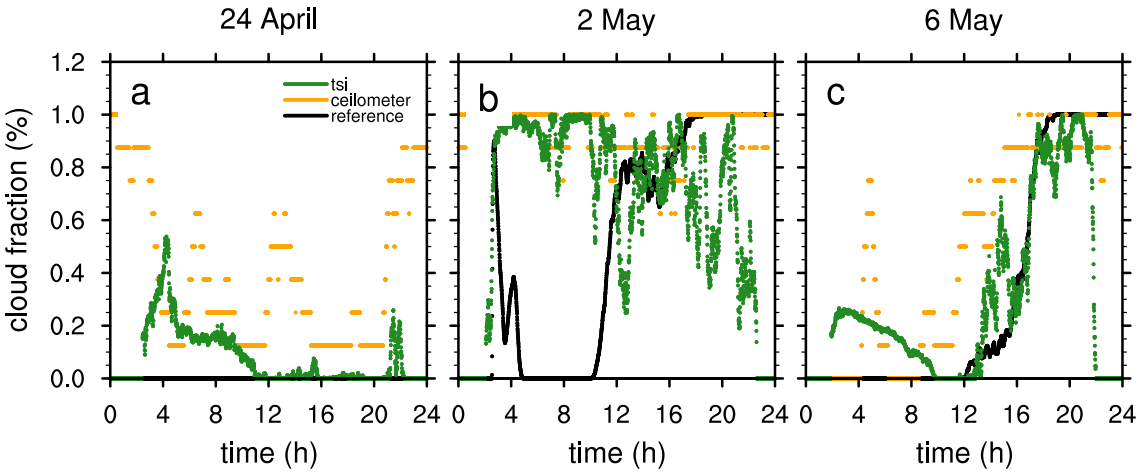

Figure 5.7: Time series of simulated resolved cloud fraction (black), and measured cloud fraction by the total sky imager (green) and the ceilometer (orange) for the three days.

deviation σ_w of the vertical wind is calculated every 5 minutes, taking into account 30 minutes of data (15 minutes before and after the time where σ_w is calculated). σ_w is then used to determine the termination height of the rising plume. Above that height, σ_w decreases; thus, the height where σ_w falls below a threshold value for the first time is taken as the BLH. This threshold value is taken as 0.4 m/s [SCHWEEN ET AL., 2014].

The various methods of determining the BLH yield a range of different heights. Also, it is not clear if the boundary layer includes clouds, thus if the BLH gives the height of cloud top, or if it excludes clouds. Thus, an intercomparison between the different measures of the BLH from both measurements and the model is difficult. To overcome this problem, we interpret the spread of BLHs as the height range covered by the shallow convective cloud layer. In Figure 5.8, the different BLHs from LES and measurements are shown. For most of the day of May 2, the BLH from LES and the wind lidar agree very well. Only at the end of the day, the LES does not capture the abrupt decrease of the BLH. The radiosonde data show a much larger BLH. This could be due to the fact that the BLH determination with the Richardson number is sensitive to the vertical profile of temperature, which the LES does not capture in all its details (see Fig. 5.4). An alternative explanation for this discrepancy could be the measurement of the radiosonde, which shows a lot of small-scale variation. Also, the radiosonde might have risen through a cloud at this stage, creating a deviation in the profile that does not reflect the wider area. Other measurements shown are the cloud base and the cloud top calculated from the target classification of cloudnet [ILLINGWORTH ET AL., 2007]. It can be seen that indeed all observed estimates are 'enveloped' by the LES cloud base height and inversion height. Thus, we conclude that the boundary layer height can be reasonably well determined by the LES. A similar development of the BLH was found by HEINZE ET AL. [2016]. Similar results were found for April 24 and May 6, though on May 6 there was only one radiosonde and on April 24 there are no clouds.

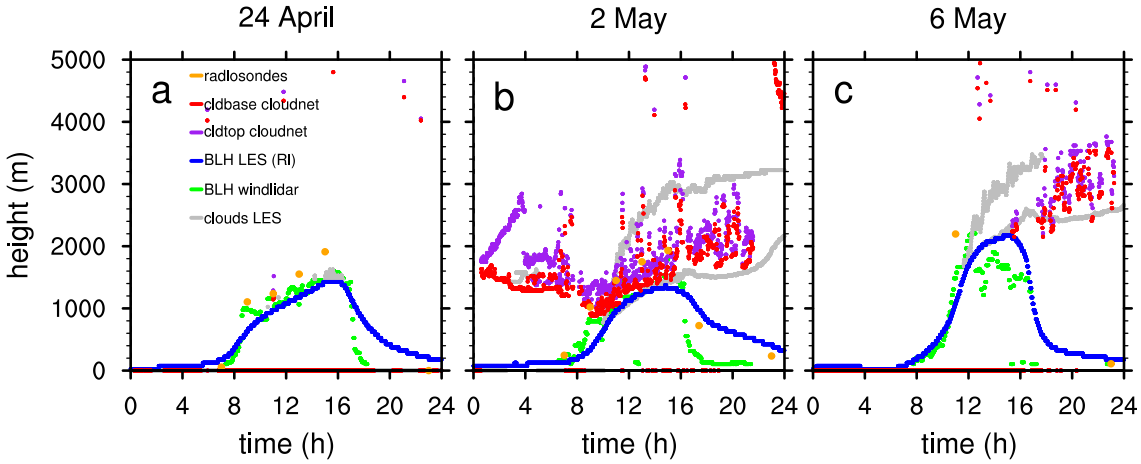

Figure 5.8: Time series of boundary layer height calculated from radiosondes (orange), the wind lidar (green) and the simulation (blue), and simulated cloud top and cloud base height (gray), and cloud top (purple) and cloud base height (red) from cloudnet for the three days.

Here, the radiosonde data still indicate a larger BLH than those from lidar or LES, but the difference is not as large as for May 2.

5.3.2 Simulations with various resolutions with ED(MF)^n

The previous section showed that the LES is able to reproduce the atmospheric conditions of the three days with different weather situations. In this section, the parameterization scheme ED(MF)^n is tested in a similar way as in chapter 4. There it was found that ED(MF)^n is scale-adaptive for a marine situation without transition. Now, the performance of ED(MF)^n is tested for a set of more complex cases, all describing diurnal cycles of boundary layer convection over land. Specifically, we focus on the scale-adaptivity of the scheme by investigating if the scheme is able to represent the clouds that the LES cannot resolve. Especially, the transport of temperature and humidity is studied, since a scale-adaptive scheme adjusts to the transport resolved by the large-scale model, here the LES, and only represents the subgrid-scale transport.

Figure 5.9 shows the profiles of temperature and humidity for the simulations of LES with ED(MF)^n for four different resolutions for the three days. Overall, this gives a first indication that ED(MF)^n can reproduce the main characteristics of the atmosphere for all resolutions. For May 2, the profiles for all resolutions closely follow the profiles of the reference simulation. For the other two days, the boundary layer height increases for coarser resolutions. This increase in BLH also appeared for the simulations of the RICO case (chapter 4). Further research is ongoing into the exact reasons for this behavior. Also, for coarse resolutions the humidity in the mixed layer decreases and the temperature increases slightly. For May 6, some wiggles occur in the profiles, which might have numerical

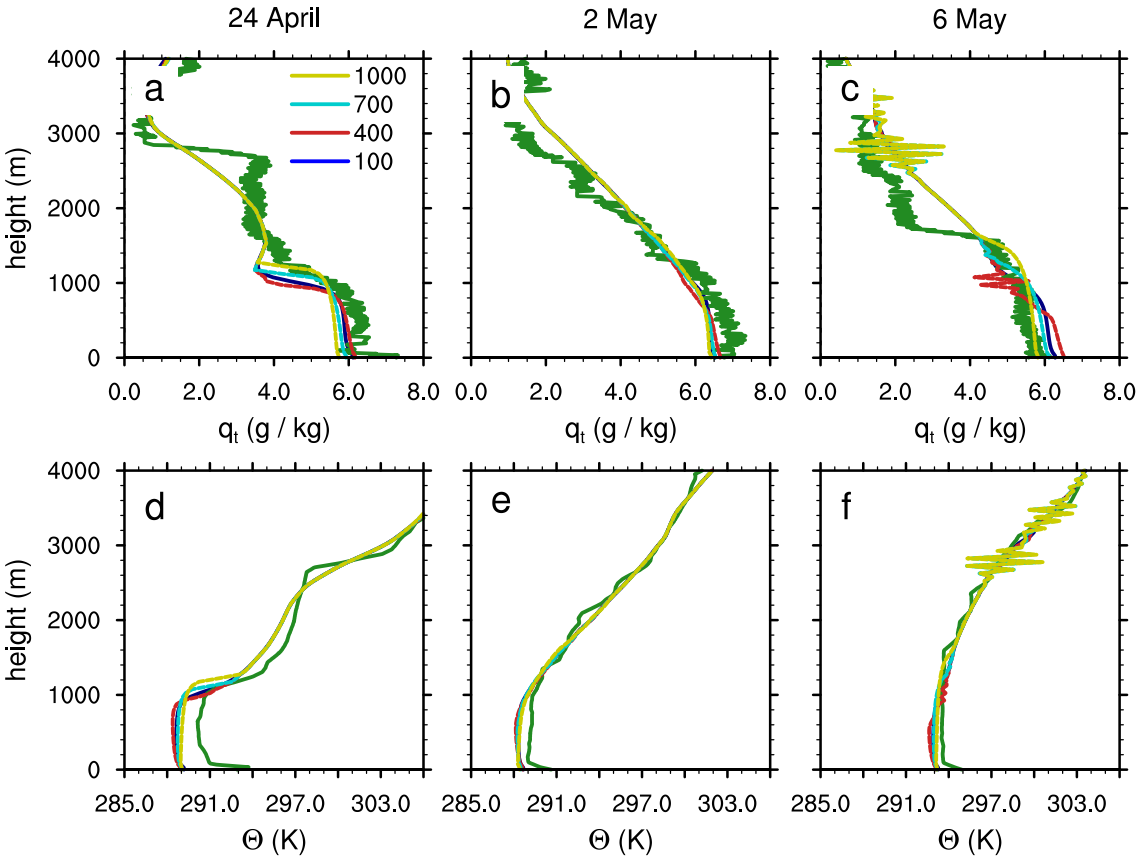

Figure 5.9: As in Figure 5.4 with profiles of the simulations with different resolutions (colors).

reasons. The general difference between the control LES run and the observations as established in the previous section (strong gradients in the humidity are not captured well and the mixed layer is too cold) also materializes in the simulations with ED(MF)^n as the subgrid scheme, for all resolutions. The difference between simulations and observations is larger than the difference between the simulations with different resolutions.

In a similar fashion, the representation of the cloud layer boundaries is shown in Figure 5.10. Shown are the boundaries of the layer of resolved liquid water in the LES, i. e., the cloudtop and cloudbase heights for the reference simulation and the simulations with four different resolutions (crosses in the figure). Also shown are the maximum termination heights of the plumes within the domain (determined with the maximum height of nonzero cloud fraction). Though almost no clouds are simulated for April 24, the plumes are active in the mixed layer. The maximum plume termination height agrees well with the BLH as diagnosed in the reference LES, reproducing the distinctive gradual reduction in the deepening rate of the convective boundary layer as diurnal time progresses. One concludes from these results that the ED(MF)^n as a scale-adaptive SGS scheme is well capable of reproducing the bulk statistics of the evolving dry convective boundary layer across the gray zone. On May 2 for higher resolutions of up to 400 m, the clouds seem to

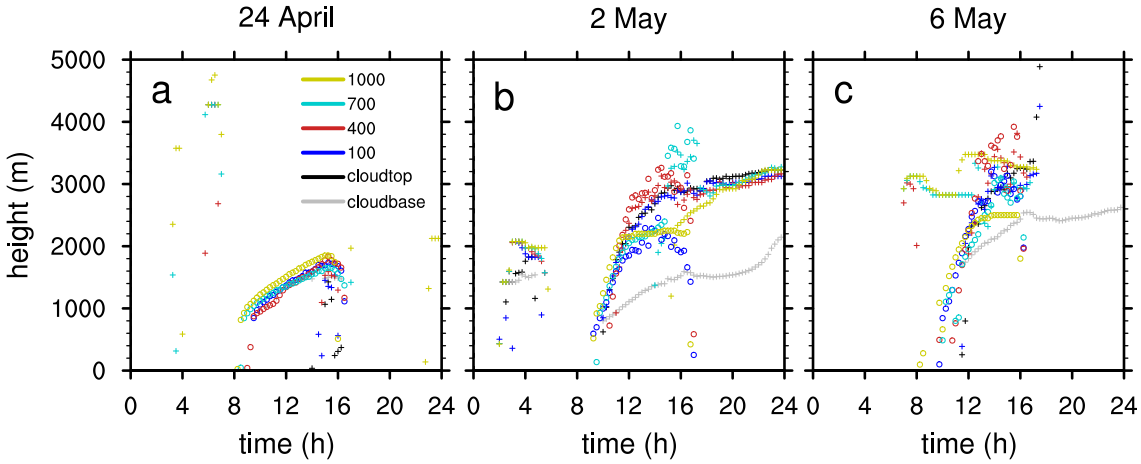

Figure 5.10: Resolved cloud top and cloud base heights (crosses) and subgrid maximum height of nonzero cloud fraction of ED(MF)^n (circles) for the reference simulation (black and gray) and the simulations with ED(MF)^n for different resolutions (colors), all averaged over 15 minutes and for the three different days.

be fairly well resolved and cloudtop and cloudbase heights agree well with the reference simulations. For a resolution of 100 m the rising plumes stop early. This is caused by the size filtering, as it effectively removes the contribution by all plumes larger than 100 m that have the capacity to reach great termination heights. The LES acts to resolve the instability that remains, which gets increasingly associated with cloudiness towards higher resolutions. For coarser resolutions, the clouds are not resolved during the development of the convective boundary layer. Only later in the day, when the intensity of the convection decreases, resolved cloudiness appears in the simulations. For a coarse resolution of 1000 m, though the plumes stop rising at about 2200 m, the transition from plume termination height to resolved clouds is fairly smooth when convection starts to decay. For May 6, some clouds appear for coarser resolutions before convection develops, but these are high clouds detached from the boundary layer. This is probably an artifact of the setup, because the subgrid-scale mixing in LES is increasingly done by the ED(MF)^n, which differs in its behavior from the Smagorinsky scheme from the reference simulation and for coarse resolutions is not active enough.

Figure 5.11 shows the resolved cloud fraction for the simulations with the different resolutions. For May 2, the resolved cloud fraction during the day starts later with decreasing resolution. For May 6, the cloud fraction starts earlier for coarser resolutions because of the high non-convective clouds due to the setup, described above. These results correspond well with those seen in Figure 5.10.

The resolved and parameterized liquid water mixing ratio for the three days for resolutions 100 m and 1000 m are shown in Figure 5.12. For high resolutions, almost all liquid water is resolved by LES. For coarse resolutions, more liquid water is represented by ED(MF)^n.

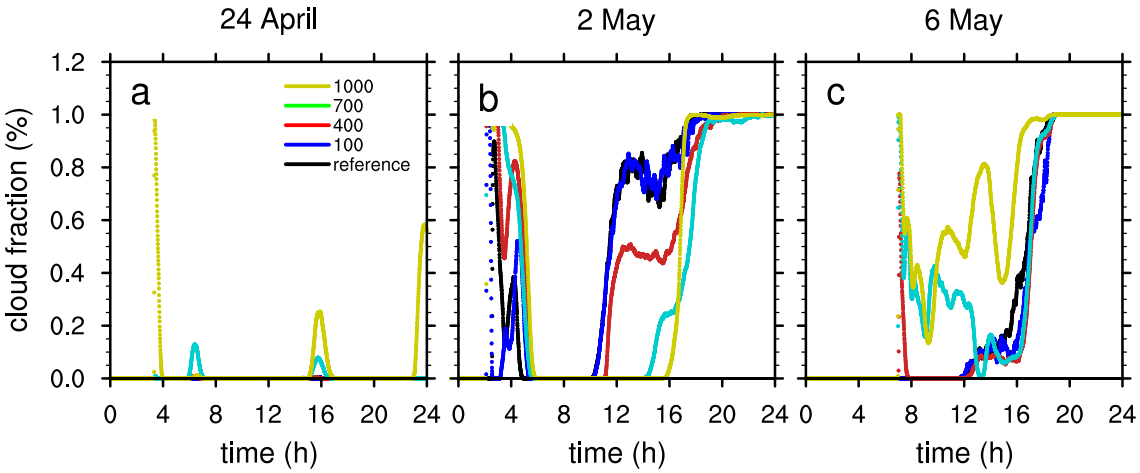

Figure 5.11: Time series of simulated resolved cloud fraction from the reference simulation (black) and the simulations with ED(MF)^n with different resolutions (colors) for the three days.

ED(MF)^n is only active during the convective phase of the day, therefore the liquid water is exclusively represented by LES for the morning and the developing clouds in the evening. For May 2, the convective liquid water is fully represented by ED(MF)^n for coarse resolutions for the time where convection occurs, while for May 6 some liquid water is also represented by LES. Obviously, for the dry day of April 24 hardly any liquid water exists.

These Figures show that the weather situations of the three days are all fairy well represented for the simulations with ED(MF)^n for all resolutions. For coarser resolutions, ED(MF)^n takes over the representation of clouds. To further investigate this scale-adaptivity, profiles of transport and cloud variables are shown in Figures 5.13 and 5.14. These Figures correspond to Figures 4.5 and 4.6 in chapter 4. The total transport has the same order of magnitude for all resolutions and all days, but the differences between the resolutions are larger than for the marine case without diurnal cycle. Also, the increasing BLH for coarser resolutions can be seen. However, the transport for fine resolutions is mostly done by the LES, while for coarse resolutions ED(MF)^n gets more active and takes over the transport (not shown). This is the behavior we are looking for since it shows that ED(MF)^n is scale-adaptive. For the cloud characteristics for fine resolutions, the clouds are resolved by the LES, while for coarse resolutions, the clouds are represented by ED(MF)^n (not shown). However, the total cloud cover and cloud condensate show large differences between the different resolutions. For May 2, the coarse resolutions have a much smaller cloud fraction than for the fine resolutions, and accordingly a much smaller amount of condensate, while for May 6 the coarsest resolution has the largest cloud fraction. The representation of the cloud amount and the cloud height seems to be difficult to capture for coarser resolutions (see also Figure 5.10). In contrast to the flux profiles, the total cloud properties are not quite conserved across the range of resolutions. This is in con-

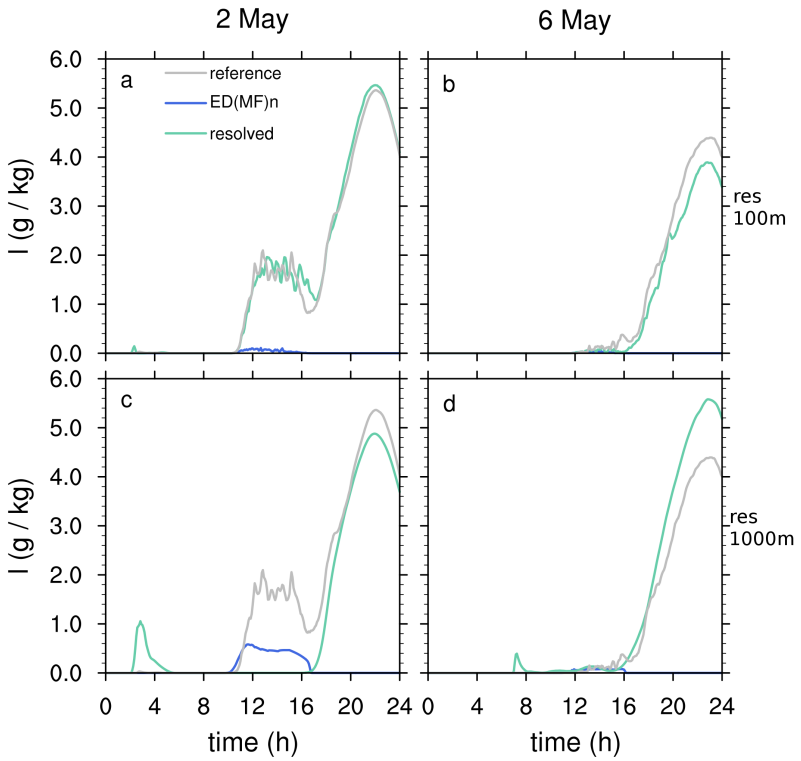

Figure 5.12: Time series of integrated liquid water mixing ratio for the two shallow cumulus days from the reference simulation (gray) and the simulations with resolutions of 100 m (top) and 1000 m (bottom), showing the resolved contribution (green) and the contribution by ED(MF)^n (blue).

trast to the results from the RICO case in the previous chapter and shows that the diurnal cycle is a much more challenging case. Also, for May 6 at 1000 m, ED(MF)^n seems not to contribute anything to cloudiness (not shown), maybe because the plumes at this time do not reach high enough. This causes the resolved scales from the LES to start overturning the existing instability, resulting in too much cloudiness with unrealistic spikes in the profile. The reason for this behavior could be that on both May 2 and May 6 for the resolution of 1000 m the ED(MF)^n deepens too quickly in the period between sunrise and convective cloud onset. As a result, too much instability is removed too quickly, by which the ED(MF)^n convection collapses somewhat in the second part of the day. Preventing this rapid deepening in the early hours should mend this problem.

A closer look into the distribution between resolved and parameterized humidity transport is given in Figure 5.15. Here, the contribution of the subgrid transport to the total transport is given at different times and different heights, for all three days. Before sunrise (Fig. 5.15a), no convection is active and no transport is done by ED(MF)^n, here shown at a height of 500 m. In the middle of the day, when convection is active, a distribution at 500 m is seen for all three days of little transport by ED(MF)^n for fine resolutions, all transport done by ED(MF)^n for coarse resolutions, and a transition in between in the area

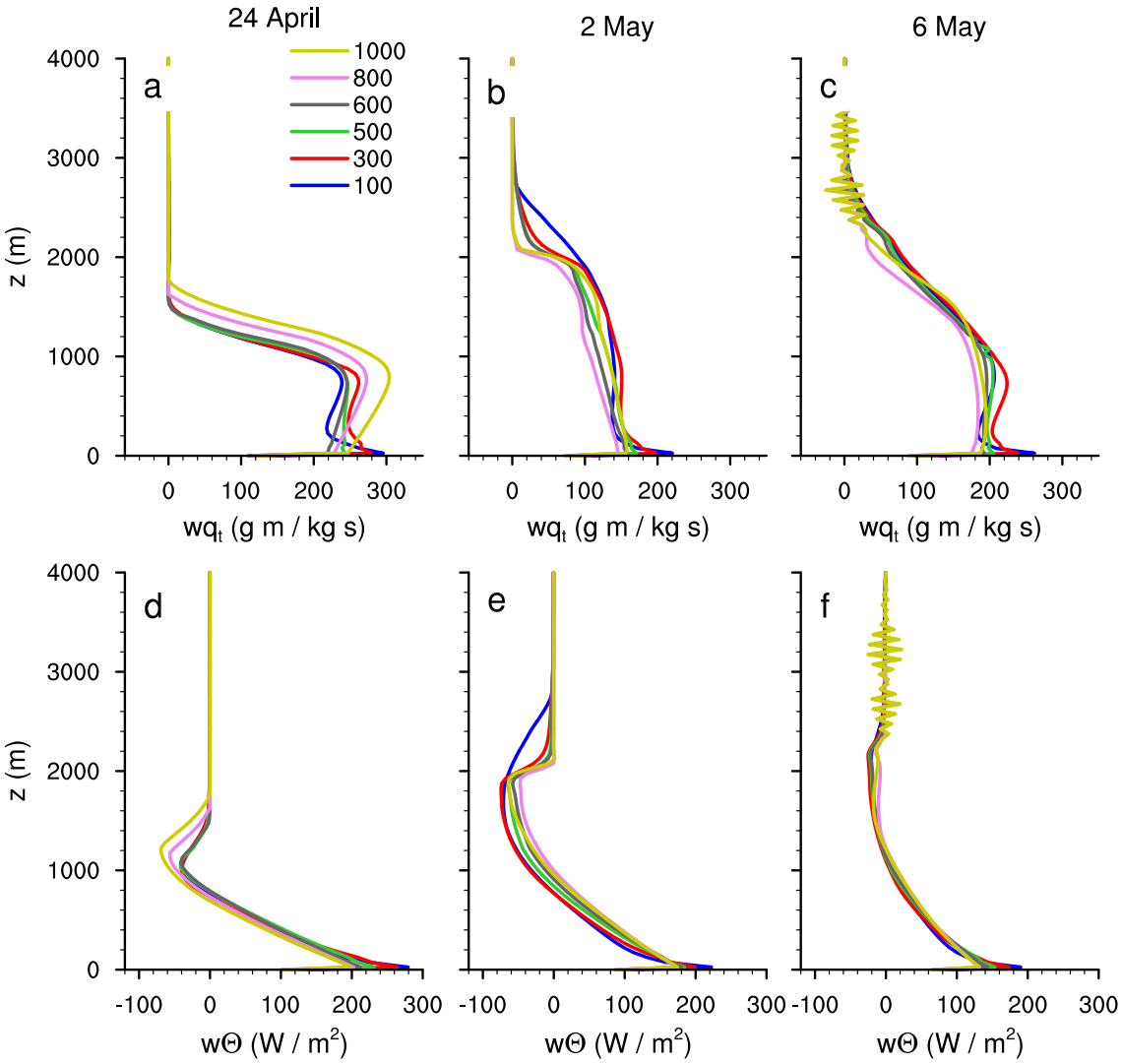

Figure 5.13: Profiles of total vertical transport of q_t (a,b,c) and Θ (d,e,f), averaged horizontally and over five hours (11 - 16 UTC), for different resolutions (in colors) for the three days.

of the gray zone (Fig. 5.15b, also shown in Fig. 4.8 for the RICO case). This distribution matches the classic S-shape that we expect in the gray zone of shallow convection [HONNERT ET AL., 2016; DORRESTIJN ET AL., 2013]. After sunset at 500 m (Fig. 5.15e) ED(MF)^n is still active with its ED component contributing significantly to transport, but the total transport is very small at this time of night, and convection is not active anymore. Therefore, we do not expect a prototype distribution between the different resolutions. Figure 5.15c-d shows the distribution of the transport for different heights at a time where convection is active. The prototype distribution at 500 m (Fig. 5.15b) lies in the middle of the mixed layer, while Figure 5.15c shows the distribution in the middle of the cloud layer at 1500 m. Here, the transition between resolved and parameterized scales is also S-shaped for May 2 and May 6, while for the dry day of April 24 the transition is discrete

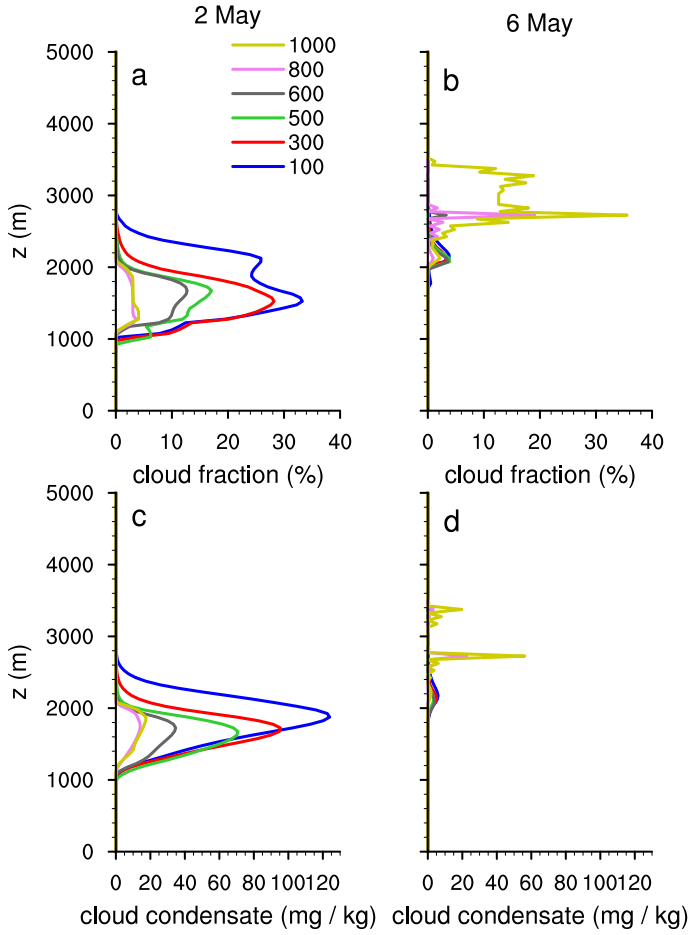

Figure 5.14: Horizontally averaged profiles of (a,b) total cloud fraction (average of 12 and 14 UTC) and (c,d) total cloud condensate (averaged over 12 - 14 UTC), for different resolutions (in colors) for two days.

at 800 - 900 m resolution. This is because in the simulations with resolutions below 900 m the inversion is below this level of 1500 m, while for resolutions of 900 m and 1000 m the level of 1500 m lies within the inversion, apparently because the plumes reach a bit higher at 900 m and 1000 m resolution. The reason that the plumes reach higher is because the entrainment of the plumes is assumed to be dependent on plume size, allowing the plumes for the coarse resolutions to penetrate slightly deeper. Figure 5.15d shows a height of 2800 m, which lies above the cloud layer. Here, only a small amount of transport is done by ED(MF)^n for small to middle resolutions, either due to the ED-component of ED(MF)^n or because there is still a small number of plumes reaching this height. However, since this layer lies above the cloud layer, the small amount of transport done by ED(MF)^n is in accordance with our expectations.

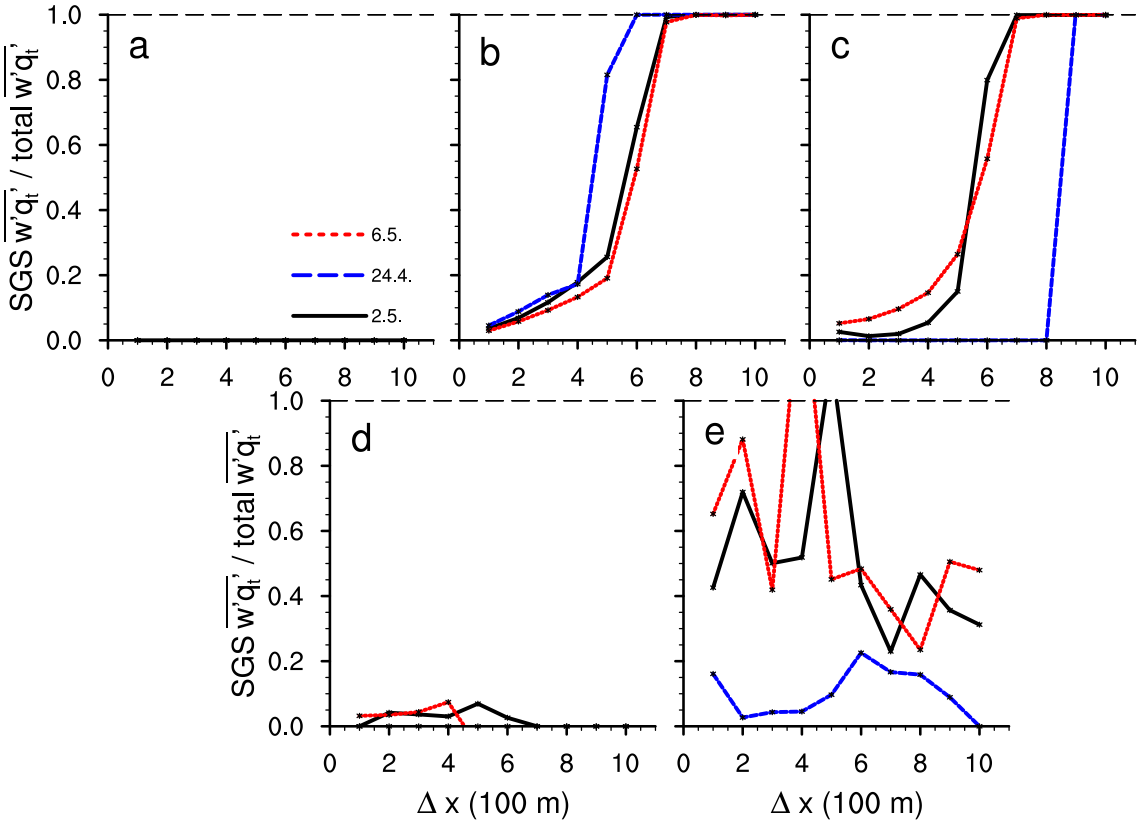

Figure 5.15: Ratio between subgrid and total flux of q_t, averaged horizontally, for the three days, (a) at height 500 m averaged between 4-5 UTC, (b) at height 500 m between 12-13 UTC, (c) at height 1500 m between 12-13 UTC, (d) at height 2800 m between 12-13 UTC, (e) at height 500 m between 21-22 UTC.

5.4 Summary and Conclusion

This chapter studies the behavior of ED(MF)^n for more complex cases of shallow cumuli over land and with a diurnal cycle. In the first part of this chapter, it was shown that our setup with the forcing provided by COSMO is able to reproduce the vertical structure and time-development of the transport and the thermodynamic state of the transient boundary layer over land. Three days where chosen, with two of the days featuring shallow cumulus clouds. These days differ mostly in the time when convection starts and the height up to which the convection reaches. As a third day a dry case was chosen to study the behavior of ED(MF)^n in a limit case.

To study the scale-adaptivity of ED(MF)^n, it is implemented into an LES model as a subgrid scheme. Then, LES is run with different resolutions. This analysis showed that ED(MF)^n is scale-adaptive even in these more complex cases of continuing transition during the day, since the key behavior in the gray zone established for the easy RICO case is also reproduced. In particular the flux partitioning is reproduced. For fine resolutions, the

transport is mostly done by the LES, which resolves the clouds. For coarser resolutions, ED(MF)^n takes over the transport and represents the clouds. This conclusion holds for all three days, i. e., for the two shallow cumulus days as well as for the dry day. However, some shortcomings in the development of the clouds are established, which are traced back to the partitioning between the parameterized and the resolved convection in the early hours after the morning transition. Future work on ED(MF)^n is underway to resolve these issues and to improve the parameterization scheme.

6 Conclusion and Outlook

Due to the small scales associated with shallow cumulus clouds their impact on the atmospheric state and larger scale flow is usually represented in weather and climate models by means of parameterization. Presently the spatial and temporal discretizations of numerical weather prediction models are getting to the point where some of the shallow cumulus clouds can be resolved. Parameterization schemes in such models should react to this development by only representing those clouds that are not resolved by the large-scale model, thus becoming scale-aware and scale-adaptive. This thesis contributes to exploring scale-adaptive parameterization schemes.

Chapter 3 investigates the behavior of parcels rising in a heterogeneous environment containing cumulus clouds by means of the classic rising parcel model. The parcels are given vertical profiles of the atmospheric state at multiple grid points inside an LES of a shallow cumulus cloud field to provide a range of different environments. During their ascent, the parcels interact with the turbulent heterogeneous environment in which they rise. For the same setup, different entrainment formulations, which are based on a variety of variables and calibrated to allow a comparison, are used to study their impact on the fate of the rising parcels. It was found that the most important factor determining the behavior of the parcel is the local environment in which they rise. When rising in a buoyant, humid environment inside an LES cloud, the parcels reach much greater heights compared to the situation when they rise inside an unfavorable environment. As soon as a parcel leaves the protective environment inside a cloud, it soon reaches its termination height. Thus, in the kinetic energy budget of the parcels, the impact of the direct environment (through the mixing term) dominates over the buoyancy acceleration term.

A simple setup was adopted in this study in order to study the potential first order effects of a heterogeneous environment on rising parcels. This approach was indeed successful in providing valuable insights; however, some key simplifications were applied that probably affect the results, and therefore could be treated in a more sophisticated way, e. g., the life cycle of clouds was neglected, as well as vertical shear of the clouds. To study the impact of the limitations of this study, trajectories of rising parcels could be followed within an LES. The effect of the local environment could be included, e. g., by including stochastic effects into the entrainment formulation or to allow rising parcels to directly interact with each other.

In chapter 4 and 5 the analysis progresses from the off-line, diagnostic study of a single component of a parameterization scheme (i. e. the rising parcel model) to studying a complete parameterization scheme in a prognostic setting in which it is interactive with the larger-scale model. This means that two-way interaction exists between the parameterized process and the larger-scale flow. The focus in these chapters lies on the scale-adaptivity of the scheme. A key novelty is that the LES is used as a simple circulation model to this purpose. A new parameterization scheme for boundary layer transport and clouds, ED(MF)^n, which is a bin-macrophysics scheme, was implemented into an LES, replacing the original subgrid scheme. The LES was then run with resolutions ranging from 100 m to 1 km to test the scale-adaptivity of the scheme. The scheme consists of multiple plumes, each representing a class of plumes of a certain size. Scale-adaptivity is included by excluding those plumes larger than the grid size from contributing to transport in the SGS budget. This reflects the basic assumption that the plumes larger than a certain cut-off length are resolved by the LES. By implementing ED(MF)^n into LES, the scheme can be studied in an environment which is simpler than operational weather prediction models, so that the processes determining the behavior of the scheme can be better understood without its behavior being obscured by, e. g., other parameterization schemes.

The behavior of this scale-adaptive framework was studied using a simple marine case of shallow cumulus clouds. A motivation for choosing this cumulus case was that it is idealized and reaches a quasi-stationary state, making it a good starting point to study the principal scale-adaptivity of the parameterization scheme. With this setup, it was shown that the size-filtered ED(MF)^n framework is indeed scale-adaptive. This behavior is apparent in the range of spatial resolutions that covers the gray zone of shallow convection. Toward finer resolutions, almost all vertical transport was resolved, while toward coarse resolutions ED(MF)^n conducted almost all of the transport. In between, a smooth transition in the partitioning between subgrid-scale and resolved transport occurred in the gray zone. Most of the scale-adaptivity was carried by the mass flux part of the scheme, where plumes larger than the grid size are filtered out. However, it proved necessary to include scale-adaptivity in the eddy diffusivity part of the scheme as well, in order to avoid overestimating the subgrid-scale transport for fine resolutions.

In chapter 5 the behavior of the new scheme is studied in a more complex setting, by means of simulations for a set of selected diurnal cycles over land. Three cases are constructed that reflect three days of the measurement campaign HOPE. Analyses of the operational weather prediction model COSMO-DE were used to force the LES. Time-dependent advective forcing in combination with continuous Newtonian relaxation was applied during the simulation to achieve a good representation of the observed conditions in the atmosphere. First a control run with the LES without ED(MF)^n was evaluated with the measurements from HOPE, which described the thermodynamic state, the vertical structure,

and clouds, using state of the art instrumentation and including both in-situ and remote sensing. It was found that LES satisfactorily reproduces the observed vertical structure and the time development of the transient boundary layer. Next, similar to the previous analysis for the marine steady-state cumulus case, the scale-adaptivity of the ED(MF)^n scheme was tested by running the LES with varying resolutions. In this setup, the key behavior of ED(MF)^n as shown for the RICO case could be reproduced, demonstrating basic scale-adaptivity also for the more complex transient cases. While these results on the subgrid-resolved flux partitioning are encouraging, challenging situations were also identified. For example, sometimes complex cloud situations featuring decoupled stratiform layers were not well reproduced. Also the flux partitioning during the morning transition proved to be difficult.

Within this work the parameterization scheme ED(MF)^n demonstrates scale-adaptivity even for more complex cases. ED(MF)^n should be considered a first basic framework for representing scale-adaptivity in convective transport of advective nature. While the results illustrate that this setup successfully captures the first-order size-dependencies in transport, arguably it still has its conceptual limitations. One simplification in the scheme is the assumption of a constant updraft fraction. Improvements to the scheme could include a variable updraft fraction, as well as including stochastic effects. Also, the performance of ED(MF)^n during fast transition situations could be improved. In ED(MF)^n as used here, the cloud size distribution was assumed to follow a power law without scale-break. Using, e. g., satellite data to further investigate cloud size distributions of shallow cumulus cloud fields with a resolution fine enough to also capture the smallest cumulus clouds could improve the representation of this distribution in ED(MF)^n by prescribing a more sophisticated distribution. Further work could also include an evaluation of the fluxes calculated by the model with measured fluxes. For this comparison, measurements of fluxes as a function of size would be useful. Also, entrainment measurements of clouds of different sizes could be helpful to evaluate the entrainment rate of the model.

This work showed that parameterization schemes of shallow cumulus convection in numerical weather prediction models approaching resolutions close to the gray zone of convection should include scale-adaptivity. Without it, the contribution of the fluxes by the parameterization scheme can be grossly overestimated for resolutions smaller than the gray zone. Implementing a scale-adaptive parameterization scheme such as ED(MF)^n into numerical weather prediction models could therefore be beneficial for the quality of weather forecasts.

List of Symbols

Abbreviations

ARM	- Atmospheric Radiation Measurement Program
ASTER	- Advanced Spaceborne Thermal Emission and Reflection Radiometer
ATEX	- Atlantic Trade Wind Experiment
BLH	- Boundary Layer Height
BOMEX	- Barbados Oceanographic and Meteorological Experiment
CRM	- Cloud Resolving Models
DNS	- Direct Numerical Simulation
ECMWF	- European Centre for Medium-Range Weather Forecasts
EDMF	- Eddy Diffusivity Mass Flux
ED(MF)^n	- Eddy Diffusivity Multiple Mass Flux
GDEM	- Global Digital Elevation Model
HD(CP)2	- High Definition Clouds and Precipitation for advancing Climate Prediction
HOPE	- HD(CP)2 Observational Prototype Experiment
ICON	- Icosahedral Non-Hydrostatic Model
IFS	- Integrated Forecasting System
IWV	- Integrated Water Vapor
JOYCE	- Jülich ObservatorY for Cloud Evolution
KITcube	- Karlsruhe Institute for Technology mobile facility
LACROS	- Leipzig Aerosol and Cloud Remote Observations System
LCL	- Lifting Condensation Level
LES	- Large-Eddy Simulation
LWP	- Liquid Water Path
RANS	- Reynolds Averaged Navier-Stokes Simulation
RICO	- Rain in Cumulus over the Ocean
RMSE	- Root Mean Square Error
SCM	- Single Column Model
SGS	- Subgrid Scale
UCLALES	- University of California, Los Angeles, LES

Variables

a	- area fraction
$\mathscr{A}, \mathscr{M}, \mathscr{N}$	- properties dependent on plume size
B	- buoyancy
β	- parameter controlling the speed of transition
c_p	- specific heat capacity for ideal gas at constant pressure
c_{pd}	- specific heat of dry air at constant pressure
C_S	- Smagorinsky constant
D_{ij}	- resolved deformation
δ_{ij}	- Kronecker delta
e	- turbulent kinetic energy
E	- energy
ε	- fractional entrainment rate
ε_{ijk}	- Levi-Civity symbol
η	- calibration factor
f	- Coriolis parameter
F	- filter size
Φ	- conserved thermodynamic variable for moist adiabatic ascent
Φ_{h0}, Φ_{m0}	- stability functions
$\Delta\Phi$	- surface perturbation
g	- gravity acceleration
G	- convolution kernel
Γ	- Gamma function
θ	- scale parameter
Θ	- potential temperature
Θ_l	- liquid water potential temperature
Θ_v	- virtual potential temperature
I	- indicator function
K_m, K_h	- subgrid scale eddy diffusivity coefficients for momentum and heat
κ	- von Kármán constant
l	- length scale
l_{SGS}	- subgrid scale mixing length
L	- Obukhov length
L_v	- latent heat of vaporization
λ, α, c, c_s	- various constants
M	- mass flux
μ, b	- proportionality constants for drag and mixing
ν_m, ν_h p	- pressure

p_{1000}	- reference pressure at 1000 hPa
Pr	- Prandtl number
q	- water vapor mixing ratio
q_l	- liquid water mixing ratio
q_t	- total water mixing ratio
R	- cloud radius
R_g	- gas constant
Ri	- Richardson number
ρ	- density
S_h	- source term for heat
Δs	- grid scale
σ	- standard deviation
t	- time
T	- temperature
τ	- turnover scale
τ_{ij}, γ_k	- subgrid fluxes of momentum and heat
u_i	- three velocity components
u_*	- friction velocity
u, v	- horizontal wind velocities
V_{BL}	- wind in the boundary layer
V_g	- geostrophic wind
w	- vertical wind velocity
W	- weighing function
x_i	- Cartesian coordinates x, y, z
Δx	- horizontal grid spacing
z	- height
z_i	- boundary layer height
Δz	- vertical grid spacing
ζ	- dissipation rate

Indices

l	- index of the updraft number
e	- environment
c	- cloud
u	- updraft
0	- ground state
$*$	- deviation of ground state
b	- mean over parcels in bin

$\bar{x}$	- horizontal average over x
Lc	- LES-column
m	- momentum
h	- heat

Bibliography

Ackerman, T. P. and G. M. Stokes, 2003: The atmospheric radiation measurement program. *Phys. Today*, **56**, 38–44, doi:10.1063/1.1554135.

Arakawa, A., 1975: General circulation of the atmosphere. *Rev. Geophys.*, **13**, 668–680, doi:10.1029/RG013i003p00668.

Arakawa, A., 2004: The cumulus parameterization problem: Past, present, and future. *J. Climate*, **17**, 2493–2525, doi:http://dx.doi.org/10.1175/1520-0442(2004)017<2493:RATCPP>2.0.CO;2.

Arakawa, A. and W. H. Schubert, 1974: Interaction of a cumulus cloud ensemble with the large-scale environment, part I. *J. Atmos. Sci.*, **31**, 674–701, doi:http://dx.doi.org/10.1175/1520-0469(1974)031<0674:IOACCE>2.0.CO;2.

Arakawa, A. and C. Wu, 2013: A unified representation of deep moist convection in numerical modeling of the atmosphere. Part I. *J. Atmos. Sci.*, **70**, 1977–1992, doi:10.1175/JAS-D-12-0330.1.

ASTER GDEM Validation Team, 2011: ASTER global digital elevation model version 2 - summary of validation results, Tech. rep., NASA Land Processes Distributed Active Archive Center (LP DAAC), USGS/Earth Resources Observation and Science (EROS) Center, Sioux Falls, South Dakota, USA, accessed on May 4, 2017. http://www.jspacesystems.or.jp/ersdac/GDEM/ver2Validation/Summary_GDEM2_validation_report_final.pdf.

Augstein, E., H. Riehl, F. Ostapoff, and V. Wagner, 1973: Mass and energy transports in an undisturbed atlantic trade-wind flow. *Mon. Wea. Rev.*, **101**, 101–111, doi:10.1175/1520-0493(1973)101<0101:MAETIA>2.3.CO;2.

Avissar, R. and T. Schmidt, 1998: An evaluation of the scale at which ground–surface heat flux patchiness affects the convective boundary layer using large–eddy simulations. *J. Atmos. Sci.*, **55**, 2666–2689, doi:10.1175/1520-0469(1998)055<2666:AEOTSA>2.0.CO;2.

Baldauf, M., A. Seifert, J. Förstner, D. Majewski, and M. Raschendorfer, 2011: Operational

convective-scale numerical weather prediction with the cosmo model: Description and sensitivities. *Mon. Wea. Rev.*, **139**, 3887–3905, doi:10.1175/MWR-D-10-05013.1.

Beare, R. J., et al., 2006: An intercomparison of large-eddy simulations of the stable boundary layer. *Boundary-Layer Meteorol.*, **118**, 247–272, doi:10.1007/s10546-004-2820-6.

Benner, T. C. and J. A. Curry, 1998: Characteristics of small tropical cumulus clouds and their impact on the environment. *J. Geophys. Res.*, **103**, 28 753–28 767, doi:10.1029/98JD02579.

Betts, A. K., 1973: Non-precipitating cumulus convection and its parameterization. *Q. J. R. Meteorol. Soc.*, **99**, 178–196, doi:10.1002/qj.49709941915.

Bogenschutz, P. A. and S. K. Krueger, 2013: A simplified PDF parameterization of subgrid-scale clouds and turbulence for cloud-resolving models. *J. Adv. Model. Earth Syst.*, **5**, 195–211, doi:10.1002/jame.20018.

Böing, S. J., H. J. J. Jonker, A. P. Siebesma, and W. W. Grabowski, 2012: Influence of the subcloud layer on the development of a deep convective ensemble. *J. Atmos. Sci.*, **69**, 2682–2698, doi:10.1175/JAS-D-11-0317.1.

Bony, S., et al., 2006: How well do we understand and evaluate climate change feedback processes? *J. Climate*, **19**, 3445–3482, doi:10.1175/JCLI3819.1.

Boucher, O., et al., 2013: Clouds and aerosols. In: IPCC Climate Change 2013: The physical science basis. Contribution of working group I to the fifth assessment report of the intergovernmental panel on climate change. Cambridge University Press, Cambridge, United Kingdom and New York, NY, USA, chapter 7.

Boutle, I. A., J. E. J. Eyre, and A. P. Lock, 2014: Seamless stratocumulus simulation across the turbulent gray zone. *Mon. Wea. Rev.*, **142**, 1655–1668, doi:http://dx.doi.org/10.1175/MWR-D-13-00229.1.

Bretheron, C. S., J. R. McCaa, and H. Grenier, 2004: A new parameterization for shallow cumulus convection and its application to marine subtropical cloud-topped boundary layers. Part I: Description and 1D results. *Mon. Wea. Rev.*, **132**, 864–882, doi:http://dx.doi.org/10.1175/1520-0493(2004)132<0864:ANPFSC>2.0.CO;2.

Brown, A. R., et al., 2002: Large-eddy simulation of the diurnal cycle of shallow cumulus convection over land. *Q. J. R. Meteorol. Soc.*, **128**, 1075–1093, doi:10.1256/003590002320373210.

Calhoun, R., F. Gouveia, J. Shinn, S. Chan, D. Stevens, R. Lee, and J. Leone, 2005: Flow

around a complex building: Experimental and large-eddy simulation comparisons. *J. Appl. Meteor.*, **44**, 571–590, doi:10.1175/JAM2219.1.

Cheinet, S., 2003: A multiple mass-flux parameterization for the surface-generated convection. *J. Atmos. Sci.*, **60**, 2313–2327, doi:http://dx.doi.org/10.1175/1520-0469(2003)060<2313:AMMPFT>2.0.CO;2.

Chikira, M. and M. Sugiyama, 2010: Cumulus parameterization with state-dependent entrainment rate. Part I: Description and sensitivity to temperature and humidity profiles. *J. Atmos. Sci.*, **67**, 2171–2193, doi:10.1175/2010JAS3316.1.

Chlond, A., 1992: Three-dimensional simulation of cloud street development during a cold air outbreak. *Boundary-Layer Meteorol.*, **58**, 161–200, doi:10.1007/BF00120757.

Chlond, A. and A. Wolkau, 2000: Large-eddy simulation of a nocturnal stratocumulus-topped marine atmospheric boundary layer: An uncertainty analysis. *Boundary-Layer Meteorol.*, **95**, 31–55, doi:10.1023/A:1002438701638.

Dawe, J. T. and P. H. Austin, 2012: Statistical analysis of an LES shallow cumulus cloud ensemble using a cloud tracking algorithm. *Atmos. Chem. Phys.*, **12**, 1101–1119, doi:10.5194/acp-12-1101-2012.

Dawe, J. T. and P. H. Austin, 2013: Direct entrainment and detrainment rate distributions of individual shallow cumulus clouds in an LES. *Atmos. Chem. Phys.*, **13**, 7795–7811, doi:10.5194/acp-13-7795-2013.

De Roode, S. R., P. G. Duynkerke, and H. J. J. Jonker, 2004: Large-eddy simulation: How large is large enough? *J. Atmos. Sci.*, **61**, 403–421, doi:10.1175/1520-0469(2004)061<0403:LSHLIL>2.0.CO;2.

De Roode, S. R., A. P. Siebesma, H. J. J. Jonker, and Y. D. Voogd, 2012: Parameterization of the vertical velocity equation for shallow cumulus clouds. *Mon. Wea. Rev.*, **140**, 2424–2436, doi:10.1175/MWR-D-11-00277.1.

De Rooy, W. C. and A. P. Siebesma, 2008: A simple parameterization for detrainment in shallow cumulus. *Mon. Wea. Rev.*, **136**, 560–576, doi:10.1175/2007MWR2201.1.

De Rooy, W. C. and A. P. Siebesma, 2010: Analytical expressions for entrainment and detrainment in cumulus convection. *Q. J. R. Meteorol. Soc.*, **136**, 1216–1227, doi:10.1002/qj.640.

De Rooy, W. C., et al., 2013: Entrainment and detrainment in cumulus convection: an overview. *Q. J. R. Meteorol. Soc.*, **139**, 1–19, doi:10.1002/qj.1959.

Deardorff, J. W., 1980: Stratocumulus–capped mixed layers derived from a three–dimensional model. *Boundary–Layer Meteorology*, **18**, 495–527.

Dorrestijn, J., D. T. Crommelin, A. P. Siebesma, and H. J. J. Jonker, 2013: Stochastic parameterization of shallow cumulus convection estimated from high-resolution model data. *Theor. Comput. Fluid Dyn.*, **27**, 133–148, doi:10.1007/s00162-012-0281-y.

Dufresne, J.-L. and S. Bony, 2008: An assessment of the primary sources of spread of global warming estimates from coupled atmosphere-ocean models. *J. Climate*, **21**, 5135–5144, doi:10.1175/2008JCLI2239.1.

Etling, D., 2008: *Theoretische Meteorologie*. 3d ed., Springer, Berlin Heidelberg New York.

European Centre for Medium-Range Weather Forecasts, 2014: IFS Documentation, Cy40r1. Part IV: physical processes.

Fritsch, J. M. and C. F. Chappell, 1980: Numerical prediction of convectively driven mesoscale pressure systems. part I: Convective parameterization. *J. Atmos. Sci.*, **37**, 1722–1733, doi:http://dx.doi.org/10.1175/1520-0469(1980)037<1734:NPOCDM>2.0.CO;2.

Gerard, L., 2015: Bulk mass-flux perturbation formulation for a unified approach of deep convection at high resolution. *Mon. Wea. Rev.*, **143**, 4038–4063, doi:10.1175/MWR-D-15-0030.1.

Grabowski, W. W., 2016: Towards global large eddy simulation: Super-parameterization revisited. *J. Meteor. Soc. Japan*, **94**, 327–344, doi:10.2151/jmsj.2016-017.

Grant, A. L. M., 2001: Cloud-base fluxes in the cumulus-capped boundary layer. *Q. J. R. Meteorol. Soc*, **127**, 407–421, doi:10.1002/qj.49712757209.

Gregory, D., 2001: Estimation of entrainment rate in simple models of convective clouds. *Q. J. R. Meteorol. Soc.*, **127**, 53–72, doi:10.1002/qj.49712757104.

Gryschka, M. and S. Raasch, 2005: Roll convection during a cold air outbreak: A large eddy simulation with stationary model domain. *Geophys. Res. Lett.*, **32**.

Heinze, R., C. Moseley, L. N. Böske, S. Muppa, V. Maurer, S. Raasch, and B. Stevens, 2016: Evaluation of large-eddy simulations forced with mesoscale model output for a multi-week period during a measurement campaign. *Atmos. Chem. Phys. Discuss.*, doi:10.5194/acp-2016-498, in review.

Heus, T., H. J. J. Jonker, H. E. A. V. den Akker, E. J. Griffith, M. Koutek, and F. H. Post, 2009: A statistical approach to the life cycle analysis of cumulus clouds selected in a virtual reality environment. *J. Geophys. Res.*, **114**, doi:10.1029/2008JD010917.

Heus, T., G. van Dijk, H. J. Jonker, and H. A. V. den Akker, 2008: Mixing in shallow cumulus clouds studied by lagrangian particle tracking. *J. Atmos. Sci.*, **65**, 2581–2597, doi:10.1175/2008JAS2572.1.

Heus, T., et al., 2010: Formulation of the Dutch Atmospheric Large-Eddy Simulation (DALES) and overview of its applications. *Geosci. Model Dev.*, **3**, 415–444, doi: 10.5194/gmd-3-415-2010.

Hohenegger, C. and C. S. Bretherton, 2011: Simulating deep convection with a shallow convection scheme. *Atmos. Chem. Phys.*, **11**, 10 389–10 406, doi:10.5194/acp-11-10389-2011.

Holland, J. Z. and E. M. . Rasmusson, 1973: Measurements of the atmospheric mass, energy, and momentum budgets over a 500-kilometer square of tropical ocean. *Mon. Wea. Rev.*, **101**, 44–55, doi:10.1175/1520-0493(1973)101<0044:MOTAME>2.3.CO;2.

Holtslag, A. A. M. and C.-H. Moeng, 1991: Eddy diffusivity and countergradient transport in the convective atmospheric boundary layer. *J. Atmos. Sci.*, **48**, 1690–1698, doi:10.1175/1520-0469(1991)048<1690:EDACTI>2.0.CO;2.

Honnert, R., F. Couvreux, V. Masson, and D. Lancz, 2016: Sampling the structure of convective turbulence and implications for grey-zone parametrizations. *Boundary-Layer Meteorol.*, **160**, 133–156, doi:10.1007/s10546-016-0130-4.

Honnert, R., V. Masson, and F. Couvreux, 2011: A diagnostic for evaluating the representation of turbulence in atmospheric models at the kilometric scale. *J. Atmos. Sci.*, **68**, 3112–3131, doi:10.1175/JAS-D-11-061.1.

Illingworth, A. J., et al., 2007: CLOUDNET - Continuous evaluation of cloud profiles in seven operational models using ground-based observations. *Bull. Amer. Meteor. Soc.*, **88**, 883–898, doi:10.1175/BAMS-88-6-883.

Ito, J., H. Niino, and M. Nakanishi, 2013: Formation mechanism of dust devil–like vortices in idealized convective mixed layers. *J. Atmos. Sci.*, **70**, 1173–1186, doi: 10.1175/JAS-D-12-085.1.

Jensen, M. P. and A. D. D. Genio, 2006: Factors limiting convective cloud-top height at the ARM Nauru Island Climate Research Facility. *J. Climate*, **19**, 2105–2117, doi: http://dx.doi.org/10.1175/JCLI3722.1.

Jonas, P. R., 1990: Observations of cumulus cloud entrainment. *Atmos. Res.*, **25**, 105–127, doi:10.1016/0169-8095(90)90008-Z.

Kain, J. S. and J. M. Fritsch, 1990: A one-dimensional entraining / detraining plume model and its application in convective parameterization. *J. Atmos. Sci.*, **47**, 2784–2802, doi: http://dx.doi.org/10.1175/1520-0469(1990)047<2784:AODEPM>2.0.CO;2.

Kalthoff, N., et al., 2014: KITcube - a mobile observation platform for convection studies

deployed during HyMeX. *Meteorol. Z.*, **22**, 633–647, doi:10.1127/0941-2948/2013/0542.

Kanak, K. M., D. K. Lilly, and J. T. Snow, 2000: The formation of vertical vortices in the convective boundary layer. *Q. J. R. Meteorol. Soc.*, **126**, 2789–2810, doi:10.1002/qj.49712656910.

Kanani-Sühring, F. and S. Raasch, 2015: Spatial variability of scalar concentrations and fluxes downstream of a clearing-to-forest transition: A large-eddy simulation study. *Boundary-Layer Meteorol.*, **155**, 1–27, doi:10.1007/s10546-014-9986-3.

Keane, R., G. Craig, C. Keil, and G. Zängl, 2014: The Plant-Craig stochastic convection scheme in ICON and its scale adaptivity. *J. Atmos. Sci.*, **71**, 3404–3415, doi:10.1175/JAS-D-13-0331.1.

Lappen, C. and D. Randall, 2001: Toward a unified parameterization of the boundary layer and moist convection. Part I: A new type of mass-flux model. *J. Atmos. Sci.*, **58**, 2021–2036, doi:10.1175/1520-0469(2001)058<2021:TAUPOT>2.0.CO;2.

Letzel, M. O., C. Helmke, E. Ng, X. An, A. Lai, and S. Raasch, 2012: LES case study on pedestrian level ventilation in two neighbourhoods in Hong Kong. *Meteorol. Z.*, **6**, 575–589, doi:10.1127/0941-2948/2012/0356.

Lin, C., 1999: Some bulk properties of cumulus ensembles simulated by a cloud-resolving model. Part II: Entrainment profiles. *J. Atmos. Sci.*, **56**, 3736–3748, doi:http://dx.doi.org/10.1175/1520-0469(1999)056<3736:SBPOCE>2.0.CO;2.

Löhnert, U., et al., 2015: JOYCE - Jülich Observatory for Cloud Evolution. *Bull. Amer. Meteor. Soc.*, **96**, 1157–1174, doi:10.1175/BAMS-D-14-00105.1.

López, R., 1977: The lognormal distribution and cumulus cloud populations. *Mon. Wea. Rev.*, **105**, 865–872, doi:10.1175/1520-0493(1977)105<0865:TLDACC>2.0.CO;2.

Macke, A., et al., 2017: The HD(CP)2 Observational Prototype Experiment HOPE - an overview. *Atmos. Chem. Phys.*, **17**, 4887–4914, doi:10.5194/acp-17-4887-2017.

Manabe, S., J. Smagorinsky, and R. F. Strickler, 1965: Simulated climatology of a general circulation model with a hydrologic cycle. *Mon. Wea. Rev.*, **93**, 769–798, doi:10.1175/1520-0493(1965)093<0769:SCOAGC>2.3.CO;2.

Maronga, B. and S. Raasch, 2013: Large–eddy simulations of surface heterogeneity effects on the convective boundary layer during the LITFASS-2003 experiment. *Boundary-Layer Meteorol.*, **146**, 17–44, doi:10.1007/s10546-012-9748-z.

Marsaglia, G. and T. A. Bray, 1964: A convenient method for generating normal variables. *SIAM Review*, **6**, 260–264.

Marsaglia, G. and W. W. Tsang, 2000: A simple method for generating gamma variables. *ACM Transactions on Mathematical Software*, **26**, 363–372, doi:10.1145/358407.358414.

Mason, P. J., 1989: Large-eddy simulation of the convective atmospheric boundary layer. *J. Atmos. Sci.*, **46**, 1492–1516, doi:10.1175/1520-0469(1989)046<1492:LESOTC>2.0.CO;2.

Nebenführ, B. and L. Davidson, 2015: Large-eddy simulation study of thermally stratified canopy flow. *Boundary-Layer Meteorol.*, **156**, 253–276, doi:007/s10546-015-0025-9.

Neggers, R., H. Jonker, and A. Siebesma, 2003: Size statistics of cumulus cloud populations in large-eddy simulations. *J. Atmos. Sci.*, **60**, 1060–1074, doi:10.1175/1520-0469(2003)60<1060:SSOCCP>2.0.CO;2.

Neggers, R. A. J., 2009: A dual mass flux framework for boundary layer convection. part II: Clouds. *J. Atmos. Sci.*, **66**, 1489–1506.

Neggers, R. A. J., 2015: Exploring bin-macrophysics models for moist convective transport and clouds. *J. Adv. Model. Earth Syst.*, **7**, 2079–2104, doi:10.1002/2015MS000502.

Neggers, R. A. J., M. Köhler, and A. C. M. Beljaars, 2009: A dual mass flux framework for boundary layer convection. part I: Transport. *J. Atmos. Sci.*, **66**, 1465–1487, doi:http://dx.doi.org/10.1175/2008JAS2635.1.

Neggers, R. A. J., J. D. Neelin, and B. Stevens, 2007: Impact mechanisms of shallow cumulus convection on tropical climate dynamics. *J. Climate*, **20**, 2623–2642, doi:http://dx.doi.org/10.1175/JCLI4079.1.

Neggers, R. A. J., A. P. Siebesma, and H. J. J. Jonker, 2002: A multiparcel model for shallow cumulus convection. *J. Atmos. Sci.*, **59**, 1655–1668, doi:http://dx.doi.org/10.1175/1520-0469(2002)059<1655:AMMFSC>2.0.CO;2.

Neggers, R. J., A. P. Siebesma, and T. T. Heus, 2012: Continuous single-column model evaluation at a permanent meteorological supersite. *Bull. Amer. Meteor. Soc.*, **93**, 1389–1400, doi:10.1175/BAMS-D-11-00162.1.

Nieuwstadt, F. T. M., P. J. Mason, C.-H. Moeng, and U. Schumann, 1993: *Large-Eddy Simulation of the Convective Boundary Layer: A Comparison of Four Computer Codes*, chap. 4, 343–367. Springer Berlin Heidelberg, Berlin, Heidelberg, doi:10.1007/978-3-642-77674-8_24.

Ooyama, K., 1971: A theory on parameterization of cumulus convection. *J. Meteor. Soc. Japan*, **49**, 744–756, special Issue.

Park, S., 2014a: A unified convection scheme (UNICON). Part I: Formulation. *J. Atmos. Sci.*, **71**, 3902–3930, doi:10.1175/JAS-D-13-0233.1.

Park, S., 2014b: A unified convection scheme (UNICON). Part II: Simulation. *J. Atmos. Sci.*, **71**, 3931–3973, doi:10.1175/JAS-D-13-0234.1.

Plank, V. G., 1969: The size distribution of cumulus clouds in representative Florida populations. *J. Appl. Meteorol.*, **8**, 46–67, doi:10.1175/1520-0450(1969)008<0046:TSDOCC>2.0.CO;2.

Plant, R. S. and G. C. Craig, 2008: A stochastic parameterization for deep convection based on equilibrium statistics. *J. Atmos. Sci.*, **65**, 87–105, doi:10.1175/2007JAS2263.1.

Raasch, S. and T. Franke, 2011: Structure and formation of dust devil–like vortices in the atmospheric boundary layer: A high–resolution numerical study. *J. Geophys. Res.*, **116**, D16 120, doi:10.1029/2011JD016010.

Rauber, R. M., et al., 2007: Rain in shallow cumulus over the ocean - the RICO campaign. *Bull. Amer. Meteor. Soc.*, **88**, 12–18, doi:http://dx.doi.org/10.1175/BAMS-88-12-Rauber.

Richardson, H., S. Basu, and A. A. M. Holtslag, 2013: Improving stable boundary-layer height estimation using a stability-dependent critical bulk richardson number. *Boundary-Layer Meteorol.*, **148**, 93–109, doi:10.1007/s10546-013-9812-3.

Rodts, S. M. A., P. G. Duynkerke, and H. J. J. Jonker, 2003: Size distributions and dynamical properties of shallow cumulus clouds from aircraft observations and satellite data. *J. Atmos. Sci.*, **60**, 1895–1912, doi:10.1175/1520-0469(2003)060<1895:SDADPO>2.0.CO;2.

Romps, D. M. and A. B. Charn, 2015: Sticky thermals: Evidence for a dominant balance between buoyancy and drag in cloud updrafts. *J. Atmos. Sci.*, **72**, 2890–2901, doi:10.1175/JAS-D-15-0042.1.

Romps, D. M. and Z. Kuang, 2010: Nature versus nurture in shallow convection. *J. Atmos. Sci.*, **67**, 1655–1666, doi:http://dx.doi.org/10.1175/2009JAS3307.1.

Sagaut, P., 2006: *Large Eddy Simulation for Incompressible Flows - An Introduction*. 3d ed., Springer.

Saiki, E. M., C.-H. Moeng, and P. P. Sullivan, 2000: Large-eddy simulation of the stably stratified planetary boundary layer. *Boundary-Layer Meteorol.*, **95**, 1–30, doi:10.1023/A:1002428223156.

Sakradzija, M., A. Seifert, and A. Dipankar, 2016: A stochastic scale-aware parameteri-

zation of shallow cumulus convection across the convective gray zone. *J. Adv. Model. Earth Syst.*, **8**, 786–812, doi:10.1002/2016MS000634.

Sakradzija, M., A. Seifert, and T. Heus, 2015: Fluctuations in a quasi-stationary shallow cumulus cloud ensemble. *Nonlin. Processes Geophys.*, **22**, 65–85, doi:10.5194/npg-22-65-2015.

Schalkwijk, J., H. J. J. Jonker, A. P. Siebesma, and F. C. Bosveld, 2015: A year-long large-eddy simulation of the weather over cabauw: An overview. *Mon. Wea. Rev.*, **143**, 828–844, doi:10.1175/MWR-D-14-00293.1.

Schween, J. H., A. Hirsikko, U. Löhnert, and S. Crewell, 2014: Mixing-layer height retrieval with ceilometer and doppler lidar: from case studies to long-term assessment. *Atmos. Meas. Tech.*, **7**, 3685–3704, doi:10.5194/amt-7-3685-2014.

Seifert, A. and K. D. Beheng, 2001: A double-moment parameterization for simulating autoconversion, accretion and selfcollection. *Atmos. Res.*, **59(2)**, 265–281, doi:10.1016/S0169-8095(01)00126-0.

Shaw, R. H. and U. Schumann, 1992: Large-eddy simulation of turbulent flow above and within a forest. *Boundary-Layer Meteorol.*, **61**, 47–64, doi:10.1007/BF02033994.

Shen, S. and M. Y. Leclerc, 1995: How large must surface inhomogeneities be before they influence the convective boundary layer structure? a case study. *Q. J. R. Meteorol. Soc.*, **121**, 1209–1228, doi:10.1002/qj.49712152603.

Shutts, G. J. and T. N. Palmer, 2007: Convective forcing fluctuations in a Cloud-Resolving Model: Relevance to the stochastic parameterization problem. *J. Climate*, **20**, 187–202, doi:10.1175/JCLI3954.1.

Siebesma, A. P. and J. W. M. Cuijpers, 1995: Evaluation of parametric assumptions for shallow cumulus convection. *J. Atmos. Sci.*, **52**, 650–666, doi:http://dx.doi.org/10.1175/1520-0469(1995)052<0650:EOPAFS>2.0.CO;2.

Siebesma, A. P., P. M. M. Soares, and J. Teixeira, 2007: A combined eddy-diffusivity mass-flux approach for the convective boundary layer. *J. Atmos. Sci.*, **64**, 1230–1248, doi:http://dx.doi.org/10.1175/JAS3888.1.

Siebesma, A. P., et al., 2003: A large eddy simulation intercomparison study of shallow cumulus convection. *J. Atmos. Sci.*, **60**, 1201–1219.

Simpson, J. and V. Wiggert, 1969: Models of precipitating cumulus towers. *Mon. Wea. Rev.*, **97**, 471–489, doi:http://dx.doi.org/10.1175/1520-0493(1969)097<0471:MOPCT>2.3.CO;2.

Soares, P. M. M., P. M. A. Miranda, A. P. Siebesma, and J. Teixeira, 2004: An eddy-

diffusivity / mass-flux parametrization for dry and shallow cumulus convection. *Q. J. R. Meteorol. Soc.*, **130**, 3365–3383, doi:10.1256/qj.03.223.

Sommeria, G. and J. W. Deardorff, 1977: Subgrid-scale condensation in models of nonprecipitating clouds. *J. Atmos. Sci.*, **34**, 344–355, doi:http://dx.doi.org/10.1175/1520-0469(1977)034<0344:SSCIMO>2.0.CO;2.

Squires, P., 1958: The spatial variation of liquid water and droplet concentration in cumuli. *Tellus*, **10**, 372–380, doi:10.1111/j.2153-3490.1958.tb02024.x.

Stevens, B., C.-H. Moeng, and P. P. Sullivan, 1999: Large-eddy simulations of radiatively driven convection: Sensitivities to the representation of small scales. *J. Atmos. Sci.*, **56**, 3963–3984, doi:10.1175/1520-0469(1999)056<3963:LESORD>2.0.CO;2.

Stevens, B. and A. Seifert, 2008: Understanding macrophysical outcomes of microphysical choices in simulations of shallow cumulus convection. *J. Meteor. Soc. Japan*, **86A**, 143–162, doi:10.2151/jmsj.86A.143.

Stevens, B., et al., 2001: Simulations of trade wind cumuli under a strong inversion. *J. Atmos. Sci.*, **58**, 1870–1891, doi:10.1175/1520-0469(2001)058%3C1870:SOTWCU%3E2.0.CO;2.

Stevens, B., et al., 2005: Evaluation of large-eddy simulations via observations of nocturnal marine stratocumulus. *Mon. Wea. Rev.*, **133**, 1443–1462, doi:http://dx.doi.org/10.1175/MWR2930.1.

Stommel, H., 1947: Entrainment of air into a cumulus cloud. *J. Meteor.*, **4**, 91–94, doi:10.1175/1520-0469(1947)004<0091:EOAIAC>2.0.CO;2.

Stull, R. B., 2000: *Meteorology for Scientists and Engineers*. 2d ed., Brooks Cole.

Stull, R. B., 2009: *An Introduction to Boundary Layer Meteorology*. Springer.

Sušelj, K., J. Teixeira, and D. Chung, 2013: A unified model for moist convective boundary layers based on a stochastic eddy-diffusivity/mass-flux parameterization. *J. Atmos. Sci.*, **70**, 1929–1953, doi:10.1175/JAS-D-12-0106.1.

Sušelj, K., J. Teixeira, and G. Matheou, 2012: Eddy diffusivity/mass flux and shallow cumulus boundary layer: An updraft PDF multiple mass flux scheme. *J. Atmos. Sci.*, **69**, 1513–1533, doi:10.1175/JAS-D-11-090.1.

Teixeira, J., et al., 2008: Parameterization of the atmospheric boundary layer - a view from just above the inversion. *Bull. Amer. Meteor. Soc.*, **89**, 453–458, doi:10.1175/BAMS-89-4-453.

Tian, Y. and Z. Kuang, 2016: Dependence of entrainment in shallow cumulus convection

on vertical velocity and distance to cloud edge. *Geophys. Res. Lett.*, **43**, 4056–4065, doi:10.1002/2016GL069005.

Tiedtke, M., 1989: A comprehensive mass flux scheme for cumulus parameterization in large-scale models. *Mon. Wea. Rev.*, **117**, 1779–1800, doi:http://dx.doi.org/10.1175/1520-0493(1989)117<1779:ACMFSF>2.0.CO;2.

Tiedtke, M. A. H. and J. Slingo, 1988: Tropical forecasting at ECMWF: The influence of physical parametrization on the mean structure of forecasts and analyses. *Q. J. R. Meteorol. Soc.*, **114**, 639–664, doi:10.1002/qj.49711448106.

Troen, I. B. and L. Mahrt, 1986: A simple model of the atmospheric boundary layer; sensitivity to surface evaporation. *Boundary-Layer Meteorol.*, **37**, 129–148, doi:10.1007/BF00122760.

van der Dussen, J. J., S. R. de Roode, S. D. Gesso, and A. P. Siebesma, 2015: An LES model study of the influence of the free tropospheric thermodynamic conditions on the stratocumulus response to a climate perturbation. *J. Adv. Model. Earth Syst.*, **7**, 670–691, doi:10.1002/2014MS000380.

Van der Hoven, I., 1957: Power spectrum of horizontal wind speed in the frequency range from 0.0007 to 900 cycles per hour. *J. Meteor.*, **14**, 160–164, doi:10.1175/1520-0469(1957)014<0160:PSOHWS>2.0.CO;2.

vanZanten, M. C., et al., 2011: Controls on precipitation and cloudiness in simulations of trade-wind cumulus as observed during RICO. *J. Adv. Model. Earth Syst.*, **3**, 1–19, doi:10.1029/2011MS000056.

Vial, J., J.-L. Dufresne, and S. Bony, 2013: On the interpretation of inter-model spread in CMIP5 climate sensitivity estimates. *Clim. Dyn.*, **41**, 3339–3362, doi:10.1007/s00382-013-1725-9.

Wagner, T. M. and H.-F. Graf, 2010: An ensemble cumulus convection parameterization with explicit cloud treatment. *J. Atmos. Sci.*, **67**, 3854–3869, doi:http://dx.doi.org/10.1175/2010JAS3485.1.

Wielicki, B. and R. Welch, 1986: Cumulus cloud properties derived using Landsat satellite data. *J. Climate Appl. Meteor.*, **25**, 261–276, doi:10.1175/1520-0450(1986)025<0261:CCPDUL>2.0.CO;2.

Wyngaard, J. C., 2004: Toward numerical modeling in the "terra incognita". *J. Atmos. Sci.*, **61**, 1816–1826, doi:http://dx.doi.org/10.1175/1520-0469(2004)061<1816:TNMITT>2.0.CO;2.

Yanai, M., S. Esbensen, and J.-H. Chu, 1973: Determination of bulk properties of tropical

cloud clusters from large-scale heat and moisture budgets. *J. Atmos. Sci.*, **30**, 611–627, doi:10.1175/1520-0469(1973)030<0611:DOBPOT>2.0.CO;2.

Zhang, Y. and S. A. Klein, 2013: Factors controlling the vertical extent of fair-weather shallow cumulus clouds over land: Investigation of diurnal-cycle observations collected at the ARM Southern Great Plains site. *J. Atmos. Sci.*, **70**, 1297–1315, doi:10.1175/JAS-D-12-0131.1.

Acknowledgments

I would like to thank Roel for giving me the opportunity to work on this fascinating topic and for the enthusiastic discussions and support. I would also like to thank Vera for the help in supervising and the good company in the office, and Susanne for the supervision from an observational point of view. For proofreading of this thesis I thank Vera. I thank Christopher Moseley for his generous help with setting up the forcing of LES with COSMO. I would also like to thank Karin Boessenkool and the GSGS for the structure given to my PhD and the financial help in traveling to the AGU and the fellowship allowing me the time to finish this thesis; and to HPSCTerrSys for the financial support to conduct most of this research. Finally, thanks goes to the Inscapers, Infernos and the institute for creating a good working atmosphere and for always being willing to help.

Erklärung

Ich versichere, dass ich die von mir vorgelegte Dissertation selbständig angefertigt, die benutzten Quellen und Hilfsmittel vollständig angegeben und die Stellen der Arbeit - einschließlich Tabellen, Karten und Abbildungen -, die anderen Werken im Wortlaut oder dem Sinn nach entnommen sind, in jedem Einzelfall als Entlehnung kenntlich gemacht habe; dass diese Dissertation noch keiner anderen Fakultät oder Universität zur Prüfung vorgelegen hat; dass sie - abgesehen von unten angegebenen Teilpublikationen - noch nicht veröffentlicht worden ist, sowie, dass ich eine solche Veröffentlichung vor Abschluss des Promotionsverfahrens nicht vornehmen werde. Die Bestimmungen der Promotionsordnung sind mir bekannt. Die von mir vorgelegte Dissertation ist von Prof. Dr. Roel Neggers betreut worden.

Teilpublikation:

Brast, M., R. A. J. Neggers and T. Heus (2016), What determines the fate of rising parcels in a heterogeneous environment?, J. Adv. Model. Earth Syst., 8, 1674 - 1690, doi:10.1002/2016MS000750